

STUDY OF METALLIC NANO-OPTIC STRUCTURES

by

Zhijun Sun

B.S. in Physics, Lanzhou University, China, 1997

M.S. in Electronics Engineering, Lanzhou University, China, 2000

Submitted to the Graduate Faculty of
the School of Engineering in partial fulfillment of
the requirements for the degree of
Doctor of Philosophy

University of Pittsburgh

2005

UNIVERSITY OF PITTSBURGH

SCHOOL OF ENGINEERING

This dissertation was presented

by

Zhijun Sun

It was defended on

February 15, 2005

and approved by

Hong Koo Kim, Professor, Department of Electrical and Computer Engineering

Mahmoud El-Nokali, Associate Professor, Department of Electrical and Computer Engineering

Joel Falk, Professor, Department of Electrical and Computer Engineering

Dietrich W. Langer, Professor, Department of Electrical and Computer Engineering

Rob Coalson, Professor, Department of Chemistry

Hrvoje Petek, Professor, Department of Physics and Astronomy

Dissertation Director: Hong Koo Kim, Professor, Department of Electrical and Computer
Engineering

ABSTRACT

STUDY OF METALLIC NANO-OPTIC STRUCTURES

Zhijun Sun, PhD

University of Pittsburgh, 2005

Physical phenomena (optical, electronic and optoelectronic) occurring in metallic nanostructures offer an interesting potential in that they may allow us to overcome the limits of diffractive optics and to develop new functional devices complementing the dielectric-based conventional optics. Optical waves incident to a metallic structure, for example, can excite a collective oscillation of electrons, so-called surface plasmons (SPs). The spatial extension of SP fields is governed by the size of the nanostructure and can be made much smaller than the wavelength of light. These features are potentially useful in developing ultracompact photonic chips, i.e., miniaturizing the optics into subwavelength dimensions.

In this thesis, we have investigated the plasmonic phenomena occurring in metallic nanoaperture array structures. A novel fabrication process has been developed to form highly ordered nanoaperture (both slits and holes) arrays on metallic layers. Optical characterization of the fabricated nanostructures revealed many interesting properties (in transmission, reflection, filtering, confinement, etc.) involving plasmonic interactions. The plasmonic phenomena in nanoaperture arrays have been analyzed theoretically: analytical solutions of plasmonic waveguiding inside nanoslits were formulated; funneling of light into nanoslit was simulated; the

in-plane surface plasmon band structures at the metal/dielectric interfaces were modeled; the dynamic evolution of polarization in metal islands was analyzed. The finite-difference time-domain (FDTD) analysis of optical field distribution and propagation has been performed, and the simulation results were compared with the analytic results and experimental data. Detailed mechanisms of the plasmonic interactions in nanoaperture arrays have been developed and proposed based on this experimental and theoretical study.

We further studied optical transmission properties of bi-layer metallic nanoslit arrays. The structure is found to reveal Fabry-Perot-resonator-like characteristics and the transmittance, passband, and beam polarization properties are determined by structure, dimension, and configuration. Near-field interaction and coupling in the bi-layer slit array structures were also analyzed with FDTD simulation. We also studied surface plasmon effects in reflective metallic grating structures, which show strong reflection quenching under cross-metal SP coupling conditions. We have designed and analyzed metallic nano-optic lenses based on nanoslit array structures. The phase of optical radiation emanating from each aperture is controlled by the metal thickness and aperture size. FDTD simulation of the nano-optic lenses demonstrates refractive transmission of light and beam shaping (focusing and collimation). This study opens up the possibility of developing a new class of optics that can complement the conventional dielectric-based refractive/diffractive optics.

TABLE OF CONTENTS

ABSTRACT.....	iii
TABLE OF CONTENTS.....	v
LIST OF FIGURES.....	viii
ACKNOWLEDGEMENT.....	xii
1.0 INTRODUCTION	1
1.1 Overview.....	1
1.2 Optical Properties of Metallic Materials.....	4
1.3 Surface Plasmons at Metal Surfaces.....	11
1.4 Scattering and Absorption in Interaction of Light with Metallic Nanostructures....	19
1.5 FDTD Numerical Simulation Method.....	21
1.5.1 Discretization.....	23
1.5.2 Stability.....	24
1.5.3 Absorbing Boundary Conditions (ABC).....	25
1.5.4 Metal Surface Boundary Conditions.....	27
1.6 Summary.....	30
2.0 TRANSMISSION OF LIGHT THROUGH NARROW SLITS IN THICK METALLIC GRATINGS.....	31
2.1 Introduction.....	31
2.2 Fabrication of One-dimensional Thick Metallic Gratings with Narrow Slits.....	33
2.3 Characterization and Analysis of the Optical Transmission Spectrum.....	38

2.3.1	Characterization.....	38
2.3.2	Spectrum Analysis.....	39
2.4	Guiding of Light with Plasmon Mode through Nanometer-width Slit in Thick Metallic Slab.....	50
2.4.1	Field and Wave Solutions in the Slit.....	51
2.4.2	Propagation Constants and Effective Index.....	60
2.4.3	Dipole Modeling of Symmetric Plasmon Mode inside Slit.....	63
2.4.4	Funneling of Light into Metallic Narrow Slit.....	64
2.5	Modeling of Surface Plasmon Band Structures on Metallic Grating Surface.....	81
2.6	Dynamic Polarization of Infinite Metallic cylinders	91
2.6.1	Exact Solution for the Dynamical Polarization in a Metal Cylinder.....	91
2.6.2	Dipolar Plasmon Resonance inside a Metal Cylinder.....	98
2.6.3	Coupling of Plasmon Resonance Mode between Arrayed Metallic Cylinders.....	104
2.7	FDTD Simulation of Field and Charge Distributions.....	114
2.8	Summary.....	124
3.0	OPTICAL INTERACTION WITH PERIODIC METALLIC NANOSTRUCTURES.....	125
3.1	Band-pass Transmission of Light through 2D Metallic Nanopore Arrays.....	125
3.1.1	Fabrication.....	127
3.1.2	Characterization and Discussion.....	131
3.2	Optical Transmission through Bi-layer 1D Narrow Metallic Slit Arrays.....	138
3.2.1	Fabrication and Characterization.....	138
3.2.2	Results and Discussion.....	139
3.2.3	FDTD Simulation of Near-field Interaction Between Bi-layer Slit Arrays	146

3.3	Reflection Quenching of 1D Metallic Gratings.....	157
3.3.1	Fabrication and Characterization.....	157
3.3.2	Results and Discussion.....	157
3.4	Summary.....	171
4.0	REFRACTIVE TRANSMISSION OF LIGHT AND BEAM SHAPING WITH METALLIC NANO-OPTIC LENSES.....	172
5.0	CONCLUSIONS	188
	BIBLIOGRAPHY.....	192

LIST OF FIGURES

Figure 1.1	Dielectric constant of silver in the optical range.....	10
Figure 1.2	Surface plasmon waves on metal surface and the dispersion relation.	17
Figure 1.3	Grating coupling between light and SPs.....	18
Figure 1.4	Two-dimensional discretization of TM-polarized light incidence on metallic slab with narrow slits using Yee's algorithm.....	28
Figure 1.5	Minimization of load on absorbing boundary conditions (ABCs).....	29
Figure 2.1	SEM micrographs of a silver 1D grating structure with subwavelength slits formed on a quartz substrate using holographic lithography and angled deposition.....	35
Figure 2.2	Schematic process flow forming 1D thick metallic gratings with narrow slits....	36
Figure 2.3	Angled-deposition of Ag onto quartz substrate with mesa using thermal evaporation.....	37
Figure 2.4	Set-up for optical characterization of Ag subwavelength gratings with narrow slits.....	46
Figure 2.5	Transmission spectra of 1D slit array samples with grating period of 370 nm and with 120- or 200-nm-thick Ag.....	47
Figure 2.6	Transmission spectra of 1D slit array samples with grating period of 780 nm and Ag of different thickness.....	48
Figure 2.7	Transmission and reflection measured as a function of incidence angle at the wavelength of 633 nm (TM polarized).....	49
Figure 2.8	Illustration of TM-polarized light normal incidence on a broad thick metal slab with a narrow slit.....	70
Figure 2.9	Dependence of real and imaginary part of the propagation constant β on wavelength with slit width as parameters.....	71

Figure 2.10	Dependence of real and imaginary part of the propagation constant β on slit width with wavelength as parameters.....	72
Figure 2.11	Parametric plot of the propagation constant β with wavelength as parameter at a fixed slit width of 50 nm.....	73
Figure 2.12	Parametric plots of transverse wave vectors inside slit (γ_1) and silver skin depth (γ_2) with slit width as parameter for fixed wavelength.....	74
Figure 2.13	Intensity distribution along the transverse direction of the plasmon mode inside the narrow slit.....	75
Figure 2.14	A dipole wave model of the symmetry plasmon mode inside the narrow metallic slit	76
Figure 2.15	Funneling of optical energy into plasmon wave mode by slit entrance	77
Figure 2.16	Time-averaged intensity distribution in funneling of light into a single slit.....	78
Figure 2.17	Dependence of funneling on slit width and incidence beam wavelength	79
Figure 2.18	Time-averaged intensity distribution in light transmission through single slit in a metal layer of different thickness	80
Figure 2.19	Schematic illustration of the model for band structures of SP waves at the top and bottom dielectric/metal interface.....	87
Figure 2.20	Photonic band structures of surface plasmons at the top and bottom dielectric/Ag interfaces of a thick Ag slab with narrow slit arrays (the period of slit arrays is 370 nm).....	88
Figure 2.21	Photonic band structures of surface plasmons at the top and bottom dielectric/Ag interfaces of a thick Ag slab with narrow slit arrays (the period of slit arrays is 780 nm).....	90
Figure 2.22	Schematic illustration of the charge and electric field distribution of the resonance SP wave modes at B. Z. center.....	90
Figure 2.23	Illustration of a plane wave incident on an infinite length metal cylinder with TM-polarization.....	106
Figure 2.24	Dependence of A_n/B_n on ω for $n = 1 - 6$	107
Figure 2.25	Symmetry of irreducible representations of the C_{2v} point group for a metallic cylinder array.....	108

Figure 2.26	The angular variation of the magnetic field and the symmetry assignment of the resonant states according to the irreducible representations of the C_{2v} point group.....	109
Figure 2.27	Dipolar plasmon resonance position dependence on size of a silver cylinder in air background.....	110
Figure 2.28	Polar distribution of the Hz-field scattered by a metallic cylinder at near and far fields	111
Figure 2.29	Coupling of dipolar plasmon modes between 1D-arrayed metallic cylinders ...	112
Figure 2.30	Coupling of dipolar plasmon modes between 1D-arrayed metallic rectangular pillars	113
Figure 2.31	FDTD simulated transmission spectra of light through 1D narrow slits in thick silver slab.....	120
Figure 2.32	FDTD simulated Hz-field distribution at particular wavelengths.....	121
Figure 2.33	FDTD simulated charge distribution at particular wavelengths.....	122
Figure 2.34	FDTD simulated instant power flow at particular wavelengths	123
Figure 3.1	Schematic illustrations of procedures transferring holographic photoresist grating patterns onto substrate	133
Figure 3.2	SEM micrographs of Cr mesh patterns on silica substrate obtained with the two-step 1D grating fabrication process	134
Figure 3.3	SEM micrographs of anodic alumina pore arrays on silica substrates.....	135
Figure 3.4	SEM micrographs of silver pore arrays formed on porous anodic alumina template	136
Figure 3.5	Transmission spectrum of 2D square lattice silver nanopore arrays formed on porous anodic alumina template	137
Figure 3.6	Schematic diagram of the configuration of the bi-layer 1D narrow metallic grating slits.....	143
Figure 3.7	Comparison of transmission spectra of a bi-layer metallic grating slit array and a single-layer one.....	144
Figure 3.8	Transmission modulation by varying the cross angle of the gratings on a bi-layer metallic narrow slit arrays.....	145

Figure 3.9	DTD simulated transmission of light through single layer of silver films with narrow slit arrays of different periods.....	151
Figure 3.10	FDTD simulated transmission of light through bi-layer of silver films with narrow slit arrays of different periods	152
Figure 3.11	FDTD simulated transmission of light through bi-layer of silver films with narrow slit arrays at different layer separations	153
Figure 3.12	Transmission of bi-layer metallic narrow slit arrays modeled with Fabry-Perot cavity modes	154
Figure 3.13	Effects of lateral shifts on transmission of bi-layer silver narrow slit arrays simulated with FDTD method	155
Figure 3.14	Hz-field distribution in transmission of light through bi-layer of silver narrow slit arrays under different alignment simulated with FDTD method	156
Figure 3.15	Schematic drawing of the 1D metallic reflective gratings.....	165
Figure 3.16	Angular dependence of TM-polarized Zero-order reflection and transmission of thin metallic reflective gratings with different depth thickness.....	166
Figure 3.17	Schematic phase matching diagram of backward light-SP coupling and SP-light decoupling with subwavelength metallic gratings.....	167
Figure 3.18	Coupling of light into surface plasmon waves with shallow silver gratings.....	168
Figure 3.19	Coupling of light into surface plasmon waves with deep reflective gratings and thick transmissive gratings.....	169
Figure 3.20	Forward coupling of light into surface plasmons with metallic gratings.....	170
Figure 4.1	FDTD simulated optical transmission through a single nanoaperture formed on a metal layer.....	181
Figure 4.2	Characteristics of a surface plasmon wave through a nanoslit structure formed in metal	182
Figure 4.3	Refraction of light at a nano-apertured metal surface.....	183
Figure 4.4	FDTD simulated beam shaping with metallic nano-optic lenses	184
Figure 4.5	FDTD simulated beam steering and focusing with planar metallic nanoslit lenses	186
Figure 4.6	Effects of element source intensity on beam steering in near field with metallic slit arrays	187

ACKNOWLEDGEMENT

I would like to thank my supervisor, Prof. Hong Koo Kim, for his guidance, support, encouragement and confidence in me throughout this work. For more than four years, we have shared the joy and challenges awarded in this adventure. It is surely an unforgettable experience. Additionally, I would like to thank my colleagues, primarily Yun-Suk Jung for his experimental support in this work and also Dr. Mingjiao Liu for his past help. I gratefully acknowledge the support from the Office of Naval Research and the National Science Foundation during this project. And I express my thanks to Professors, Mahmoud El-Nokali, Joel Falk, Dietrich W. Langer, Rob Coalson and Hrvoje Petek, who have been serving in the PhD committee.

This work and thesis are dedicated to my parents. I am full of gratitude for their continuous support, love and encouragement in all these years.

1.0 INTRODUCTION

1.1 OVERVIEW

Recent advances in electro-optical systems demand drastic increases in the degree of integration of photonic and electronic devices for large-capacity and ultrahigh-speed signal transmission and information processing [1]. Device size has to be scaled down to nanometric dimensions to meet this requirement, which will become even more strict in the future. In the case of photonic devices, this requirement cannot be met only by decreasing the sizes of materials. It is indispensable to decrease the size of the electromagnetic field used as a carrier for signal transmission. Such a reduction in the size of the electromagnetic field beyond the diffraction limit of the propagating field is expected to be possible when we utilize the optical near field phenomena occurring in metallic material systems.

The basic optical near field properties are related to evanescent waves that arise at illuminated material boundaries and decay exponentially in the direction perpendicular to the boundary surface. The evanescent waves mediate optical interactions only in a short range in the direction normal to the surface and have a wave vector along the surface with magnitudes larger than those of optical waves in free space [2]. This makes it possible to drive an optical interaction localized in a spatial extent narrower than the optical wavelength in vacuum which

corresponds to the origin of ultrahigh spatial resolution realized in optical near-field techniques. Optical fields exhibit such localized behavior only as a result of interactions with matter, so that optical near-fields can be considered modes of optical fields coupled with matter [3]. Such evanescent modes are especially prominent at metallic material surfaces because of their strong attenuation of propagating mode inside. Great enhancement of field at metal surface intensifies the light localization.

Near-field optics has progressed rapidly in elucidating the science and technology of such fields. Exploiting an essential feature of optical near fields, i.e. the resonant interaction between electromagnetic fields and matter in nanometric regions, important applications and new directions such as studies in near-field imaging, spatially resolved spectroscopy, nano-fabrication, nano-photonic devices, ultrahigh-density optical memory, and atom/particle manipulation have been realized and significant progress has been reported [3]. As the fabrication of nanometric materials are progressed simultaneously, a new field can be open in future technologies for wide applications.

Functioning of localized light in near field involves strong coupling with other objects. Such coupling is dependent on related materials, object size and shape. In another regime, by carefully constructing nano-structured material systems to satisfy certain resonant conditions, the neighboring local field can also be coupled with each other so as to manipulate both spatial and frequency distribution of light in far field. Underlying technology implies advantages of compactness and tunability for integration compared to conventional peers. In this work, new technologies were developed to fabricate such nano-structures of metallic materials (especially

with Ag). We have, experimentally and theoretically, studied their optical properties both in near and far fields. Finite-difference time-domain (FDTD) simulations were also performed for numerical analysis of electromagnetic (EM) field distribution with Maxwell's equations. Various applications demonstrated / to be proposed suggest that worthy investigations are deserved to deepen and broaden this topic.

In this thesis, the topic will be introduced step-by-step, piece-by-piece with five chapters and their sections. Specifically, in the following sections of the Chapter 1, some fundamentals on light interaction with bulk metallic materials are briefly reviewed, which will be shown in later chapters linked to the optical properties of small metallic structures in certain relations. The basic FDTD simulation method will also be introduced in the first chapter to allow later chapters to more focus on results. In Chapter 2, giant optical transmission through extremely narrow slit arrays is studied extensively. Analytical models are established to elucidate the different physical effects involved in this complex system with "simple" structures. The numerical simulation will further illuminate the understandings. In Chapter 3, various metallic nano-structures are introduced and their optical properties are studied; their characteristics are shown closely related to the interaction of photons and surface plasmons (SP). In Chapter 4, a concept of utilizing metallic nano-optics lenses for beam shaping is proposed and studied, which offers unique capability in shaping and processing optical beams that cannot be obtained in conventional dielectric-based refractive and diffractive optical lenses. Finally, in Chapter 5, we summarize the former chapters and conclude.

1.2 OPTICAL PROPERTIES OF METALLIC MATERIALS

Basically, the optical response of matter is determined by internal electronic processes that involve an interaction with optical fields consistent with both electronic and electromagnetic boundary conditions [3]. The resulting scattered fields reflect the properties of these internal processes in the illuminated objects, especially when they are observed in an optical near field. The scattered fields exhibit an asymptotic behavior in the far-field limit since propagating optical waves carry electromagnetic energy out of the object with a retarded nature. In this case, the optical response of matter can be represented in macroscopic quantities, such as dielectric functions, which enable us to reproduce the macroscopic electromagnetic boundary conditions correctly.

The internal electronic states of matters are characterized by its crystal energy band structure, a consequence of the periodicity of the crystal lattice. Depending on the electron distribution in energy bands and band gaps as formed, marked difference of optical properties are exhibited in conductors, semiconductors and insulators. Inside of a metal (typical conductor), a band of electron states is incompletely filled, or filled band overlaps in energy with an empty band (called “semi-metals”) [4]. Usually in metals, under an applied optical electric field, electrons at the top of the energy distribution are excited into adjacent unoccupied states in the same energy band and electric current is formed, which is so-called intraband absorption. This mechanism can be applied to all low-energy photons. While in nonconductors (semiconductors

and insulators), absorption is only possible for photon energies greater than the band gap, which mechanism is called interband absorption.

Optical properties of free-electron metals are best modeled by Drude theory [4]. In this model, a free electron is considered as an oscillator, with mass m and charge e , driven by optical electric field (assume the matter is non-magnetic). The equation of motion can be described with

$$m\ddot{\bar{x}} + b\dot{\bar{x}} = e\bar{E} \quad (1.1)$$

where \bar{E} is the applied optical electric field; \bar{x} is the displacement from equilibrium; b is the damping constant. For free-electron metals, the atomic Coulomb force is neglected. A restoring force $K\bar{x}$ is included on the left hand side of Equation (1.1) in a more general Lorentz model.

Taking the electric field to be time harmonic with frequency ω and neglecting the transient response of electrons to the field, Equation (1.1) results in a polarization (dipole moment per unit volume)

$$\bar{P} = -\frac{\omega_p^2}{\omega^2 + i\gamma\omega} \epsilon_0 \bar{E} \quad (1.2)$$

where $\gamma = b/m$, $\omega_p^2 = Ne^2/m\epsilon_0$ defined as plasma frequency, N is the number of oscillators per unit volume, and ϵ_0 is the dielectric constant in vacuum. Considering the polarization and applied field for $\vec{D} = \epsilon\epsilon_0\vec{E}$ in Maxwell's equations, we have

$$\epsilon = 1 + \chi = 1 - \frac{\omega_p^2}{\omega^2 + i\gamma\omega}, \quad (1.3)$$

where χ is called susceptibility, with real and imaginary parts

$$\epsilon' = 1 - \frac{\omega_p^2}{\omega^2 + \gamma^2}, \quad (1.4a)$$

$$\epsilon'' = \frac{\omega_p^2\gamma}{\omega(\omega^2 + \gamma^2)}, \quad (1.4b)$$

Physically, dynamic polarization of the metal is the collective oscillation of electrons inside a positive ionic atomic lattice. The whole entity keeps neutral, so it is called plasma oscillation and its quantum-mechanical exciton is called plasmon with energy $\hbar\omega_p$. Individual electron's behavior is exhibited in the motion of a collection of electrons. The damping constant is related to the average time τ between collisions by $\gamma = 1/\tau$. Collision times are usually dominated by interaction of the electrons with lattice vibrations: electron-phonon scattering [5]. For most metals at room temperature γ is much less than ω_p . Plasma frequencies of metals are in the visible and ultraviolet (UV), $\hbar\omega_p$ ranges from 3 to 20 eV. Therefore, a good approximation to the Drude dielectric functions at visible and UV frequencies is

$$\varepsilon' \approx 1 - \frac{\omega_p^2}{\omega^2}, \quad (1.5a)$$

$$\varepsilon'' \approx \frac{\omega_p^2 \gamma}{\omega^3}. \quad (1.5b)$$

Dude theory has its good applicability to metals such as aluminum, but for many other metals, including silver (Ag), bound-electrons appreciably alters the free-electron optical properties due to excitation of the weakly bounded inner shell electrons. Thus the dielectric function is modified as $\varepsilon = \varepsilon_f + \delta\varepsilon_b$ to include a contribution $\delta\varepsilon_b$ of bound-electrons, which part should be modeled by Lorentz's with $K \neq 0$.

Intrinsically, the real and imaginary parts of the dielectric function are not independent. They are linked by the Kramers-Kronig relation [5]

$$\varepsilon'(\omega) = 1 + \frac{2}{\pi} P \int_0^{\infty} \frac{\Omega \varepsilon''(\Omega)}{\Omega^2 - \omega^2} d\Omega. \quad (1.6)$$

where P denotes the Cauchy principal value of the integral, defined in Reference [5, p21]. The Kramers-Kronig relation tells that frequency dependence of real and imaginary parts of the dielectric function implies each other. Its physical contents are the assumption of linearity and causality in its derivation: (1) $\bar{P}(t)$ is linearly dependent on $\bar{E}(t)$; (2) the system has no response to the field before it is applied.

The complex refractive index, $\tilde{N} = n + ik$, are also frequently used to describe the optical properties of absorbing media [6]. Here, n is the refractive index usually used for transparent media ($k = 0$). Since $\varepsilon = \varepsilon' + i\varepsilon'' = \tilde{N}^2$, we have

$$\varepsilon' = n^2 - k^2, \quad \varepsilon'' = 2nk, \quad (1.7)$$

or

$$n = \left[\varepsilon' + \sqrt{\varepsilon'^2 + \varepsilon''^2} \right]^{1/2} / \sqrt{2}, \quad k = \left[-\varepsilon' + \sqrt{\varepsilon'^2 + \varepsilon''^2} \right]^{1/2} / \sqrt{2} \quad (1.8)$$

A time-harmonic plane wave in such a media can be expressed as [2]

$$\vec{E} = \vec{E}_0 e^{i[\hat{k}\vec{r}\cdot\vec{s} - \omega t]} = \vec{E}_0 e^{-\frac{\omega}{c}k\vec{r}\cdot\vec{s}} e^{i\omega\left[\frac{n}{c}\vec{r}\cdot\vec{s} - t\right]} \quad (1.9)$$

where wave vector in the media is $\hat{k} = \omega\tilde{N}/c = \omega(n + ik)/c$, and \vec{s} is its unit vector. The absorption coefficient is

$$\alpha = \frac{2\omega k}{c} = \frac{4\pi k}{\lambda_0}. \quad (1.10)$$

And $d = \frac{1}{\alpha}$ is the propagation length that the energy density falls to $1/e$ of its original value,

which is also defined as skin depth for normal incident light. It should be noted that the foregoing expressions are valid for cubic crystals or randomly oriented polycrystalline media.

For noncubic crystals, ε become tensors and \tilde{N} and α become anisotropic as well.

It should also be noted that, in many cases, we deal with non-crystal/poly-crystal matters, whose optical properties are results of collective behavior of multiple scattering and absorption of light by short-range crystals inside of them. Macroscopically, we take the effective value of dielectric constant. In case that the short-range crystal size is less than the electronic mean free path limit, the optical properties will be strongly affected by electronic boundary conditions, which will be mentioned in Section 1.4 with the similar case for applicability of bulk dielectric constant to small particles.

Silver is a favored material for this study because of its high conductivity, relatively small imaginary part dielectric constant ϵ'' for lower attenuation and the deep UV bulk plasma frequency ($\lambda_p \approx 360nm$) away from visible range. In this work, experimentally obtained optical constants [6] of silver are used both in analytical calculations and numerical simulations. Intermediate values between experimental data points are obtained from fitted 6th-order polynomial function in a range of 350~1800 nm wavelength, which is shown in Figure 1.1. Under the tolerance of experimental accuracy, these data have included whatever optical mechanism involved.

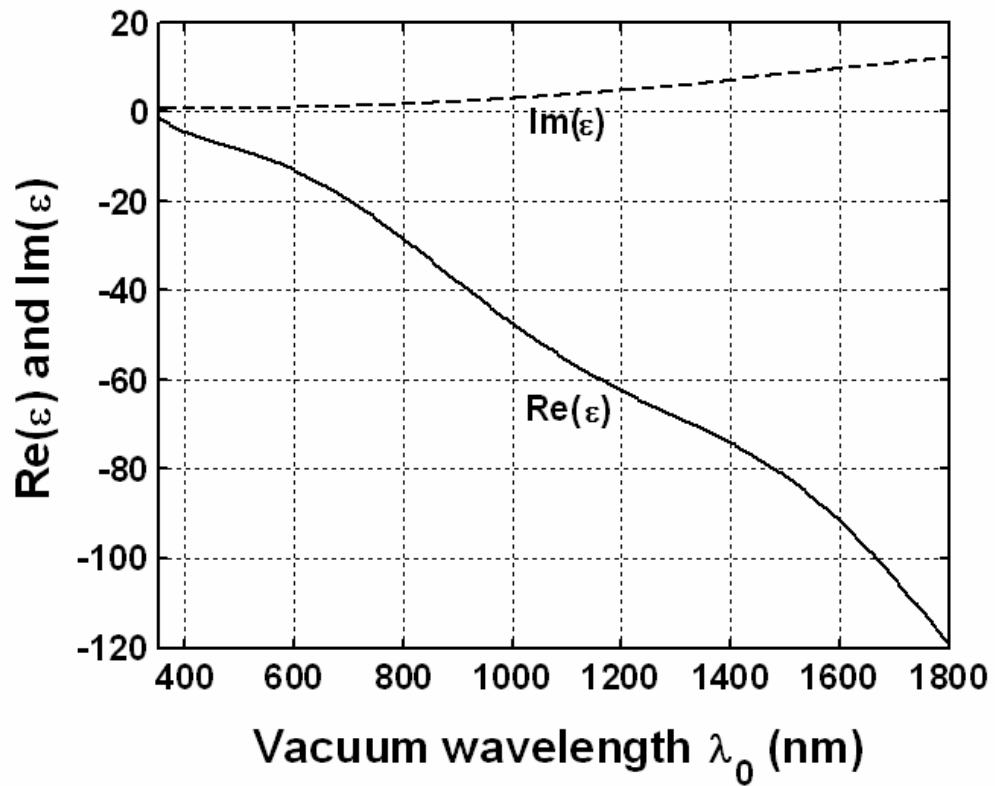


Figure 1.1. Dielectric constant of silver in the optical range. The curves for real and imaginary parts of the dielectric constant are fitted on the experimental data from Reference [6].

1.3 SURFACE PLASMONS AT METAL SURFACES

From Equation (1.9), it's obvious that propagating wave cannot exist in a metal media with size much larger than the attenuation length ($1/\alpha$) due to large absorption of metal. As a light beam is incident upon a metal surface from a dielectric surrounding media, only surface waves could possibly exist as satisfying the EM wave boundary conditions, or specified as phase matching, equal wave vector in both media along the interface or called momentum conservation along the interface. Physically, we know from the previous section that optical properties of metals are basically effects of collective behavior of electrons, oscillation under applied optical field. The surface plasma oscillation is the coherent fluctuations of electron charges on a metal boundary, which can be characterized as fluctuation of electron charge density. Such an electron density wave is accompanied by an electromagnetic field, which transversally attenuates quickly in the depth direction, and longitudinally propagates along the metal surface. Thus, we can configure surface plasmon wave as

$$(\text{Surface plasmon}) = (\text{Electron oscillation}) + (\text{Electromagnetic wave})$$

On the one hand, the EM wave drives electron oscillation; on the other hand, electron oscillation affects field distribution. They are coupled with each other such that, by studying one, theoretically one can obtain all information of the other. Thus, traditionally, surface plasmons are studied in two approaches: on the electronic excitation base [8] and on the electromagnetic field and wave base [7]. The first approach turned out to be rather complicated for interpreting

macroscopic experimental results in a quantitative way. Thus, the EM approach is more preferred by physicists, especially those studying optical properties of surface plasmons. And mostly it seems to be effective and sufficient for both interpreting phenomena and performing experiment design. Here, we also study with an electromagnetic view.

Schematically, the charge density and EM field distribution at a metal/dielectric interface can be illustrated as shown in Figure 1.2(a). The field is strongly localized at the interface and its distribution can be described by [7]

$$E = E_0^\pm \exp[+i(k_x x \pm k_z z - \omega t)] \quad (1.11)$$

with + for $z \geq 0$, - for $z \leq 0$, and with imaginary k_z , which causes the exponential decay of the field E_z . The wave vector k_x lies parallel to the x direction; $k_x = 2\pi/\lambda_p$, where λ_p is the wavelength of the plasma oscillation. Maxwell's equations yield the retarded dispersion relation for the plane surface of a semi-infinite metal with the dielectric function ($\epsilon_1 = \epsilon_1' + i\epsilon_1''$), adjacent to a medium ϵ_2 as air, vacuum or other dielectric media:

$$D_0 = \frac{k_{z1}}{\epsilon_1} + \frac{k_{z2}}{\epsilon_2} = 0 \quad \text{together with} \quad (1.12)$$

$$\epsilon_i \left(\frac{\omega}{c} \right)^2 = k_x^2 + k_{zi}^2 \quad \text{or} \quad (1.13)$$

$$k_{zi} = \left[\varepsilon_i \left(\frac{\omega}{c} \right)^2 - k_x^2 \right]^{1/2}, \quad i = 1, 2.$$

The wave vector k_x is continuous through the interface. The dispersion relation, Equation (1.12) can be written as

$$k_x = \frac{\omega}{c} \left(\frac{\varepsilon_1 \varepsilon_2}{\varepsilon_1 + \varepsilon_2} \right)^{1/2}. \quad (1.14)$$

If we assume besides a real ω and ε_2 that $\varepsilon_1'' < |\varepsilon_1'|$, we obtain a complex $k_x = k_x' + ik_x''$ with

$$k_x' = \frac{\omega}{c} \left(\frac{\varepsilon_1' \varepsilon_2}{\varepsilon_1' + \varepsilon_2} \right)^{1/2} \quad (1.15)$$

$$k_x'' = \frac{\omega}{c} \left(\frac{\varepsilon_1' \varepsilon_2}{\varepsilon_1' + \varepsilon_2} \right)^{3/2} \frac{\varepsilon_1''}{2(\varepsilon_1')^2}. \quad (1.16)$$

For real k_x' , one needs $\varepsilon_1' < 0$ and $|\varepsilon_1'| > \varepsilon_2$, which can be fulfilled in a metal and also in a doped semiconductor near the eigen frequency; k_x'' determines the internal absorption. The dispersion relation, shown in Figure 1.2(b), approaches the light line $\sqrt{\varepsilon_2} \omega / c$ at small k_x , but remains larger than $\sqrt{\varepsilon_2} \omega / c$, so that the SPs cannot transform into light: it is a “ nonradiative ” SP. At large k_x or $\varepsilon_1' \rightarrow -\varepsilon_2$, the value of ω approaches

$$\omega_{sp} = \frac{\omega_p}{\sqrt{1 + \varepsilon_2}}. \quad (1.17)$$

For a free electron gas where ω_p is the plasma frequency $\sqrt{4\pi N e^2/m}$, with N the bulk electron density. With increasing ε_2 , the value of ω_{sp} is reduced. At large k_x the group velocity goes to zero as well as the phase velocity, so that the SP resembles a localized fluctuation of the electron plasma.

As the field amplitude of the SPs decreases exponentially normal to the surface, the value of the skin depth at which the field falls to $1/e$, becomes

$$\hat{z} = \frac{1}{|k_{zi}|} \quad \text{or} \quad (1.18)$$

in the medium with ε_2 :
$$\hat{z}_2 = \frac{\lambda_0}{2\pi} \left(\frac{\varepsilon_1' + \varepsilon_2}{\varepsilon_2^2} \right)^{1/2}$$

in the metal with ε_1 :
$$\hat{z}_1 = \frac{\lambda_0}{2\pi} \left(\frac{\varepsilon_1' + \varepsilon_2}{\varepsilon_1'^2} \right)^{1/2}. \quad (1.19)$$

Typically, for $\lambda_0 = 6000 \text{ \AA}$ one obtains for silver $\hat{z}_2 = 3900 \text{ \AA}$ and $\hat{z}_1 = 240 \text{ \AA}$ [7]. The intensity of SPs propagating along a smooth surface decreases as $e^{-2k_x''x}$. The length L_i after which the intensity decreases to $1/e$ is then given by

$$L_i = (2k_x'')^{-1}. \quad (1.20)$$

Typically, in the visible region, L_i reaches the value of $L_i = 22\mu m$ in silver at $\lambda_0 = 5145 \text{ \AA}$ and $L_i = 500\mu m$ at $\lambda_0 = 10600 \text{ \AA}$ [7].

From Figure 1.2(b), it's shown that the dispersion relation of SPs lies right from the light line ($k_x > \omega/c$). Thus, for optical excitation of SPs, the wave vector $\hbar\omega/c$ of a given photon energy $\hbar\omega$ has to be increased by a Δk_x value so as to “transform” the photons into SPs. Usually, there are two methods of using (1) grating coupler; and (2) attenuated total reflection (ATR) coupler [7]. Here, grating coupling of light into SPs is of our interest in science and technology point of view.

If light ($k = \omega/c$) hits a grating with a grating constant d_g , at an angle θ_0 its component in the surface can have wave vectors $(\omega/c)\sin\theta_0 \pm m \cdot k_g$ with m an integer and $k_g = 2\pi/d_g$. The dispersion relation, Equation (1.14), can then be fulfilled by the sum

$$k_x = \frac{\omega}{c} \sin\theta_0 \pm m \cdot k_g = \frac{\omega}{c} \sqrt{\frac{\varepsilon}{\varepsilon + 1}} = k_{sp},$$

or more generally

$$k_x = \frac{\omega}{c} \sin \theta_0 \pm \Delta k_x = k_{sp} \quad (1.21)$$

where Δk_x , in Fig. 1.3, stems from any perturbation in the smooth surface; $\Delta k_x = 0$ gives no solution of the dispersion relation, Equation (1.14).

The reverse takes place too: SPs propagating along a gating or a rough surface can reduce their wave vector k_x by Δk_x so that the SP is transformed into light, see Figure 1.3, arrow 4 \rightarrow 5. This light emission, a consequence of the photon-SP coupling via roughness, plays an important role.

Surface plasmons also exist on curved surfaces, e.g., on spheres or cylinders [7]. In that case, the SPs are coupled and scattered by Δk_x resulting from the curvature. Since the resonant collective oscillation of the conduction electrons is limited to the small object, it is often called a “localized” plasmon. And the fields are enhanced at the curved surface. Resonance of localized surface plasmon around small cylinders will be discussed in more detail in Chapter 2 as one of the main features of the transmission spectrum.

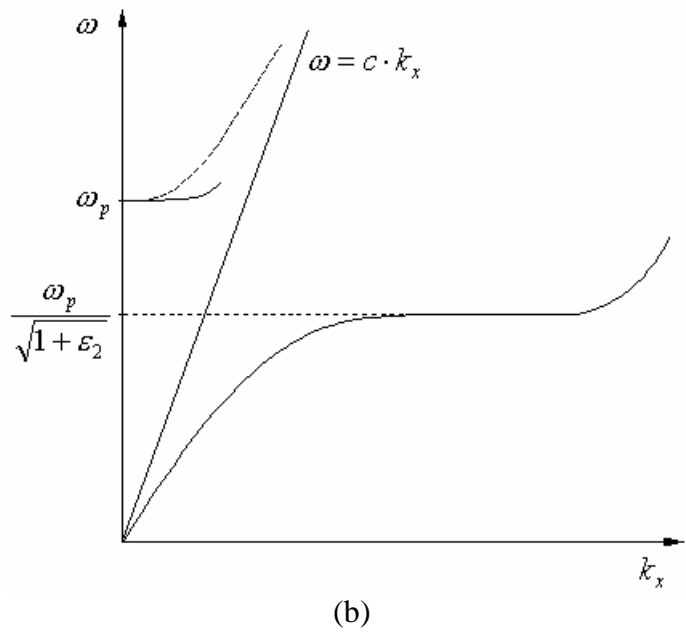
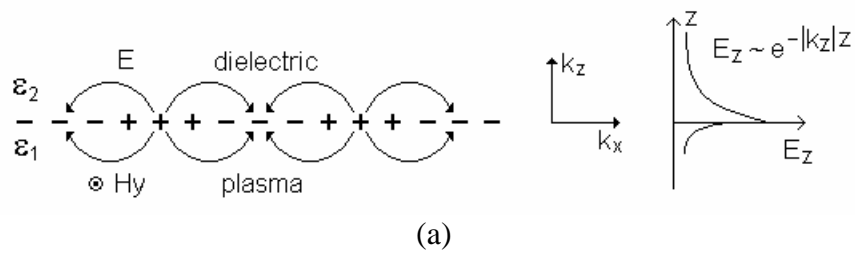


Figure 1.2. Surface plasmon waves on metal surface and the dispersion relations. (a) Schematic illustration of the charges and the electromagnetic field of SPs propagating on a surface in the x direction. The exponential dependence of the field E_z is seen on the right. H_y shows the magnetic field in the y direction of this p-polarized wave; (b) The dispersion relation of nonradiative SPs (—), right of the light line $\omega = ck_x$, on a metal surface coated with a dielectric film (ϵ_2). Radiative SPs (---), left of the light line, starts at ω_p . The dashed line (- - -), left of the light line, represents the dispersion of light in a metal: $\omega/k_x = c/|\epsilon_1|^{1/2}$ or in the case of free electrons $\omega^2 = \omega_p^2 + c^2k_x^2$. From Reference [7].

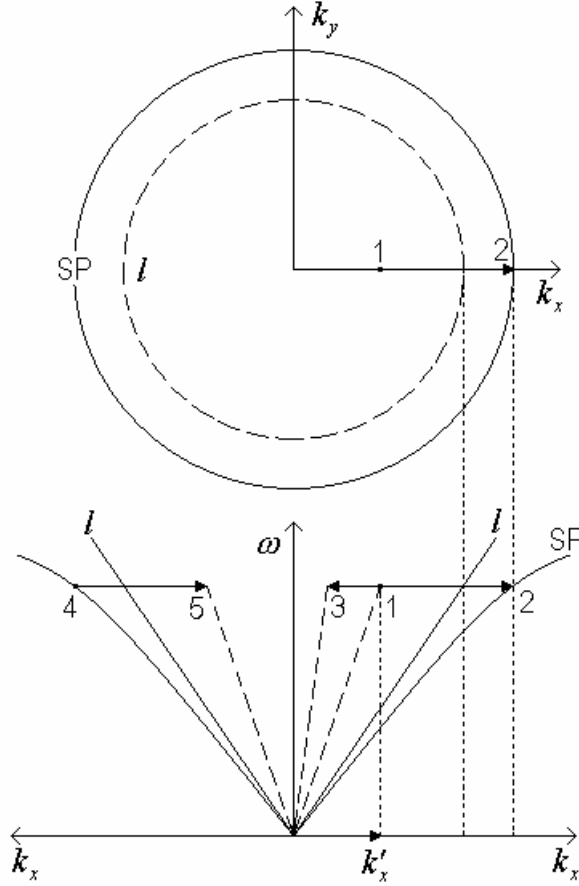


Figure 1.3. Grating coupling between light and SPs. SP: dispersion relation of SPs, l : light line. The incoming light, wave vector k'_x , point (1) is transformed into a SP, point (2), by taking up Δk_x . The interaction $1 \rightarrow 3$ via roughness leads to light scattered inside the light cone. The process $4 \rightarrow 5$ describes the decay of a SP into light via Δk_x ; it is the reverse of $1 \rightarrow 2$. Upper part: the full circle represents the values of $|k| = (k_x^2 + k_y^2)^{1/2}$ and the light circle (dashed circle) at $\omega = constant$ in the two-dimensional k space. From Reference [7].

1.4 SCATTERING AND ABSORPTION I INTERACTION OF LIGHT WITH METALLIC NANOSTRUCTURES

Effects of light interaction with matter are ultimately collective results of optical field interaction with atoms or molecules that compose the matter [5]. Thus, regardless of dimension scale of the matters, the underlying physics is the same for all systems. Reasoning down to atomic level, electric charges, electrons and protons, of atoms or molecules are set into oscillatory motion by the electric field of the incident wave. Electromagnetic energy will be radiated by the accelerated electric charges in all directions. Besides the reradiation of electromagnetic energy in such radiation scattering, the excited elementary charges may also transform part of the incident electromagnetic energy into other forms (e.g. thermal energy), a process called absorption. Therefore, all light-matter interactions can be analyzed starting from the basic scattering and absorption processes, including many familiar optical phenomena, such as reflection, refraction and diffraction, etc. The complex dielectric function underlies the scattering and absorption processes.

Once we obtain the dielectric function of metals, instead of treating optical processes by applying microscopic Maxwell's theory to electronic charges [8, Section 4.2], we can adopt a macroscopic approach to determine the absorption and scattering of electromagnetic waves by structural metals [5, Section 2.1]. $\epsilon(\omega)$ will directly count for both the constitution relations and boundary conditions. In studying optical properties of metallic nanostructures, the size dependence effects of dielectric function of metallic structures must be considered. As the dimensions for very small particles (< 5 nm) affect the electron-energy levels, the quantum-size

effects strongly determines the dielectric function. In the nano-regime of our interest ($10 \sim 10^2$ nm), the mean free path limitation of conduction electrons affects the $\varepsilon(\omega)$ more or less [5, 9], which comes from the electron collisions with the particle boundary [5, Section 12.1.6]. Usually, the effect of the mean free path limitation on the real part of the dielectric function is slight; the effect on the imaginary part is often substantial. For example, the ε'' of small silver particles near the Fröhlich frequency (fundamental plasmon resonance frequency) is found to have size dependence of

$$\varepsilon'' = 0.23 + \frac{26.4}{a}$$

where a is in angstroms. Thus, ε'' is enhanced by more than 10% for particles of radius 1000 \AA , and for a radius of about 115 \AA , ε'' is twice the bulk value. But in the visible and infrared wavelength regime, such size dependence is very weak for particle size of $\sim 10^2$ nm. The prominent features of scattering and absorption by such small single particles are the surface plasmon polaritons [9, Section 2.4.1]. They are, for spherical geometry, the multipole resonances of Mie's theory [2]. For other structures, similar characters appear while incorporated with shape anisotropy and polarization anisotropy. For radius $R \ll \lambda$, i.e., within the quasi-static approximation, a single resonance peak, the dipolar surface-plasmon, dominates the spectrum. This aspect for TM incidence on Ag thin cylinder will be discussed in detail in Chapter 2.

When such nanostructures are arranged together with separations much less than optical wavelength, optical response of the system cannot be simply considered as a superposition of

resulting scattering of the individual units; the inter-coupling between neighboring units will play a significant role, which is very different with the conventional cases. For disorderly arranged systems, observed are the collective/effective behavior of the superpositions and inter-couplings. For orderly arranged nanostructure arrays, as we study in this work, the properties are biased with clear characteristics because of the uniform constructive and destructive superposition and resonant inter-coupling, such as grating coupled in-plane surface plasmon resonance to be discussed in Chapter 2.

1.5 FDTD NUMERICAL SIMULATION METHOD

The interactions of light with the metal nanostructures are numerically analyzed by electromagnetic simulation using the finite-difference time-domain (FDTD) method [10, 11]. Since the problems we deal with are mostly two-dimensional (2D) grating-like metallic structures, and the phenomena are closely related to surface plasmons, TM-polarized incidence light are considered in solving the Maxwell's equations:

$$\frac{\partial \vec{D}}{\partial t} = \nabla \times \vec{H} \quad (1.22a)$$

$$\vec{D}(\omega) = \varepsilon_0 \varepsilon(\omega) \cdot \vec{E}(\omega) \quad (1.22b)$$

$$\frac{\partial \vec{H}}{\partial t} = -\frac{1}{\mu_0} \nabla \times \vec{E} \quad (1.22c)$$

where all parameters have their traditional meaning. It is noted that: (1) we consider all nonmagnetic materials; (2) there is no conduction current ($\bar{J} = 0$), but local displacement current is nonzero. For simplicity, the Maxwell's equations can be normalized into the "Gaussian units" system by substituting [10]

$$\tilde{\bar{E}} = \sqrt{\frac{\epsilon_0}{\mu_0}} \bar{E}; \quad \tilde{\bar{D}} = \sqrt{\frac{1}{\epsilon_0 \mu_0}} \bar{D}.$$

Then, Maxwell's equations become

$$\frac{\partial \tilde{\bar{D}}}{\partial t} = \frac{1}{\sqrt{\epsilon_0 \mu_0}} \nabla \times \bar{H} \quad (1.23a)$$

$$\tilde{\bar{D}}(\omega) = \epsilon(\omega) \cdot \tilde{\bar{E}}(\omega) \quad (1.23b)$$

$$\frac{\partial \bar{H}}{\partial t} = -\frac{1}{\sqrt{\epsilon_0 \mu_0}} \nabla \times \tilde{\bar{E}}. \quad (1.23c)$$

When we get to three-dimensional simulation, we will wind up dealing with six different fields:

\tilde{E}_x , \tilde{E}_y , \tilde{E}_z , H_x , H_y , and H_z . In doing two-dimension TM simulation in our case, we take

components $(H_z; \tilde{E}_x, \tilde{E}_y)$, which we will still write as $(H_z; E_x, E_y)$ for convenience. See

Figure 1.4(a) for the polarization and structure geometrical relations. Thus, the Maxwell

equations can also be reduced to

$$\frac{\partial H_z}{\partial t} = -\frac{1}{\sqrt{\varepsilon_0 \mu_0}} \left(\frac{\partial E_y}{\partial x} - \frac{\partial E_x}{\partial y} \right) \quad (1.24a)$$

$$D_x = \varepsilon(\omega) \cdot E_x(\omega); \quad D_y = \varepsilon(\omega) \cdot E_y(\omega) \quad (1.24b)$$

$$\frac{\partial D_x}{\partial t} = \frac{1}{\sqrt{\varepsilon_0 \mu_0}} \frac{\partial H_z}{\partial y} \quad (1.24c)$$

$$\frac{\partial D_y}{\partial t} = -\frac{1}{\sqrt{\varepsilon_0 \mu_0}} \frac{\partial H_z}{\partial x} \quad (1.24d)$$

It is noted that, unless specified, all interactions between light and 2D metallic grating structures in this thesis will have TM-polarization incidence as defined in Figure 1.4(a).

1.5.1 Discretization

Equations (1.24) are discretized using Yee's algorithm in a two-dimension problem space, as illustrated in Figure 1.4(b). The corresponding finite difference equations are shown below:

$$\frac{H_z^{n+1/2}(i, j) - H_z^{n-1/2}}{\Delta t} = -\frac{1}{\sqrt{\varepsilon_0 \mu_0}} \left(\frac{E_y^n(i + 1/2, j) - E_y^n(i - 1/2, j)}{\Delta x} - \frac{E_x^n(i, j + 1/2) - E_x^n(i, j - 1/2)}{\Delta y} \right) \quad (1.25a)$$

$$\frac{D_x^{n+1}(i, j + 1/2) - D_x^n(i, j + 1/2)}{\Delta t} = \frac{1}{\sqrt{\varepsilon_0 \mu_0}} \frac{H_z^{n+1/2}(i, j + 1) - H_z^{n+1/2}(i, j)}{\Delta y} \quad (1.25b)$$

$$\frac{D_y^{n+1}(i + 1/2, j) - D_y^n(i + 1/2, j)}{\Delta t} = -\frac{1}{\sqrt{\varepsilon_0 \mu_0}} \frac{H_z^{n+1/2}(i + 1, j) - H_z^{n+1/2}(i, j)}{\Delta x} \quad (1.25c)$$

1.5.2 Stability

An electromagnetic wave cannot propagate faster than the speed of light in free space. To propagate a distance of one cell requires a minimum time of $\Delta t = \Delta x / c_0$. When we get to two-dimensional simulation, we have to allow for the propagation in the diagonal direction, which brings the time requirement to $\Delta t = \Delta x / (\sqrt{2}c_0)$. Generally, for n-dimensional simulation, the criterion was summarized with the well-known ‘‘Courant Condition’’ [10]:

$$\Delta t \leq \frac{\Delta x}{\sqrt{n} \cdot c_0}$$

In our two-dimension system, Δt is determined by

$$\Delta t = \frac{\Delta x}{2 \cdot c_0} \quad \text{or} \quad \frac{\Delta t}{\Delta x} \cdot \frac{1}{\sqrt{\epsilon_0 \mu_0}} = \frac{1}{2} \quad (1.26)$$

1.5.3 Absorbing Boundary Conditions (ABC)

Usually, the size for the area that can be simulated using FDTD is limited by computer resources. As the wave propagates and impinges onto the edge of the allowable space, reflections

will be generated that would go back to the problem space and mess up the real wave and field distribution. Thus the ABCs are necessary to be introduced to absorb or eliminate the waves coming to the edges. Among many approaches, the perfectly matched layer (PML) is most flexible and efficient [10]. The basic idea is to introduce an artificial lossy media with non-reflection. It's known that if a wave propagating in medium A impinges upon medium B, the amount of reflection is dictated by the intrinsic impedances of the two media

$$\Gamma = \frac{\eta_A - \eta_B}{\eta_A + \eta_B}$$

where $\eta = \sqrt{\mu/\varepsilon}$ is determined by the dielectric constants ε and permeabilities μ of the two media. As a wave propagates into the PML media, the dielectric constant changes gradually from ε_1 , that inside the problem region, to ε_i , and at the same time μ also changes with ε so that η remains a constant. Then Γ would be zero and no reflection would occur. The ε and η are also made to be complex for attenuation.

In doing so, the ABC can still not be considered as really perfect. A certain portion of the impinging wave is still reflected back into the problem space. To minimize the load on the ABCs, the incident field should be subtracted from the total field. As illustrated in Figure 1.5, in the two-dimensional field every point in the problem space is either in the total field or it is not; no point lies on the border. Therefore, if a point is in the total field but it uses points outside to calculate the spatial derivatives when updating its value, it must be modified. The same is true of

a point lying just outside that uses points inside the total field. There are three places that must be modified for the TM case:

- (1) The H_z values at $j = ja$ and $j = jb$:

$$H_z(i, ja) = H_z(i, ja) + 0.5 \cdot E_x_inc(ja - 1/2)$$

$$H_z(i, jb) = H_z(i, jb) - 0.5 \cdot E_x_inc(jb - 1/2)$$

- (2) The D_x values just outside $j = ja$ and $j = jb$:

$$D_x(i, ja - 1/2) = D_x(i, ja - 1/2) - 0.5 \cdot H_z_inc(ja)$$

$$D_x(i, jb + 1/2) = D_x(i, jb + 1/2) + 0.5 \cdot H_z_inc(jb)$$

- (3) The D_y values just outside $i = ia$ and $i = ib$:

$$D_y(ia - 1/2, j) = D_y(ia - 1/2, j) + 0.5 \cdot H_z_inc(j)$$

$$D_y(ib + 1/2, j) = D_y(ib + 1/2, j) - 0.5 \cdot H_z_inc(j)$$

where the (E_x_inc, H_z_inc) are field components of generated incidence wave.

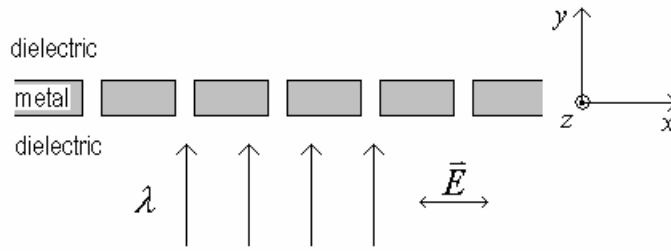
1.5.4 Metal Surface Boundary Conditions

Since the dimensions of our metallic (Ag) structures are much larger than the skin depth of visible light, the perfect electric conduction (PEC) boundary conditions were applied at metal surfaces as approximations:

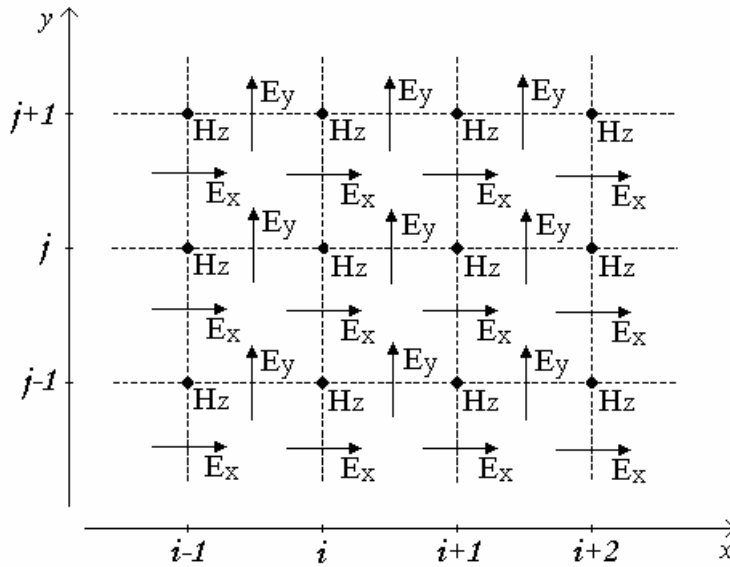
$$\vec{n} \times \vec{E} = 0 \quad \text{or} \quad \vec{E}_{\text{tangential}} = 0 \quad (1.27)$$

$$\vec{n} \cdot \vec{H} = 0 \quad \text{or} \quad \vec{H}_{\text{normal}} = 0 \quad (1.28)$$

where \vec{n} is the normal vector at metal surfaces. Alternatively, the surface impedance boundary conditions (SIBC) would be a better approximation for the boundary conditions [11]. As the metal dimensions are small (≤ 50 nm), all parts of the metal object is strongly dynamic-polarized by incidence optical field, the dipole approximation can be applied inside metal to simulate the energy dissipation due to charge density oscillation [12].



(a)



(b)

Figure 1.4. Two-dimensional discretization of TM-polarized light incidence on metallic slab with narrow slits using Yee's algorithm. (a) Schematic illustration of TM-polarization incidence and structure geometry relations. (b) Field and structure discretization using Yee's algorithm [11].

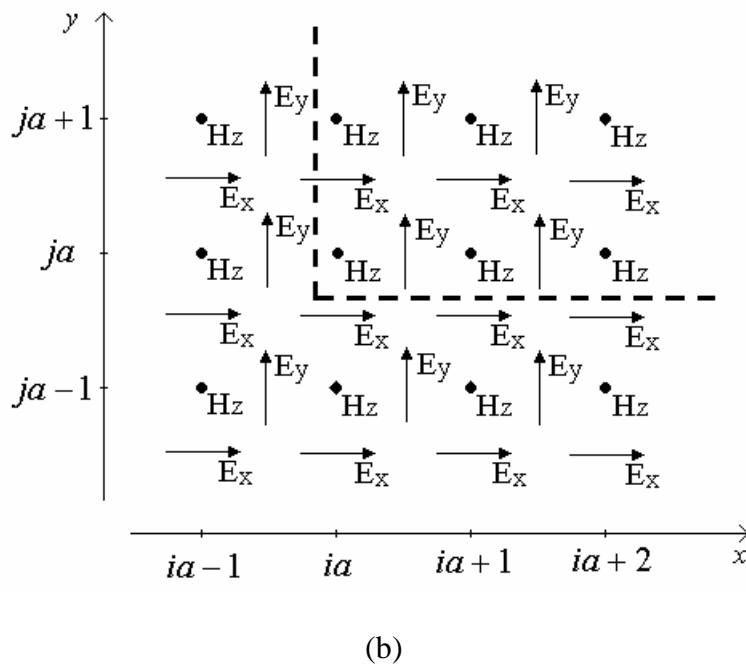
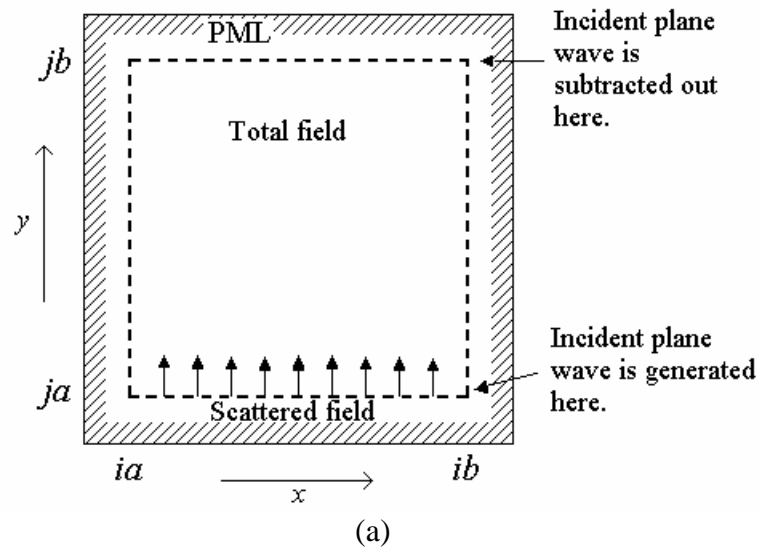


Figure 1.5. Minimization of load on absorbing boundary conditions (ABCs). (a) Total field/scattered field of the two-dimensional problem space. (b) Every point is in either the total field or the scattered field.

1.6 SUMMARY

- Significant interests exist in studying light interaction with nano/subwavelength-structured metallic materials from both science and technology point of view.
- Optical excitation of metal usually results in electron charge density oscillation. Due to the strong attenuation of light inside metals, surface plasmon (SP) wave modes are the main feature of metal optics.
- Interaction of light with a nano-structured metal can result in modulation of light in near and far fields.
- Numerical simulation using FDTD method is very helpful for understanding and analyzing the plasmonic phenomena.

2.0 TRANSMISSION OF LIGHT THROUGH NARROW SLITS IN THICK METALLIC GRATINGS

2.1 INTRODUCTION

Optical transmission through subwavelength apertures has been drawing strong interest especially in the context of near-field optics. According to Bethe's theory [13], the transmission of light (wavelength λ) through a single hole (diameter $d < \lambda$) in a smooth metal film, with its thickness greater than the optical skin depth, scales as $(d/\lambda)^4$. However, if the holes are formed into 2D periodic arrays in a metal film, extraordinary optical transmission can be obtained at wavelengths up to 10 times larger than the diameter of the holes [14-19]. Since the experimental observation, optical interaction in nano-apertured metal layers has been gaining increasing attention from the science and applications aspects. Strong confinement and transmission of light in the subwavelength aperture arrays are expected to find many applications in optics and optoelectronics, and these properties, when incorporated into photonic crystal structures, may lead to new functionalities that are complementary to those obtainable from the dielectric-based photonic bandgap structures.

In exploring mechanisms for such an extraordinary transmission, 1D thick transmission metallic gratings with very narrow slits are mostly studied with simulations and analytical models [20-25]. And near 100 % transmission of TM-polarized light has been predicted through

subwavelength slit arrays [22]. Mechanisms of the extraordinary transmission through slit arrays, however, are still not clearly understood and had been a subject of debate. While some features of the transmission characteristics of 1D slit arrays can be deduced from that of 2D aperture arrays, 1D slit arrays clearly differ from 2D aperture arrays. For example, propagating modes are supported by a slit structure but not in a hole aperture formed in metal, and this is considered one of the key factors that differentiate their transmission properties. The mechanism proposed in the earlier work with 1D slit arrays is that light transfers from the upper surface to the lower one by the excitation of coupled surface plasmons (SPs) on both surfaces of the metallic grating or by the coupling of incident waves with waveguide resonances located in the slits [22]. Later, Cao and Lalanne also argued it that SPs are most strongly excited near the Wood-Rayleigh anomalies and are most weakly excited at the transmission maxima [24]. They also argued that SPs play a negative role in the transmission anomalies in slit arrays and that the transmission enhancement is due to a combination of strongly excited waveguide and diffraction modes in slit arrays. Treacy has also argued that the transmission anomalies can be explained in terms of a dynamical diffraction theory, in which SPs are an intrinsic component of the diffracted wave fields. It is argued that both propagating and evanescent modes (traditional surface plasmons) of Bloch waves are strongly excited at both the peak and the minimum transmission conditions [21].

While some of the issues in this debate may sound a matter of semantics, it is evident that the role of surface plasmons in optical transmission remains as the key issue. Most of the reported work regarding the 1D slit arrays are theoretical investigations based on numerical analysis, and there has been lack of experimental work that can directly verify the theoretical predictions or guide theoretical study for new mechanisms that may be involved. This might be

partly ascribed to the difficulty in forming very narrow, subwavelength slit arrays in metallic films, especially for the visible or shorter wavelength range [26]. Until recently, we formed 1D metallic (Ag, Al) gratings with narrow slits on quartz substrates [27]. An experimental study of optical transmission/reflection through 1D slit arrays were reported and the results were compared with theoretical analyses of surface plasmon interactions in nano-apertured metal layers. We concluded that the surface plasmon resonance is responsible for the observed transmission minima, involving two different modes of interaction with the 1D slit arrays: 1) the SP resonance along the planes that comprise either the metal/air or metal/substrate interfaces, and 2) the SP resonance localized along the surface that encloses each metal island separated by slits. In the following sections, more details and extensions of this work will be shown and discussed.

2.2 FABRICATION OF ONE-DIMENSIONAL THICK METALLIC GRATINGS WITH NARROW SLITS

Figure 2.1 shows scanning electron microscope (SEM) images of the silver 1D grating structure with narrow slits formed on a quartz substrate. Basically, a holographic lithography technique was utilized in defining the 1D grating patterns on Cr-coated quartz substrates; A two-step dry etching process was then performed to transfer the photoresist grating patterns onto Cr and then onto quartz using the Cr layer as an etch mask. 1D array of mesa structures with near-vertical sidewalls were formed on quartz with process. And then the Ag was angle-deposited on the mesa surface with thermal evaporation. The as-formed Ag slit arrays could have an adjustable thickness up to 400 nm, slit width of 30-100 nm along the depth, and period down to

UV wavelength range. Figure 2.2 is a schematic process flow of this technique. And the angled deposition process is specifically shown in Figure 2.3.

So far, in technology, lithography with photoresist (PR) is the only controlled mature technique used for mass fine patterning. But metal like silver (Ag) is a hard material for dry etching using the fine thin photoresist (PR) patterns as etch mask, especially as the Ag film thickness is thick (> 200 nm). Wet chemical etching is typically not favorable for fine etching because of its strong under-etching using PR as etch mask. Thus we developed the indirect method forming thick Ag gratings with very narrow slits.

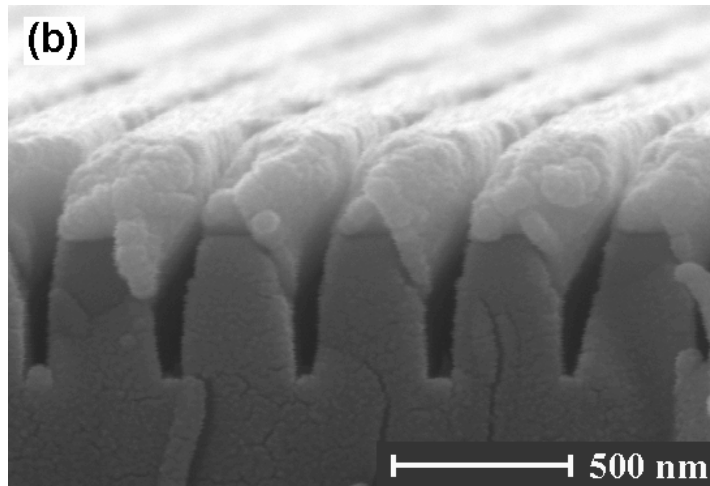
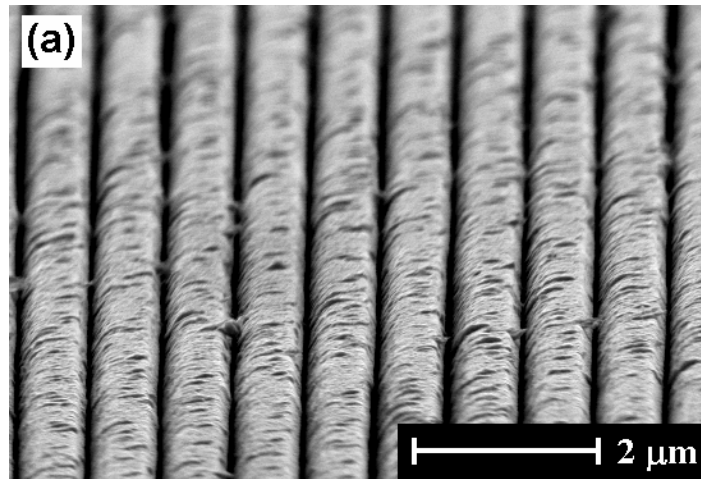
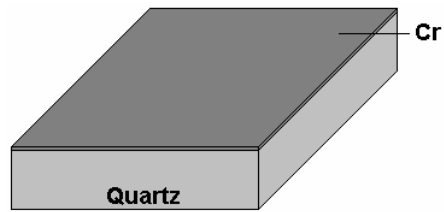
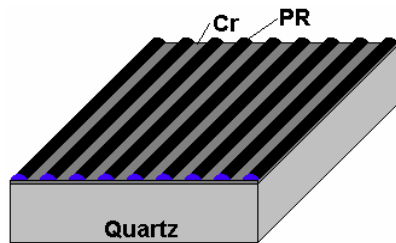


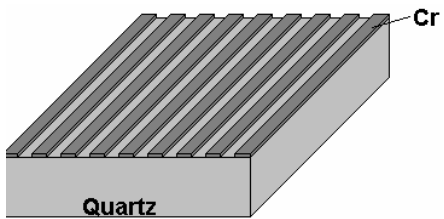
Figure 2.1. SEM micrographs of a silver 1D grating structure with subwavelength slits formed on a quartz substrate using holographic lithography and angled deposition. (a) Top view of a Ag 1D slit array with grating period of 780 nm and Ag thickness of 400 nm. (b) Side view of a Ag 1D slit array with grating period of 370 nm and Ag thickness of 250 nm. Opening of slits is clearly revealed with slit width in the range of 30-100 nm along the depth.



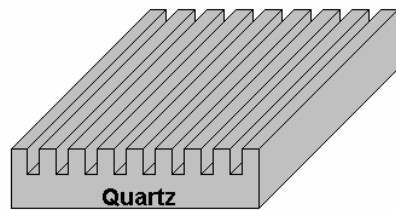
(a) Thin Cr film deposition on planar quartz substrate



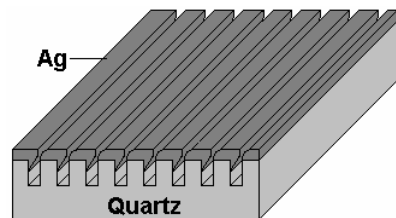
(b) Photoresist grating patterning



(c) Transferring photoresist grating patterns onto Cr by RIE etching



(d) Deep etching of quartz substrate using Cr grating pattern as mask



(e) Angled-deposition of Ag film onto etched quartz grating mesa

Figure 2.2. Schematic process flow forming 1D thick metallic gratings with narrow slits. (a)-(b)-(c)-(d)-(e) in sequence.

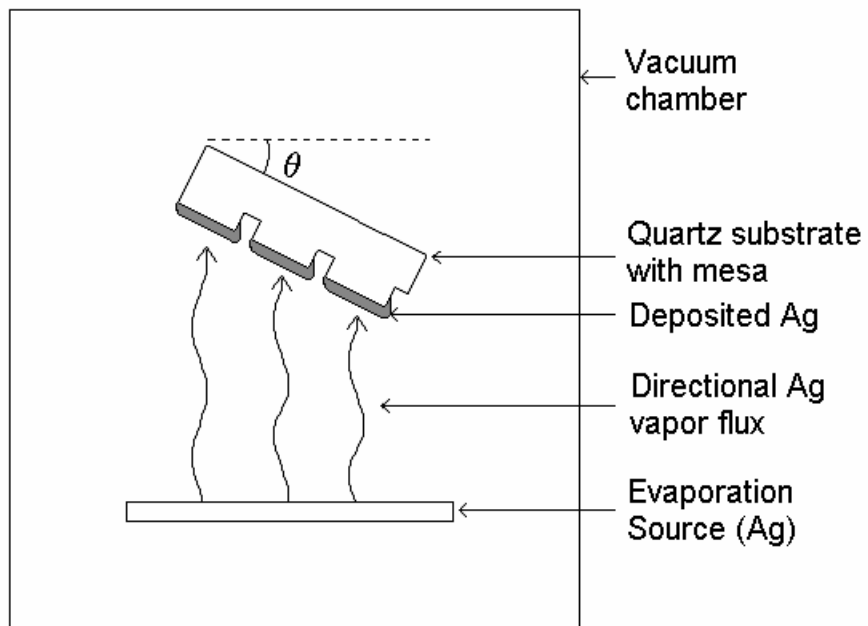


Figure 2.3. Angled-deposition of Ag onto quartz substrate with mesa using thermal evaporation.

2.3 CHARACTERIZATION AND ANALYSIS OF THE OPTICAL TRANSMISSION SPECTRUM

2.3.1 Characterization

The optical transmission through the Ag slit arrays was measured at a spectral range of 350 ~ 1750 nm. As shown in Figure 2.4(a), a beam from a multimode fiber (core diameter of 62.5 μm and a numerical aperture of 0.20) connected to an unpolarized white light source was normally incident to a Ag slit array from the substrate side. The zero-order transmission through a slit array was collected with another multimode fiber placed close to the Ag layer surface (with 3 ~ 5 μm gap), and was then characterized with an optical spectrum analyzer. The transmission measurement was repeated with a dummy sample that has the same mesa-etched quartz structure but without a Ag layer. The transmission through a Ag slit array was then calculated by dividing the spectrum obtained from a real sample by the one from the dummy, a process designed to avoid (or alleviate) the effects of involving a mesa-etched quartz substrate structure and an optical fiber on the measured transmission spectra. Theoretically, as the wavelength is larger than two times of the mesa grating period, scattering effects of the mesa are very minor.

In studying the mechanisms of the zero-order transmission, we also characterized the angular dependence of both transmission and specular reflection at a fixed wavelength (633 nm) using a He-Ne laser, as shown in Figure 2.4(b). The linearly polarized collimated beam (diameter of ~ 3 mm) was directly incident on the Ag side. Both transmitted and reflected lights were

collected in far field by a Ge detector (power acceptance area diameter of $\sim 1\text{cm}$) connected to an optical power meter.

2.3.2 Spectrum Analysis

Figures 2.5 and 2.6 show the typical transmission spectra of the Ag slit arrays with grating periods of 370 nm and 780 nm. Our experiments and analysis will focus on the one with grating period of 370 nm because of our interests in the visible range filtering properties. The two samples of Figure 2.5 have a grating period of 370 nm and Ag thickness of 120 nm and 200 nm. Measured at normal incidence, the peak transmission of approximately 30 and 15 % is observed from the 120-nm and 200-nm-thick samples, respectively. Considering that the incident beam is unpolarized and the TE polarization component does not transmit through such narrow slit arrays, the maximum transmission for TM polarization is estimated to be around 60 %. This corresponds to $\sim 500\%$ transmission efficiency, which is defined as the optical power transmitted through a slit divided by the incident power impinging upon the slit area. The main peak shifts from 660 to 690 nm as the Ag layer thickness is increased from 120 to 200 nm. The peak width also noticeably increased with the increased Ag thickness. This behavior, i.e., the main peak's red-shift and the peak width increase, is the opposite of the 2D aperture arrays case, in which the main peak initially blue-shifts with reduced peak-width and then the peak position and width remain constant as the metal thickness is further increased [30]. In an analytical study of the optical transmission through a 2D aperture array, the initial regime that shows a blue-shift is modeled by the evanescent coupling of the two surface plasmons at the top and bottom

surfaces of a metal layer and the second regime is by decoupled SPs [19]. The tendency observed in our work is rather consistent with the simulation results based on the model that involves the propagating modes in a slit in explaining the optical transmission through a slit array [25]. The difference between the 1D and 2D aperture arrays characteristics strongly suggests that different mechanisms are involved in transmitting the light through 1D slit arrays and 2D aperture arrays. As red shift of the main peak for samples with grating period of 780 nm is also obvious in Figure 2.6, the peak broadening with increasing Ag thickness is not shown. Thus the physics inhabited in the “simple” structure and material system is rather complex. At least mechanisms responsible for such spectra include these effects:

- 1) Guiding of propagating modes through the narrow slits;
- 2) Diffraction, scattering and coupling of light and surface plasmon at the sharp edges of metal surface.
- 3) The SP resonance along the planes that comprise either the metal/air or metal/substrate interfaces and
- 4) The SP resonance localized around the Ag stripes, as mentioned previously; and there may be
- 5) Fabry-Perot type resonance inside the slit when the Ag layer is thick enough, comparable to the wavelength of light or more.

These effects behave differently in a macroscopic analysis, but ultimately all of them are effects stemming from scattering and absorption of light by the structures in same or different regimes.

Figure 2.6 also clearly shows that the filtering effects of the narrow slit arrays are becoming apparent as the Ag thickness increases and slit width decreases. This can be

understood as the above effects coming to play their roles in a way that the SP resonances form the minima at a transmission (through a metal/air effective media) background, and constructive scattering enhances transmission at the main peak. The low transmission at short wavelengths in Figure 2.6 is speculated to result from densely distributed SP resonance modes (both in-plane SP and localized SP), strong mode coupling and non-zero-order scattering/diffraction by substrate mesa gratings, as the wavelengths are shorter than the grating period. In this thesis, we will focus on the main feature, low-order of the effects to analyze the spectra. Below is a further extension of this general analysis and detailed discussions are in the following sections of this chapter.

The transmission spectra in Figure 2.5 show three major dips. The minimum transmission point at around 580 nm tends to stay at nearly the same position for the raised metal thickness, although the exact location cannot be resolved due to an overlap with a neighboring peak. This insensitivity to metal thickness suggests that the phenomenon occurring at this minimum transmission point involves an interaction of light primarily with the top or bottom surfaces of metal but not the sidewalls of slits. The SP resonance along the plane that comprises the metal/substrate interface of each metal island is expected to occur at 600 nm wavelength of light, based on a calculation using the formula:

$$\lambda = \frac{d_g}{m} \sqrt{\frac{\varepsilon_d \varepsilon_m}{\varepsilon_d + \varepsilon_m}}, \quad (2.1)$$

which can be derived from Equation (1.14). Here, d_g is the grating period; m is the order of the grating vector involved in SP coupling, shown in Equation (1.21); and ε_m and ε_d are the

dielectric constants of metal and the adjacent dielectric (i.e., a quartz substrate in this case), respectively. Let's take the dielectric constant values of silver to be $-12 + i0.9$ at wavelength of 580 nm and $-4 + i0.7$ at wavelength of 400 nm [6], and the dielectric constant of quartz to be 2.16. Then, the wavelength calculated for $m = 1$ reasonably well matches the minima at around 580 nm observed in Figure 2.5. Similarly the transmission minimum at around 430 nm well corresponds to the SP resonance at the air/metal interface, which is expected to occur at 430 nm according to Equation (2.1), although an exact position cannot be clearly resolved due to an overlap with the bulk plasmon wavelength (~ 360 nm) at which a metal film is significantly transparent.

It should also be noted that the sample with 120-nm-thick Ag shows a clear, well-defined major dip at around 800 nm, which corresponds to significantly longer wavelength than that of the transmission minima related to the metal/substrate interface. Considering that a slit structure allows propagating modes (or vertical SPs along the slit walls), it would be possible that the SP waves on the top and bottom surfaces of a metal island couple to each other via the slit's sidewall. The SPs are then expected to resonate along the island surface, i.e., the periphery of metal cross-section when the following condition is satisfied along the close loop.

$$\oint k_{sp} \cdot dr = 2\pi m \quad (2.2)$$

Here, m is an integer, and k_{sp} is the SP wave vector and can be expressed as

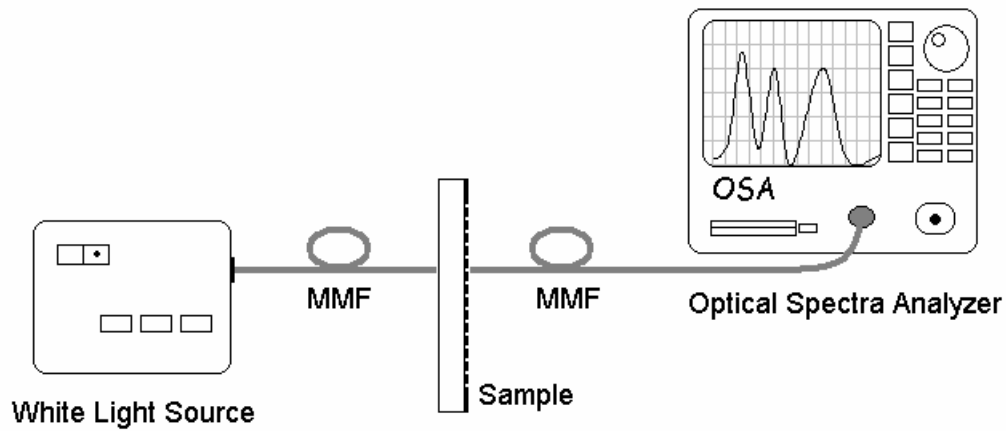
$$k_{sp} = \left(\frac{2\pi}{\lambda_0} \right) \left(\frac{\epsilon_m \epsilon_d}{\epsilon_m + \epsilon_d} \right)^{1/2}, \quad (2.3)$$

where λ_0 is the free-space wavelength of incident light. Along the periphery of metal cross-section, the magnitude of the SP wave vector k_{sp} varies depending on the dielectric material interfacing with a metal, i.e., either air or quartz in this case. Due to the irregular geometry of the metal cross-section, it is not straightforward to calculate the total phase change along the periphery. If we assume a simple geometry of circular cross-section with radius r_0 surrounded by a homogeneous dielectric, the resonance condition, Equation (2.2), is reduced to $k_{sp} \cdot r_0 = m$. If we take an approximation that $r_0 = 110\text{nm}$ and 30 % of the metal periphery interfaces with silica and the rest with air, the resonance wavelength is calculated to be 820 nm for the dipolar resonance case, i.e., $m = 1$. Here, the dielectric constant of $-29 + i1.7$ is assumed for Ag at wavelength of 820 nm [6], and the plasmon coupling between metal islands is neglected. This number closely matches the location of the transmission dip (~ 800 nm) of the sample with 120-nm-thick Ag as shown in Figure 2.5. The minimum transmission point shifts to longer wavelength as the metal thickness is increased. This behavior is also consistent with the resonance condition discussed above. It is important to note that this surface plasmon resonance is a phenomenon highly localized at each metal island and differs from the SP resonance that occurs along the planes that comprise either the top or bottom surfaces of an array of metal islands. This localized SP resonance reminisces the electron orbital of atoms [12]. Well-defined transmission minima have been observed with metal particles of variable sizes and the anomaly has been ascribed to the localized SP resonance in metal spheres [32].

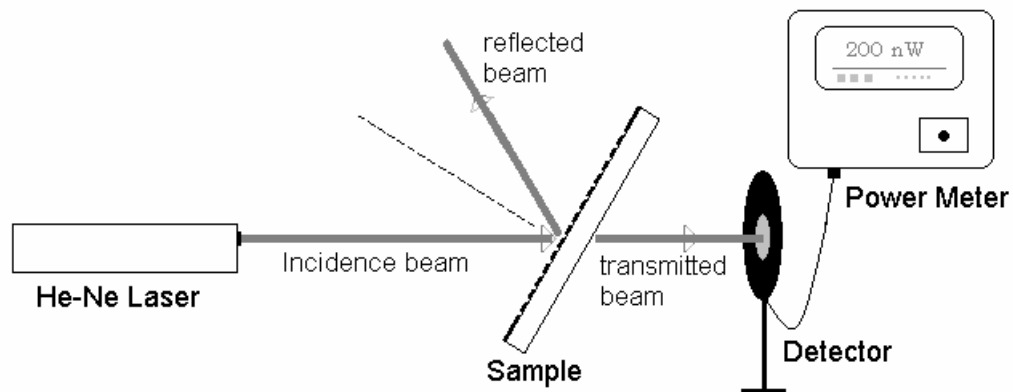
Similar calculations were applied to the thick samples with grating period of 780 nm in Figure 2.6, and the transmission minima were well matched by the resonance conditions. Overall, the results strongly suggest that the three major transmission minima observed in this work can be ascribed to the SP resonances that involve different sections of the metal surfaces. In order to consolidate this observation, we have characterized the angular dependence of both transmission and reflection at a fixed wavelength (633 nm) using a He-Ne laser. For a TM polarized light at this wavelength, the transmission shows a minimum when the incidence angle is ~ 45 degrees (the dashed curve in Figure 2.7). This angular position well matches the value (43 degrees) that is calculated from the condition for SP excitation at the plane that comprises the metal/substrate interfaces, i.e., $k_{sp} = k_0 \cdot \sin \theta \pm m \cdot k_g$, where k_0 is the wave vector of an incident beam, θ is the incidence angle measured from the substrate normal, and k_g is the grating vector. It is interesting to note that the reflection (solid curve) shows a maximum with a sharp peak profile (with the full-width-half-maximum of $2 \sim 3$ degrees) near the SP resonance point. The power loss, calculated as the difference between the incident power and the transmitted plus reflected power, is minimal at this point. The narrow reflection peak observed in here is ascribed to the close proximity of the SP resonance point and the diffraction related Wood's anomaly point.

From this analysis, the surface plasmon resonances (in-plane SP and localized SP) are found responsible for the observed transmission minima. At these resonance points, no net-power flows along the metal surfaces and thus no funneling of incident power into a slit region. The incident power is then strongly reflected back from the metal surface without incurring any major loss of power [21]. If the slits are sufficiently deep, resonance may occur in the vertical slit region itself, which forms a Fabry-Perot type cavity for SPs. Peak transmission is then expected

at this resonance point under the condition that no simultaneous resonance of surface plasmons occurs along the top or bottom surfaces of the metal island arrays. At long wavelengths that all these resonances become impossible, it behaves like an absorptive effective media composed of metal and air (or dielectric filled inside slits). The transmission is then depending on the thickness of the effective media and behaves like that of an ordinary absorptive material slab.



(a)



(b)

Figure 2.4. Set-up for optical characterization of Ag subwavelength gratings with narrow slits. (a) Characterization of zero-order transmission spectrum in the wavelength range of 350 ~ 1750 nm. (b) Characterization of angular dependent transmission and specular reflection at fixed wavelength (633 nm).

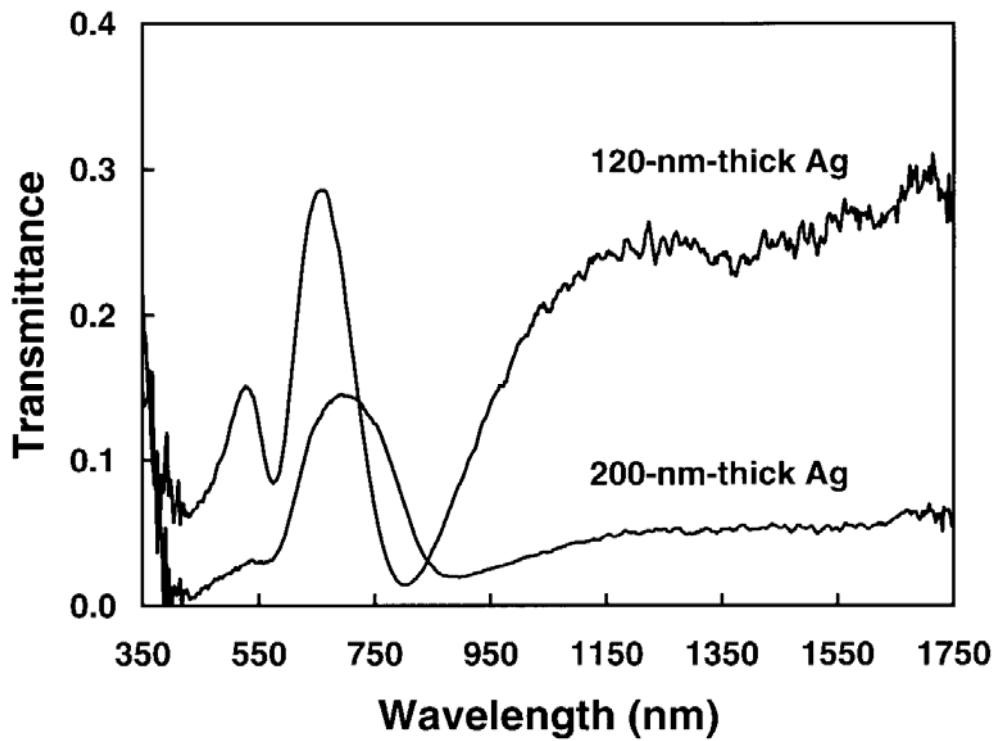


Figure 2.5. Transmission spectra of 1D slit array samples with grating period of 370 nm and with 120- or 200-nm-thick Ag. The input beam was incident normal to the Ag side surface. Peak transmission of over 30 % is observed from the 120-nm-thick Ag sample. Considering that the incident beam is unpolarized and the TE polarization component does not transmit through a slit array, the peak transmission is estimated to be over 60 % for TM polarization.

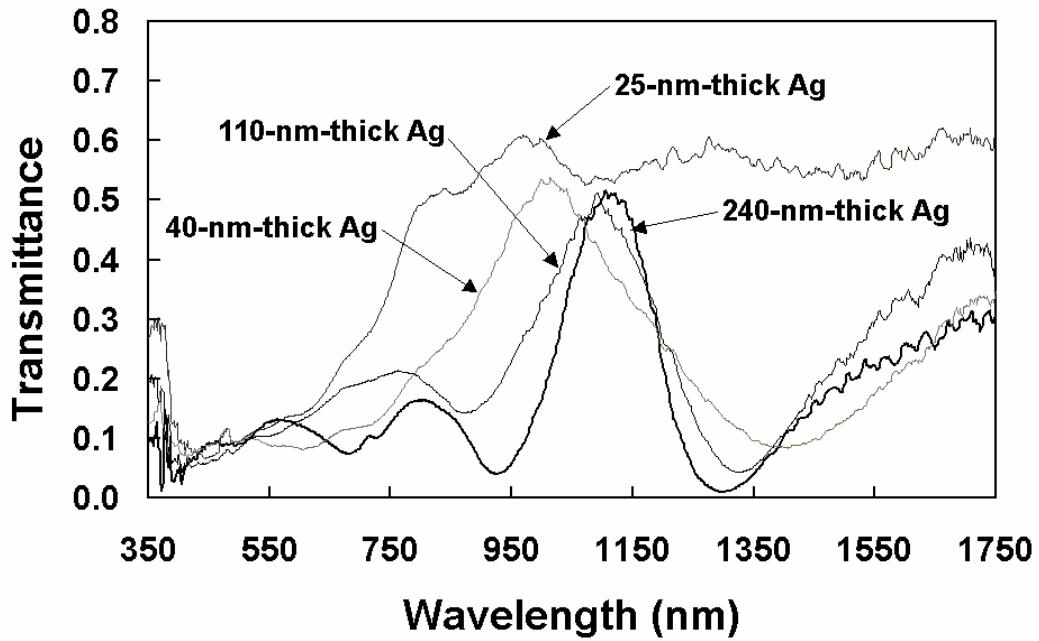


Figure 2.6. Transmission spectra of 1D slit array samples with grating period of 780 nm and Ag of different thickness. The input beam was incident normal to the Ag side surface. The filtering effects come to appear with the increasing of Ag thickness (\gg Ag skin depth \sim 20 nm) and decreasing of slit width.

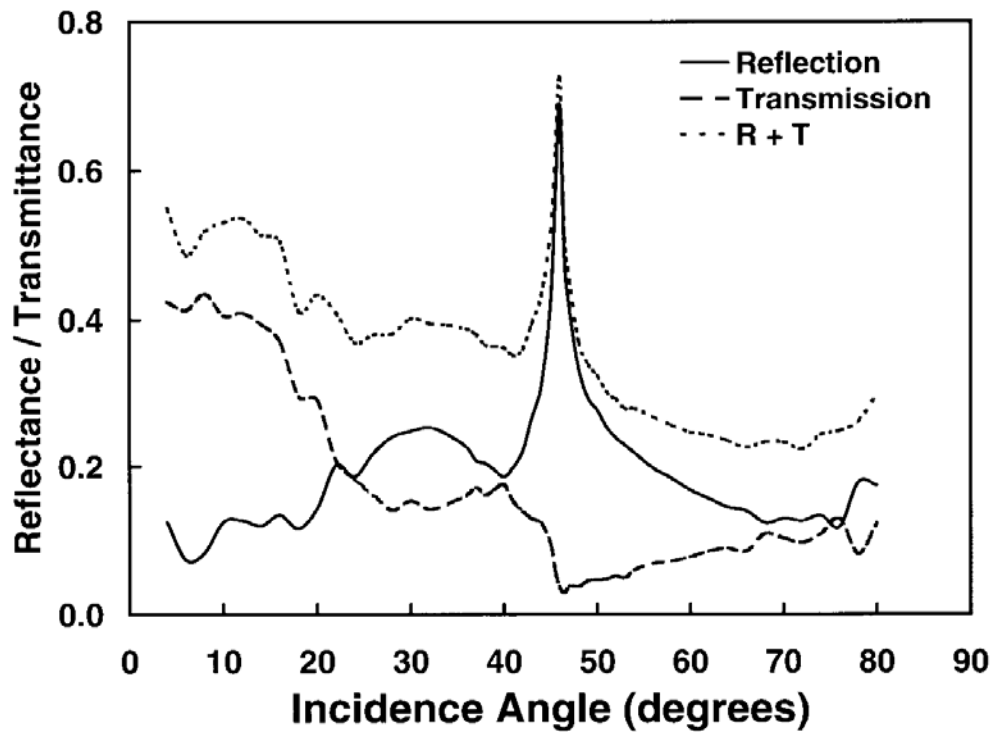


Figure 2.7. Transmission and reflection measured as a function of incidence angle at the wavelength of 633 nm (TM polarized). The sample used is the one with 120-nm-thick Ag shown in Figure 2.5. The transmission profile (dashed curve) shows a minimum at ~ 45 degrees whereas the reflection (solid curve) shows a maximum at the same incidence angle. The power loss, estimated from the difference between the incident power and the transmitted plus reflected power, is minimal at around the surface plasmon resonance point, as shown in the dotted curve.

2.4 GUIDING OF LIGHT WITH PLASMON MODE THROUGH NANOMETER- WIDTH SLIT IN THICK METALLIC SLAB

Unlike the case of a small hole (diameter \ll wavelength) in thick metal slab (which has a cut-off for propagation mode [33]), theoretically there is no cut-off for a slit in thick metal slab (no matter how narrow the slit is). There is always a fundamental TM mode. When the slit width is very narrow (\ll wavelength), the TM mode is strongly determined by the metal/dielectric interface state. Thus, we cannot analyze such a situation by directly applying perfect electric conductor (PEC) boundary conditions, which assumes tangential component of E-field and normal component of H-field inside metal is zero. A complete set of boundary conditions (B.C.) for monochromatic wave in steady state is

$$\bar{n} \cdot (\bar{D}_2 - \bar{D}_1) = \sigma_s, \quad (2.4a)$$

$$\bar{n} \times (\bar{E}_2 - \bar{E}_1) = 0, \quad (2.4b)$$

$$\bar{n} \cdot (\bar{B}_2 - \bar{B}_1) = 0, \quad (2.4c)$$

$$\bar{n} \times (\bar{H}_2 - \bar{H}_1) = \bar{\alpha}_s \quad (2.4d)$$

where subscript 1 and 2 distinguish the different media near the interface, \bar{n} is the unit vector normal to the boundary interface, σ_s is the surface charge density, and $\bar{\alpha}_s$ is the surface (conduction) current density. For a monochromatic wave, the above four relations are not independent, from Equations (2.4b) and (2.4d), the other two can be derived. In our problem here, $\bar{\alpha} = 0$, the B.C. can be written as

$$\vec{E}_{1,\text{tan } gential} = \vec{E}_{2,\text{tan } gential} , \quad (2.5a)$$

$$\vec{H}_{1,\text{tan } gential} = \vec{H}_{2,\text{tan } gential} . \quad (2.5b)$$

Here, 1 and 2 denote dielectric (or air) and metal respectively.

Characteristics of the guiding mode in such a narrow slit is that it's a longitudinal TM plasmon mode. Since the metal has a complex dielectric function, the propagation constants of the guiding mode will therefore be complex. There is no pure propagating or evanescent mode, even in the transverse direction. But for metals like silver, $\varepsilon(\omega) = \varepsilon' + i\varepsilon''$, $|\varepsilon'| \gg |\varepsilon''|$; propagating component is dominant in longitudinal direction and evanescent component is dominant in transverse direction. All these characteristics for TM case will be shown in the following derivations and discussions. While details of the TE case will not be discussed here. For TE case, evanescent component is dominant in both (longitudinal and transverse) directions, and no guiding mode exists.

2.4.1 Field and Wave Solutions in the Slit

Assume an ideal slit with infinite length and width a is formed in a infinite broad thick metal slab with thickness h . As shown in Figure 2.8, a linearly polarized beam with vacuum wavelength λ_0 is normally incident onto the slit with its E-field perpendicular to the slit direction. In this way, TM-polarized wave is launched into the slit. And only non-zero (H_z ; E_x ,

E_y) components of the field are necessary to be considered. In this problem, $a \ll \lambda$ (wavelength inside slit). In this derivation, we also assume the slab thickness, h , is large enough so that scattering at entrance and exit of the slit do not affect inside field and wave distribution. Then spatial distribution of the wave, $\tilde{\psi}(\vec{r}, t) = \psi(\vec{r}) \cdot e^{-i\omega t}$, inside the slit can be described by the time-independent monochromatic wave equation

$$(\nabla^2 + k_j^2)\vec{B}^{(j)}(\vec{r}) = 0 \quad (2.6)$$

combined with boundary conditions Equation (2.5), $E_y^{(1)}|_{interface} = E_y^{(2)}|_{interface}$ and $H_z^{(1)}|_{interface} = H_z^{(2)}|_{interface}$. Here $k_j^2 = \mu_j \varepsilon_j (\mu_0 \varepsilon_0) \omega^2$, $j = 0, 1, 2$ distinguishes vacuum, dielectric and metal involved; μ_j and ε_j denote relative permeability and permittivity (or dielectric constant). Assume $\mu_j = 1$ for the nonmagnetic materials. Then the wave equation can be written as

$$(\nabla^2 + k_j^2)\vec{H}^{(j)}(\vec{r}) = 0. \quad (2.7)$$

Let $\vec{H}^{(j)}(\vec{r}) = H_z^{(j)}(x, y)\hat{e}_z = X^{(j)}(x)Y^{(j)}(y)\hat{e}_z$, the Equation (2.7) can be split into

$$\frac{d^2 X^{(j)}}{dx^2} + k_{j,x}^2 X^{(j)} = 0, \quad (2.8)$$

$$\frac{d^2 Y^{(j)}}{dy^2} + k_{j,y}^2 Y^{(j)} = 0, \quad (2.9)$$

with

$$k_{j,x}^2 + k_{j,y}^2 = k_j^2 = \varepsilon_j \varepsilon_0 \mu_0 \omega^2, \quad j = 1(\text{dielectric}), 2(\text{metal}). \quad (2.10)$$

Here, $k_{j,z} = 0$ for the normal incidence on media with homogeneity in z-direction. Then the equations have solutions with the following forms:

$$X^{(j)} = A_j e^{ik_{j,x}x} + B_j e^{-ik_{j,x}x}, \quad (2.11a)$$

$$Y^{(j)} = C_j e^{ik_{j,y}y} + D_j e^{-ik_{j,y}y}. \quad (2.11b)$$

To specify the solutions, the following conditions, (C.1) ~ (C.5), need to be considered:

(C.1) As assumed, the metal slab is thick enough to neglect the scattering at slit entrance and exit, i.e. there is only dominant wave propagation in forward +y-direction. Thus, we can let

$$D_j \rightarrow 0 \quad (2.12)$$

with choice of $Re(k_{j,y}) \geq 0$. We only keep the item of $Y^{(j)}$ with positive wave vector. And it will also be shown later that $Im(k_{j,y}) \geq 0$, which implies wave attenuation in forward +y-direction. High order reflection for long slit should be negligible.

(C.2) $H_z^{(1)} \Big|_{x=0,a} = H_z^{(2)} \Big|_{x=0,a}$. From the B.C., we can get $k_{1,y} = k_{2,y}$. Let

$$k_{1,y} = k_{2,y} = \beta . \quad (2.13)$$

Usually, β is complex, $\beta = \beta' + i\beta''$. Here we didn't consider the magnitude relations, which will be counted later.

(C.3) $H_z^{(2)} \Big|_{x \rightarrow \pm\infty} = 0$. In other words, the field deep inside metal is zero, or the field is attenuating in the direction of depth. Let's define

$$k_{1,x} = i\gamma_1, \quad \text{and} \quad k_{2,x} = i\gamma_2 . \quad (2.14)$$

Usually $\gamma_i = \gamma_i' + i\gamma_i''$ is also complex. Then the $X^{(2)}$ component of the H-field inside metal becomes

$$X^{(2)} = B_2 e^{\gamma_2 x}, \quad (x \leq 0) \quad (2.15a)$$

$$X^{(2)} = A_2 e^{-\gamma_2 x}, \quad (x \geq a) \quad (2.15b)$$

It is noted that Equations (2.15a) and (2.15b) are just choice of an attenuating item for each regime. Depending on the sign of $\text{Re}(\gamma_2)$ from definition, they are exchangeable. Here, physically it implies $\text{Re}(\gamma_2) > 0$. But for either choice, it will be unified by the resulted different relations between A_2 and B_2 .

(C.4) Symmetry. Due to the symmetry of the structure in x-direction, the field at two sidewalls will be either symmetric or anti-symmetric. I.e.

$$H_z^{(1)} \Big|_{x=0} = H_z^{(1)} \Big|_{x=a}, \quad \text{or} \quad (2.16a)$$

$$H_z^{(1)} \Big|_{x=0} = -H_z^{(1)} \Big|_{x=a}. \quad (2.16b)$$

In the case of $H_z^{(1)} \Big|_{x=0} = H_z^{(1)} \Big|_{x=a}$, we have

$$A_1 + B_1 = A_1 e^{ik_{1,x} \cdot a} + B_1 e^{-ik_{1,x} \cdot a}. \quad (2.17)$$

To satisfy it, either

$$k_{1,x} \cdot a = 2m \cdot \pi, \quad m = 1, 2, \dots, \text{ with } \text{Im}(k_{1,x}) \approx 0, \quad (2.18)$$

or, with $\text{Im}(k_{1,x}) \neq 0$,

$$B_1 = A_1 e^{ik_{1,x} \cdot a}. \quad (2.19)$$

In the case of $H_z^{(1)} \Big|_{x=0} = -H_z^{(1)} \Big|_{x=a}$, similarly we have

$$A_1 + B_1 = -A_1 e^{ik_{1,x} \cdot a} - B_1 e^{-ik_{1,x} \cdot a}. \quad (2.20)$$

And

$$k_{1,x} \cdot a = (2m + 1) \cdot \pi, \quad m = 0, 1, 2, \dots, \text{ with } \text{Im}(k_{1,x}) \approx 0, \quad (2.21)$$

$$B_1 = -A_1 e^{ik_{1,x} \cdot a}, \text{ with } \text{Im}(k_{1,x}) \neq 0 \quad (2.22)$$

It's obvious that Equations (2.18) and (2.21) are solutions of conventional dielectric-core metallic waveguide, $k_{\text{transverse}} \cdot a = n\pi, (n = 1, 2, \dots)$. As in our present problem, $a \ll \lambda$ and $|k_{1,x}| < |k_1|$, it's impossible for satisfaction of Equations (2.18) and (2.21), which are pure propagation wave solutions. Thus we take Equations (2.19) and (2.22).

By applying the symmetry relations on the field items inside metals, we can also get

$$A_2 = B_2 e^{\gamma_2 a}, \quad (\text{symmetric case}) \quad (2.23a)$$

$$A_2 = -B_2 e^{\gamma_2 a} \quad (\text{anti-symmetric case}) \quad (2.23b)$$

for Equations (2.15a) and (2.15b).

For convenience of further analysis, let's do an intermediate organizing of the solutions by substituting Equations (2.12), (2.13), (2.14), (2.15), (2.19), (2.22) and (2.23) into Equation (2.11) and making $H_0^{(1)} = A_1 C_1$ and $H_0^{(2)} = B_2 C_2$. The solution becomes

Inside slit (ε_1):

$$H_z^{(1)} = H_0^{(1)} \left[e^{-\gamma_1 x} \pm e^{-\gamma_1(a-x)} \right] \cdot e^{i\beta y} \quad (0 \leq x \leq a) \quad (2.24)$$

Inside metal (ε_2):

$$H_z^{(2)} = H_0^{(2)} e^{\gamma_2 x} \cdot e^{i\beta y} \quad (x \leq 0) \quad (2.25a)$$

$$H_z^{(2)} = \pm H_0^{(2)} e^{\gamma_2(a-x)} \cdot e^{i\beta y} \quad (x \geq a) \quad (2.25b)$$

Here, “+” and “-” of “ \pm ” correspond to the symmetric and anti-symmetric cases respectively.

Further, apply the B.C., $H_z^{(1)} \Big|_{x=0,a} = H_z^{(2)} \Big|_{x=0,a}$, again on the solution, we can get the relation between $H_0^{(1)}$ and $H_0^{(2)}$:

$$H_0^{(2)} = H_0^{(1)} \left(1 \pm e^{-\gamma_1 a} \right) \quad (2.26)$$

Again, “+” and “-” represent for symmetric and anti-symmetric case respectively.

$$(C.5) \quad E_y^{(1)} \Big|_{x=0,a} = E_y^{(2)} \Big|_{x=0,a}.$$

From the Maxwell's equation, $\frac{\partial D_y}{\partial t} = -\frac{\partial H_z}{\partial x}$, and the constitution relations, $E_y^{(j)}$ can be

obtained by substituting $H_z^{(j)}$ into

$$E_y^{(j)} = \frac{1}{\varepsilon_j(i\omega)} \frac{\partial H_z^{(j)}}{\partial x}. \quad (2.27)$$

Specifically,

in symmetry:

$$E_y^{(1)} = \frac{-\gamma_1}{\varepsilon_1(j\omega)} \left[e^{-\gamma_1 x} - e^{-\gamma_1(a-x)} \right] H_0^{(1)} \cdot e^{i\beta y} \quad (0 \leq x \leq a) \quad (2.28)$$

$$E_y^{(2)} = \frac{\gamma_2}{\varepsilon_2(j\omega)} e^{\gamma_2 x} H_0^{(2)} \cdot e^{i\beta y} \quad (x \leq 0) \quad (2.29a)$$

$$E_y^{(2)} = -\frac{\gamma_2}{\varepsilon_2(j\omega)} H_0^{(2)} e^{\gamma_2(a-x)} \cdot e^{i\beta y}; \quad (x \geq a) \quad (2.29b)$$

in anti-symmetry:

$$E_y^{(1)} = \frac{-\gamma_1}{\varepsilon_1(j\omega)} \left[e^{-\gamma_1 x} + e^{-\gamma_1(a-x)} \right] H_0^{(1)} \cdot e^{i\beta y} \quad (0 \leq x \leq a) \quad (2.30)$$

$$E_y^{(2)} = \frac{\gamma_2}{\varepsilon_2(j\omega)} e^{\gamma_2 x} H_0^{(2)} \cdot e^{i\beta y} \quad (x \leq 0) \quad (2.31a)$$

$$E_y^{(2)} = \frac{\gamma_2}{\varepsilon_2(j\omega)} H_0^{(2)} e^{\gamma_2(a-x)} \cdot e^{i\beta y}; \quad (x \geq a) \quad (2.31b)$$

Now applying the B.C., $E_y^{(1)} \Big|_{x=0,a} = E_y^{(2)} \Big|_{x=0,a}$, we get, for the symmetry case,

$$-\frac{\gamma_1}{\varepsilon_1} (1 - e^{-\gamma_1 a}) H_0^{(1)} = \frac{\gamma_2}{\varepsilon_2} H_0^{(2)}. \quad (2.32)$$

Substituting Equation (2.26) into Equation (2.32), the following relation is obtained:

$$\frac{\gamma_2}{\varepsilon_2} + \frac{1 - e^{-\gamma_1 a}}{1 + e^{-\gamma_1 a}} \cdot \frac{\gamma_1}{\varepsilon_1} = 0. \quad (\text{symmetric case}) \quad (2.33)$$

Similarly it can also be obtained for anti-symmetry case that

$$\frac{\gamma_2}{\varepsilon_2} + \frac{1 + e^{-\gamma_1 a}}{1 - e^{-\gamma_1 a}} \cdot \frac{\gamma_1}{\varepsilon_1} = 0. \quad (\text{anti-symmetric case}) \quad (2.34)$$

By defining

$$f_{\pm}(\gamma_1 a) = \left(\frac{1 - e^{-\gamma_1 a}}{1 + e^{-\gamma_1 a}} \right)^{\pm 1}, \quad (2.35)$$

Equations (2.33) and (2.34) can be expressed together with

$$\frac{\gamma_2}{\varepsilon_2} + f_{\pm}(\gamma_1 a) \cdot \frac{\gamma_1}{\varepsilon_1} = 0. \quad (2.36)$$

Where “+” and “-” correspond to symmetry and anti-symmetry case. It is seen that Equation (2.36) has the same form as Equation (1.12), which is the determinant relation for surface plasmons [7], when $f_{\pm}(\gamma_1 a) = 1$ for $a \rightarrow \infty$. Thus, we can consider $f_{\pm}(\gamma_1 a)$ as a factor of surface plasmon coupling between the two slit walls.

By the way, the E_x -field distribution can be also obtained from the derivation of Maxwell's equations

$$E_x^{(j)} = -\frac{\beta}{\varepsilon_j \omega} \cdot H_z^{(j)}. \quad (2.37)$$

In the following subsections, further discussions, extensions and models are developed for understanding more features of the guiding wave inside the narrow metallic slit.

2.4.2 Propagation Constants and Effective Index

With Equations (2.10) and (2.36), the wave propagation constant β can be obtained by substituting

$$\gamma_j = \sqrt{\beta^2 - \varepsilon_j k_0^2}, \quad (k_0 = \frac{2\pi}{\lambda_0} \text{ is the wave vector in free space}) \quad (2.38)$$

into

$$\frac{\gamma_2}{\varepsilon_2} + \left(\frac{1 - e^{-\gamma_1 a}}{1 + e^{-\gamma_1 a}} \right)^{\pm 1} \cdot \frac{\gamma_1}{\varepsilon_1} = 0. \quad (2.39)$$

But analytically, it's very difficult to solve such a transcendental equation. It is also obvious that $\beta (= \beta' + i\beta'')$ is dependent on both the dielectric constants, $\varepsilon_j(\omega)$, and the slit width, a . Assume the slit is filled with air, i.e. $\varepsilon_1 = 1$, and the metal is silver, whose dielectric constants are taken from 6-th order polynomial fitting of the experimental data (from ref. [6]) in the wavelength

range of 400 ~ 1800 nm. Numerically, the dependence of β'/k_0 and β''/k_0 on wavelength and slit width, a , are calculated and shown in Figure 2.9 and Figure 2.10. In Figure 2.11, a parametric plot of the propagation constant β with wavelength as parameter is shown at fixed slit width. Figure 2.12 shows parametric plots of the transverse wave vectors inside slit (γ_1) and silver skin depth (γ_2) with slit width as parameter at a fixed wavelength. Figure 2.13 shows a typical distribution of wave intensity along the transverse direction. From these plots, we can see:

- (1) In the longitudinal direction of the slit, $|\text{Re}(\beta)| \gg |\text{Im}(\beta)|$, the wave is propagation dominant. Let's define

$$N(\omega, a) = \beta/k_0$$

as the effective index inside the slit, and we can see that it is a function of both the incidence light wavelength and the slit width. The propagation phase velocity, mainly determined by $\text{Re}(\beta)$, is less dependent on wavelength but more on slit width; while the attenuation, mainly determined by $\text{Im}(\beta)$, becomes prominent especially at short wavelengths and/or small slit width. We can also see that, $|\beta| > |\beta_0|$, where

$$\beta_0 = k_0 \sqrt{\frac{\epsilon_1 \epsilon_2}{\epsilon_1 + \epsilon_2}}, \quad (2.40)$$

similar with Equation (1.14), which can be considered as the propagation constant of “free” surface plasmon wave. It implies that the plasmon wave propagation inside the slit is “slower” (in phase velocity) than the “free” surface plasmon wave propagating at same media interface because of more retardation induced by SP coupling of the two slit walls. Such retardation will result in additional energy dissipation.

(2) In the transverse direction of the slit, $|Re(\gamma_j)| \gg |Im(\gamma_j)|$, the wave is strongly attenuating especially in the metal skin depth. For such a negligible transverse propagation component, we consider the TM fundamental transmission mode inside the narrow slit is a plasmon mode. We can also consider there is no phase accumulation in transverse direction, but just phase shift at dielectric/metal interface.

For the anti-symmetric case, numerical solutions were not readily found in the parameter range of our interest shown above. We suspect the mathematical solution do not mean a valid physical process in this parameter range. Additionally, from Equation (2.24), we can see that such an anti-symmetry mode is suppressed in magnitude because of destructive coupling, and not favorable for power transmission; while the symmetric mode is an enhanced mode for transmission.

2.4.3 Dipole Modeling of Symmetric Plasmon Mode inside Slit

From the previous analysis, we can see the following relations for the symmetric mode:

$$H_z \Big|_{x=0} = H_z \Big|_{x=a}, \quad (2.41a)$$

$$E_x \Big|_{x=0} = E_x \Big|_{x=a}, \quad (2.41b)$$

$$E_y \Big|_{x=0} = -E_y \Big|_{x=a}; \quad (2.41c)$$

They are exactly the field nature of a dipole infinite in z-direction, as shown in Figure 2.14. Thus we can simulate the propagating surface plasmon mode inside the slit as a dipole wave. Charges in the dipole are the collective electron distribution formed at opposite slit walls. For phase matching, the transverse dipole oscillation has the same frequency as that of the longitudinal surface plasmon wave frequency, i.e. the incidence light frequency. Again, it is noted that this is different from the conventional positioned oscillation dipole; it's a dipole plasmon wave that propagates along the slit. Propagation properties of such a dipole wave are characterized by the excitation frequency and the environment (material and geometry) that the excitons are “parasitic” in.

Previously, we assumed that the metal slab is thick enough so that we neglected the longitudinal boundaries, which resulted in “free” y-direction propagation. Actually, as the slab thickness becomes much larger than the skin depth and smaller than the plasmon wavelength, the field distribution along y-direction also becomes a fundamental mode. If the impedances at slit entrance and exit are small, such a mode is weakly confined, which favors the light launching at

entrance and emitting at exit. Then the high order resonance along the slit is negligible. Thus our assumption, $D_j \rightarrow 0$, in Equation (2.12) is meaningful not only for very long slits, but also for short slits (shorter than wavelength). Prominent resonance along the slit should be considered as it is within length of a few wavelengths. And for the thin metal slabs, the plasmon mode is so confined in the slit region that we can even consider it as a positioned oscillation dipole. The incident light launches power to the dipole, and it emits as a secondary field source.

2.4.4 Funneling of Light into Metallic Narrow Slit

We have shown that an optical wave propagates as a plasmon mode inside a narrow slit ($a \ll \lambda$). The incident beam couples into a plasmon mode, and this coupling occurs at the entrance of a slit. The sharp (or curved) edge of the entrance itself can work as a coupler for excitation of surface plasmon. The mechanism is that the edge-coupler introduces momentum enhancement/retardation as explained in Section 1.3. The process can also be understood as a scattering problem at a more fundamental level. The heterogeneous distribution of the media near the slit scatters incident TM-polarized light. As a result, scattered light strongly localized around edges, and metal surface electrons are excited by absorption, which oscillate harmonically with surface EM waves. The collective electron oscillation waves readily propagate along the metal surface and thus “funnel” the associated energy into the slit. Note, again, that the EM wave inside slit is also an exhibition of the electron oscillation. In the analytical scattering problem point of view, the narrow slit acts as a complementary small scattering object, and the enlarged scattering cross-section effectively collects more power than that directly impinges onto

the slit area. For not well-defined boundaries, such a scattering problem is also not easy to solve analytically. Using FDTD numerical simulation, the Poynting vector ($\vec{S} = \vec{E} \times \vec{H}$) is calculated and shown in Figure 2.15 at instant phase intervals. In simulation, the slit width is 80 nm, and the vacuum wavelength is 650 nm. The funneling process is a dynamic process. At the instant that near maximum power flows into the slit [$5\pi/6$ instant of Figure 2.15], the instant funneling cross-section of the slit, defined as

$$C_f = \frac{W_f}{I_i} \quad (2.42)$$

in unit of length in z-direction, is estimated from the graph to be around 300 nm. Here, I_i is the incidence irradiance; W_f is the power rate that is funneled into the slit. Then we can get a funneling coefficient

$$Q_f = \frac{I_f}{I_i} = \frac{C_f}{C_{slit}} \quad (2.43)$$

of around 3.8. Here, I_f is the irradiance of power funneled into the slit, C_{slit} is the cross-section area of the slit in unit length in z-direction. Since the incidence field amplitude in the simulation is 1, from Figure 2.15, we see a \vec{S} magnitude of ~ 3.6 , which is consistent with the instant funneling coefficient.

Mathematically, if we introduce the complex form of the incidence source instead of its sinusoidal form in the simulation, we can obtain both amplitude and phase information of field distribution after certain time steps of calculation. Thereafter, the time-averaged intensity distribution is to be calculated. Such a “detectable” intensity distribution is shown in Figure 2.16(a) at the wavelength of 650 nm, where we assumed the monochromatic plane wave is normally incident onto a slit in a semi-infinite metal. As the incidence light (from bottom) interacts with the metal surface and the slit, most of the power will be reflected back and scattered by the slit entrance, which, superposing with the incidence beam, forms complex standing waves as shown in Figure 2.16(a). Otherwise, time-averaged intensity of the incidence beam would be uniform. Additionally, if the slit in metal is ideally semi-infinite, the integral wave intensity inside it will also be uniform (neglecting absorption in a short propagating range) or monotonically attenuating along the propagating direction, i.e. there will be no standing waves formed inside the slit. But in real situation of the simulation, the boundary “perfect matching layer (PML)” is not perfectly absorbing. Therefore, a weak resonant standing wave mode is formed along the channel, more clearly shown with a cross-section view along the mid-line of the slit in Figure 2.16(b). Effectively, we can spatially average the intensity along the slit channel to consider as that of the ideal case. At the wavelength of 650 nm, this value is ~ 1.8 . Notice that the incidence beam amplitude is 1, and the time averaging will result in a factor of 0.5 for both the incidence intensity and as-resulted intensity inside slit. The average intensity inside slit is equivalent to the normalized funneling coefficient. Here particularly at the wavelength of 650 nm, the averaged effective funneling coefficient (~ 1.8) is half of that at the instant with maximum funneling as shown above, which is exactly due to the averaging factor of 0.5 for power integration of a sinusoidal signal. We perform this processing for different slit widths in the

wavelength range of 450 ~ 1000 nm and obtain the plots shown in Figure 2.17. In this figure, Figure (a) shows the dependence of funneling coefficient on wavelength for slits with different slit width; Figure (b) shows the dependence of funneling coefficient on slit width at different wavelengths; and Figure (c) shows the dependence of power funneled into the slit on slit width at different wavelengths, where the normalized power is defined as the multiplication of funneling coefficient, slit width and incidence intensity ($= 1$).

An inspection of Figure 2.17 (a), (b) and (c) comes to the following conclusions: (1) Dependence of funneling coefficient on slit width and wavelength are not monotonous in the shown data range; there are critical points for wavelength at 600 nm and slit width at 40 nm. (2) Overall, the funneling coefficient decreases with increase of wavelength below 600 nm wavelength and increases with increase of wavelength above 600 nm wavelength; but as the wavelength further increases to be above 850 nm, it again decreases. (3) Below the wavelength of 600 nm, the funneling coefficient monotonically decreases with increase of slit width over the full range (20 ~ 180 nm); above the wavelength of 600 nm, a maximum appears at 40 nm slit width; the funneling coefficient drops at slit widths smaller than 40 nm. At the point, reasoning of the critical points, 600-nm-wavelength and 40-nm-slit-width, is still obscure. As we count the power that is funneled into the slit, the trends are quite clear. It lead to conclusions: (4) at a particular wavelength, the funneled power monotonically increases with increase of the slit width; (5) the funneled powers are more differentiated for different wavelengths as the slit width becomes larger; and they becomes low and very close at the slit width of 20 nm. The small fluctuations in plot (a) may be due to resonance resulted from limited finite problem region and non-ideal absorbing boundary conditions in simulation.

We briefly discussed the longitudinal resonance effects along the slit in a finite thick metal slab in Section 2.4.3, here we simulated the case with time averaged intensity distribution for different metal thicknesses, which are shown in Figure 2.18 (a) 2000-nm-thick, (b) 200-nm-thick and (c) 100-nm-thick. In this simulation, the slit width is chosen as 80 nm and the incidence wavelength is 650 nm. It clearly shows that a standing wave mode is formed inside the slit for (a) with seven maximum nodes and (b) with only one maximum node; while for (c), if it is too thin, there cannot be confined mode. As part of the energy transmitted through the slit, it evolves into spherical waveforms and the slit exits act as a cylindrical point source. Interestingly, it is found that the intensity of the output for thicker slit shows a larger magnitude than that for thinner ones. Although the absorption of energy by slit walls are neglected in this simulation, it's speculated that the effects are mainly due to the longitudinal resonance in slit.

Additionally, it is noticed that edge excited surface plasmons also propagate away from the slit in the metal plane ($y = 0$ plane) in both directions perpendicular to the slit. Due to attenuation, the SP wave will gradually die out. But if there are many slits (or corrugations) that are periodic and are able to excite SPs coherently, the locally excited SPs will be coupled with each other and can propagate to a far distance as it extends. The slit arrays then work as a SP coupler. The coupling would also follow the phase matching conditions, Equation (1.21). Such SP waves have resonance properties of standing waves. And usually there exists a bandgap distribution of the SP wave modes, which will be shown in next section.

In the case of slit arrays with period smaller than the lateral funneling length, the funneling cross-section will be approximately the area of one period due to the identity of the slits. In this way, without negative role of other physical effects, the transmission for TM-polarized light would approach up to 100 % with a small portion of absorption loss. Such a condition is nearly fulfilled at the main peak of our transmission spectrum (Figures 2.5 and 2.6).

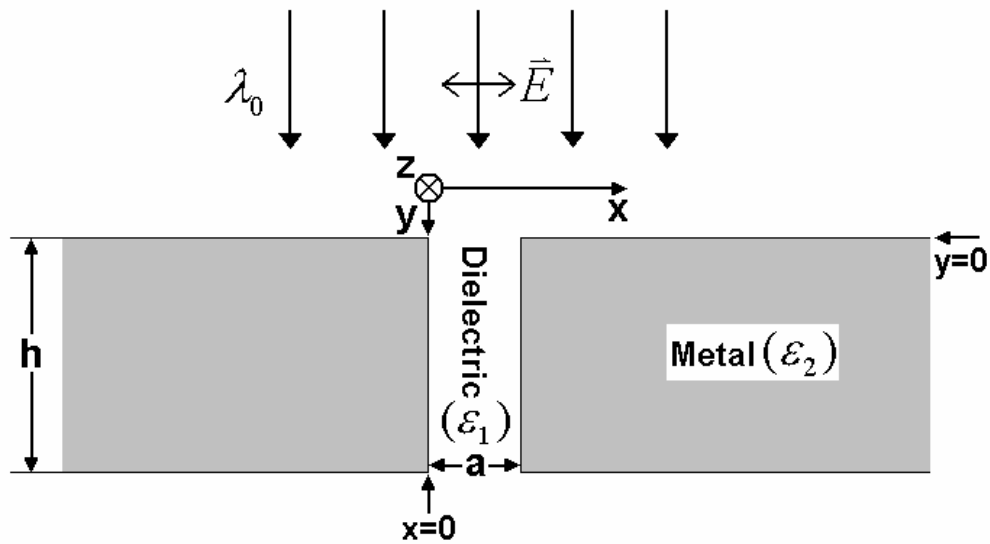
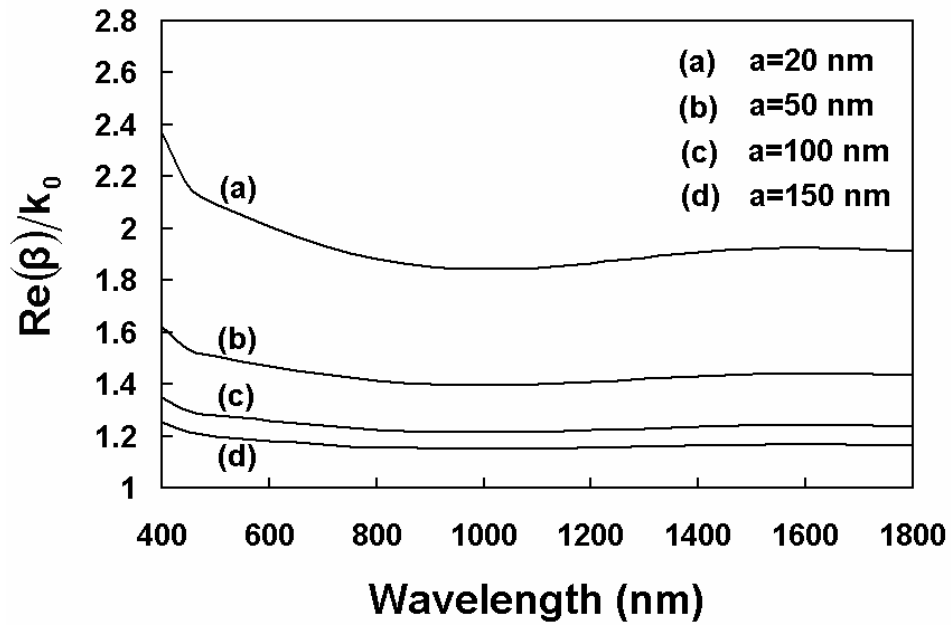
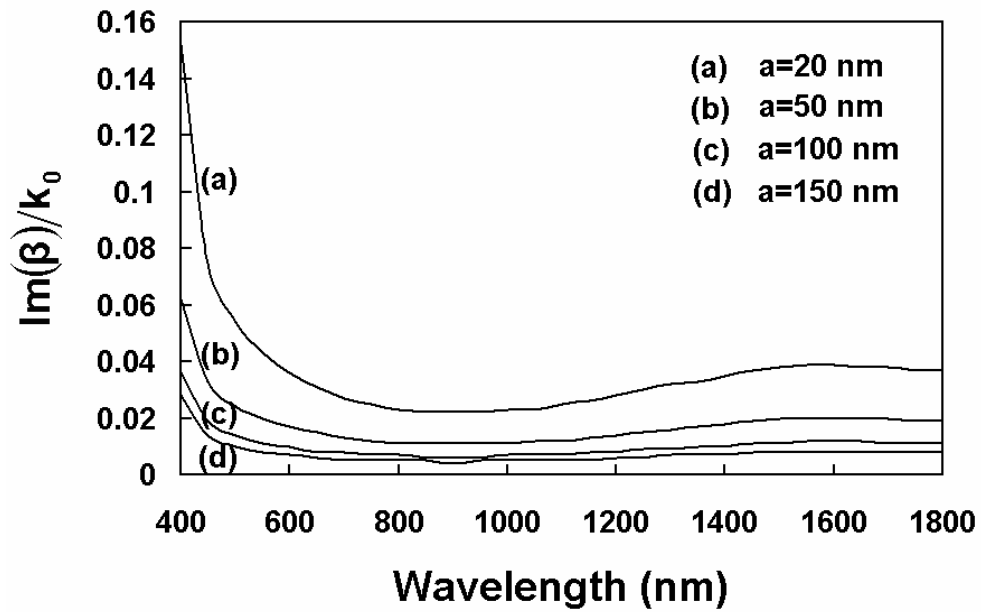


Figure 2.8. Illustration of TM-polarized light normal incidence on a broad thick metal slab with a narrow slit. The as-shown right-hand Cartesian coordination is defined for analysis.

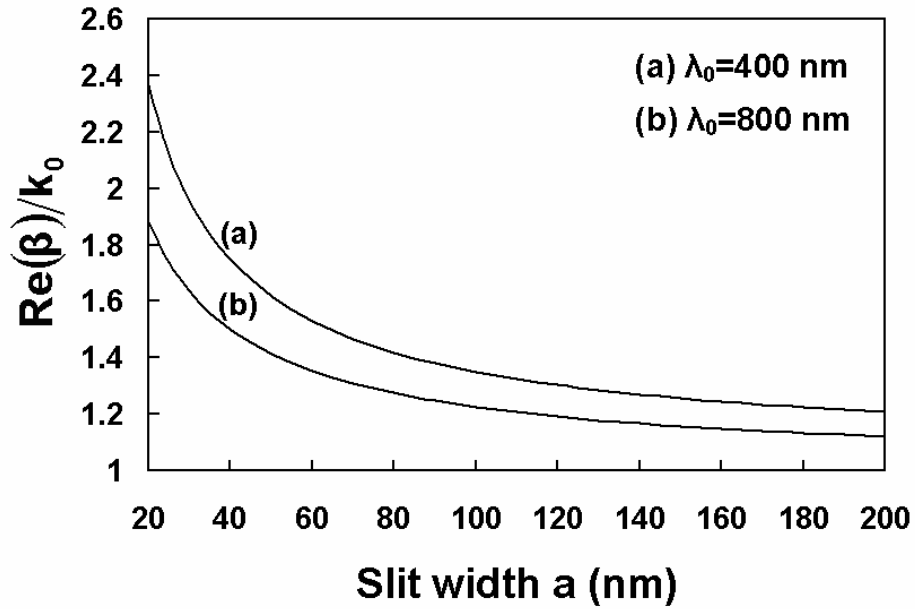


(a)

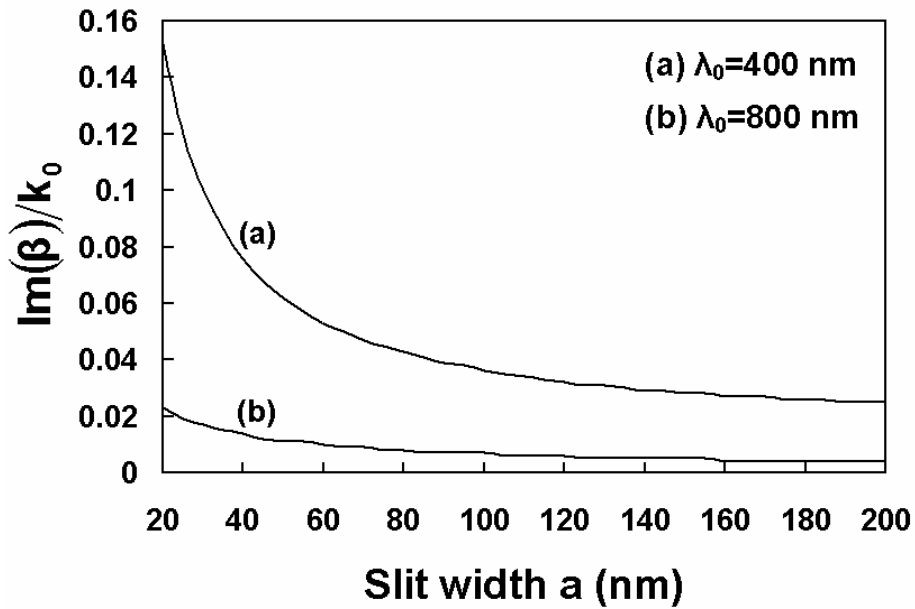


(b)

Figure 2.9. Dependence of real and imaginary part of the propagation constant β on wavelength with slit width as parameters.



(a)



(b)

Figure 2.10. Dependence of real and imaginary part of the propagation constant β on slit width with wavelength as parameters. As the wavelength is larger than 800 nm, the dependence curve is very close to that of 800 nm.

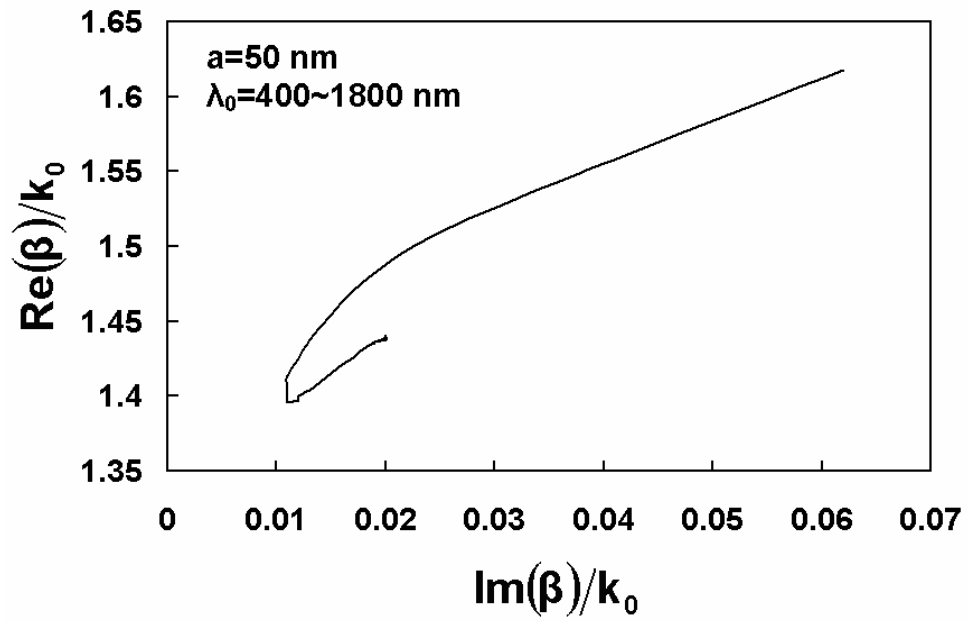
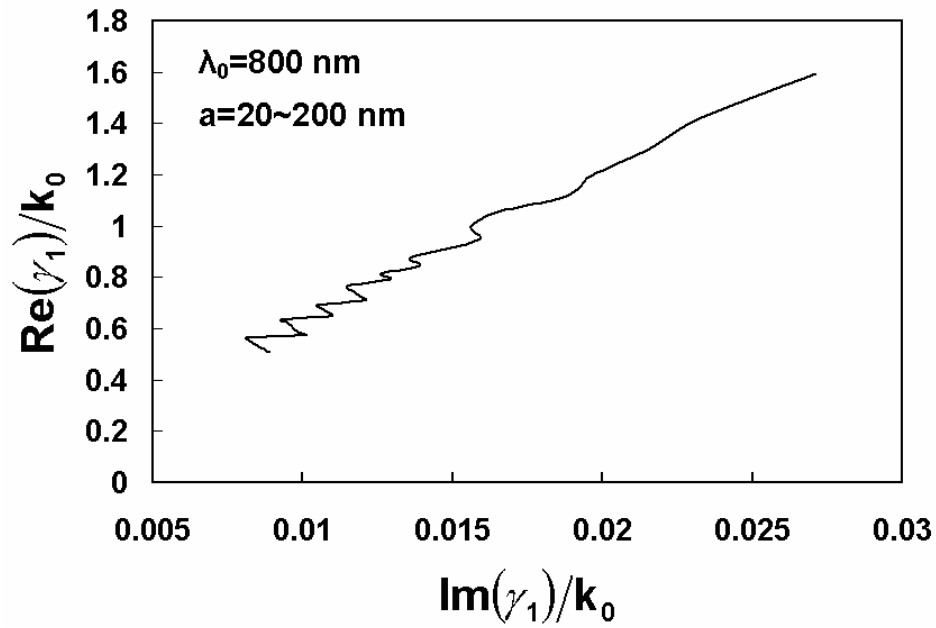
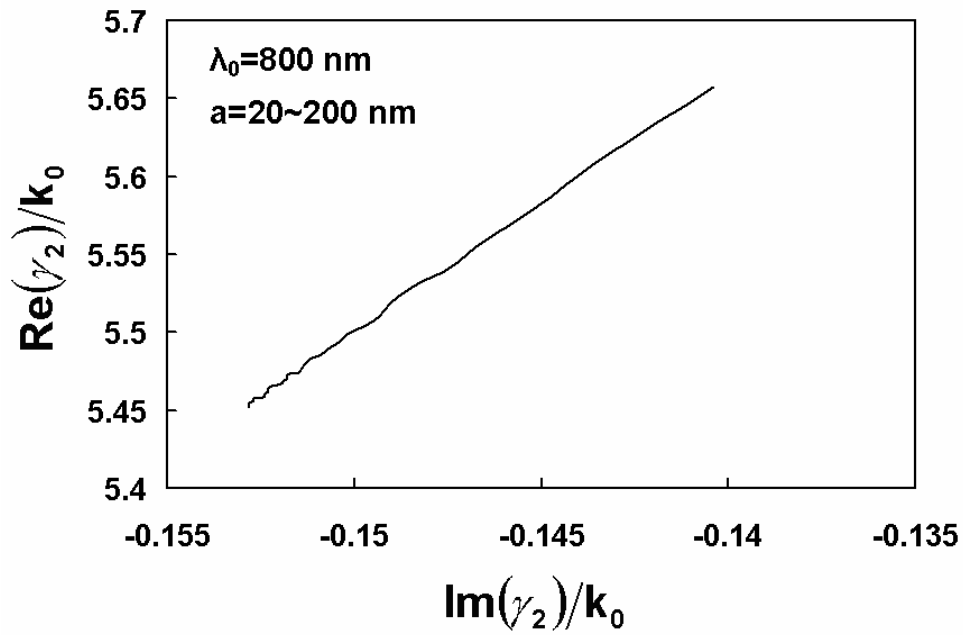


Figure 2.11. Parametric plot of the propagation constant β with wavelength as parameter at a fixed slit width of 50 nm.



(a)



(b)

Figure 2.12. Parametric plots of transverse wave vectors inside slit (γ_1) and silver skin depth (γ_2) with slit width as parameter for fixed wavelength of 800 nm.

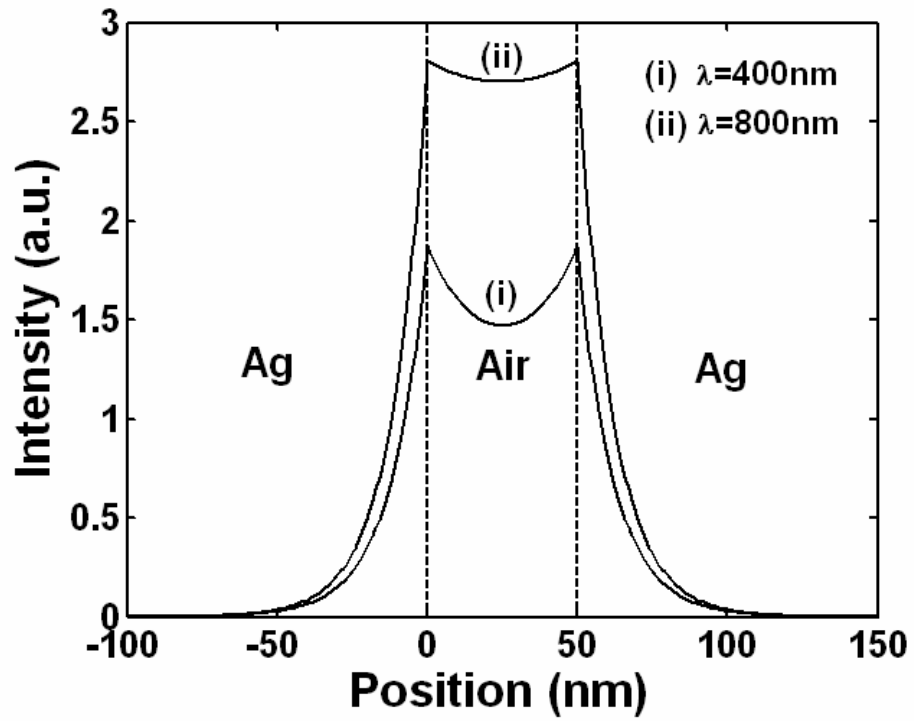
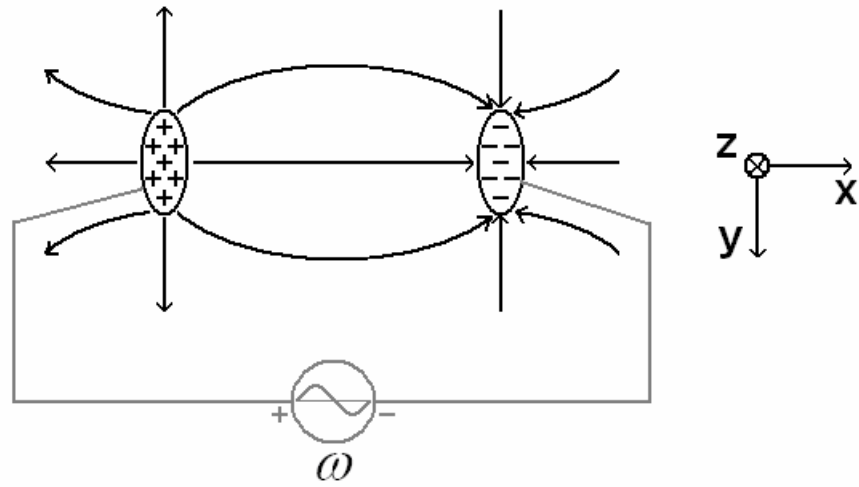
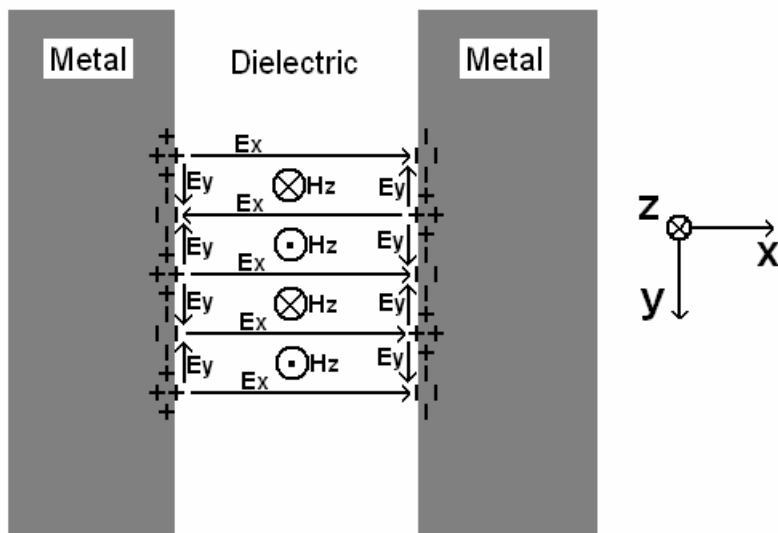


Figure 2.13. Intensity distribution along the transverse direction of the plasmon mode inside the narrow slit. The slit width is 50 nm.



(a)



(b)

Figure 2.14. A dipole wave model of the symmetry plasmon mode inside the narrow metallic slit. (a) shows a stationary analogy of the plasmon dipole transverse oscillation and the field distributions; (b) shows the alternating oscillation plasmon dipole wave propagating along the slit.

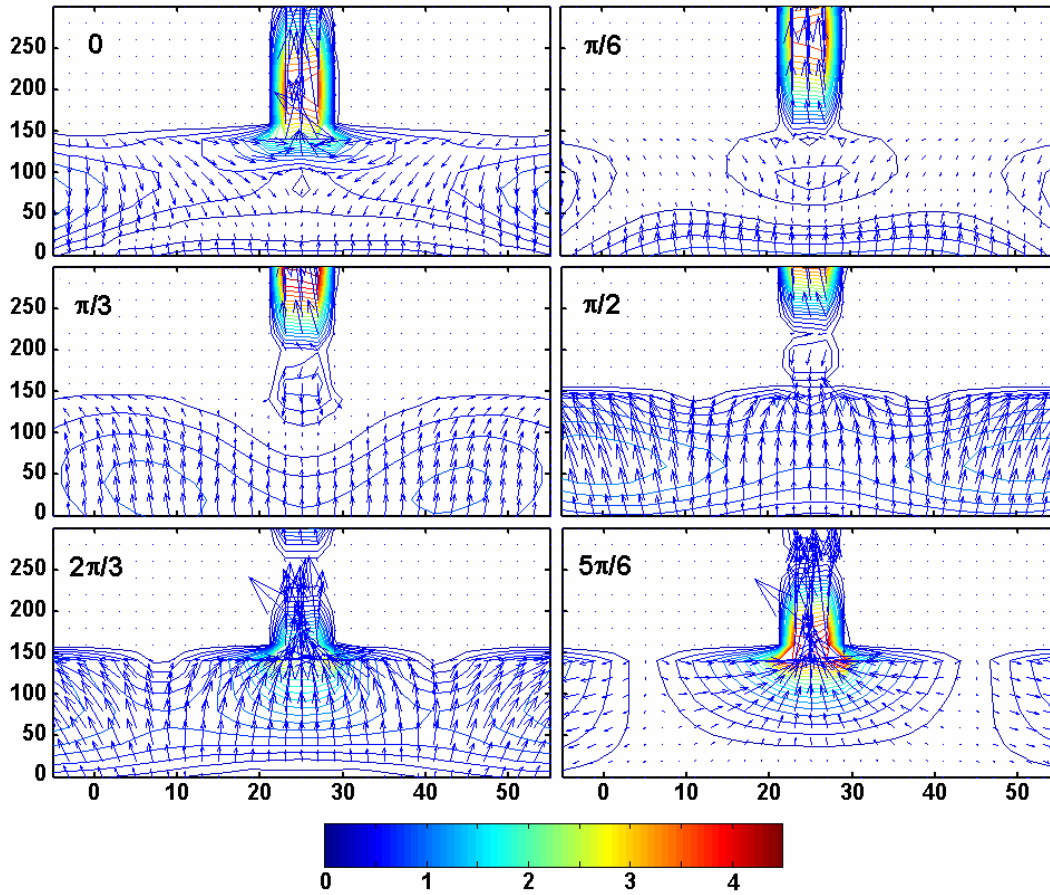


Figure 2.15. Funneling of optical energy into plasmon wave mode by slit entrance. The FDTD analysis shows instant power flow state at $\pi/6$ phase intervals. The color contour and arrows indicate magnitude and direction of the Poynting vector $\vec{S} = \vec{E} \times \vec{H}$. In simulation, the slit width is 80 nm, and the vacuum wavelength is 650 nm.

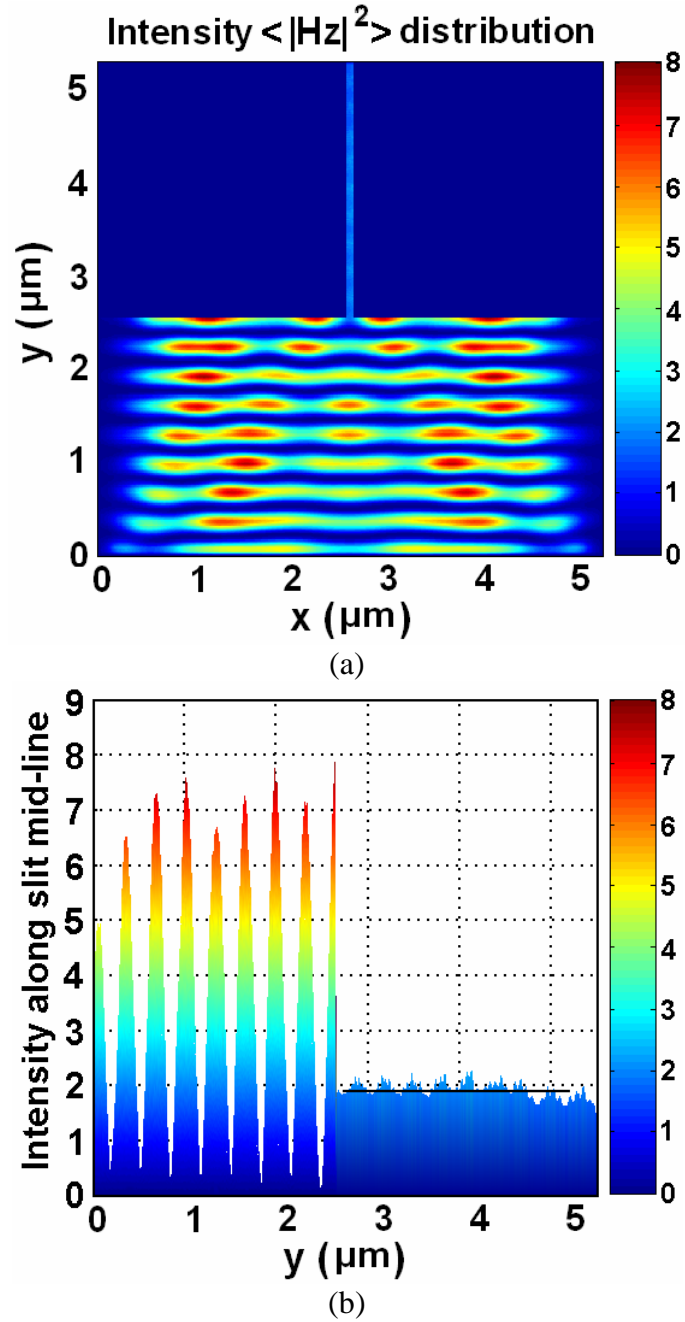


Figure 2.16. Time-averaged intensity distribution in funneling of light into a single slit. (a) Top view of the intensity distribution by FDTD analysis of a 80-nm-width slit at 650 nm wavelength incidence; (b) Cross-section view along the mid-line of the slit. The small fluctuations along the slit are due to imperfectness of the absorbing condition that introduces Fabry-Perot resonance inside, effects if which can be eliminated by spatial averaging as indicated in (b) with a flat line.

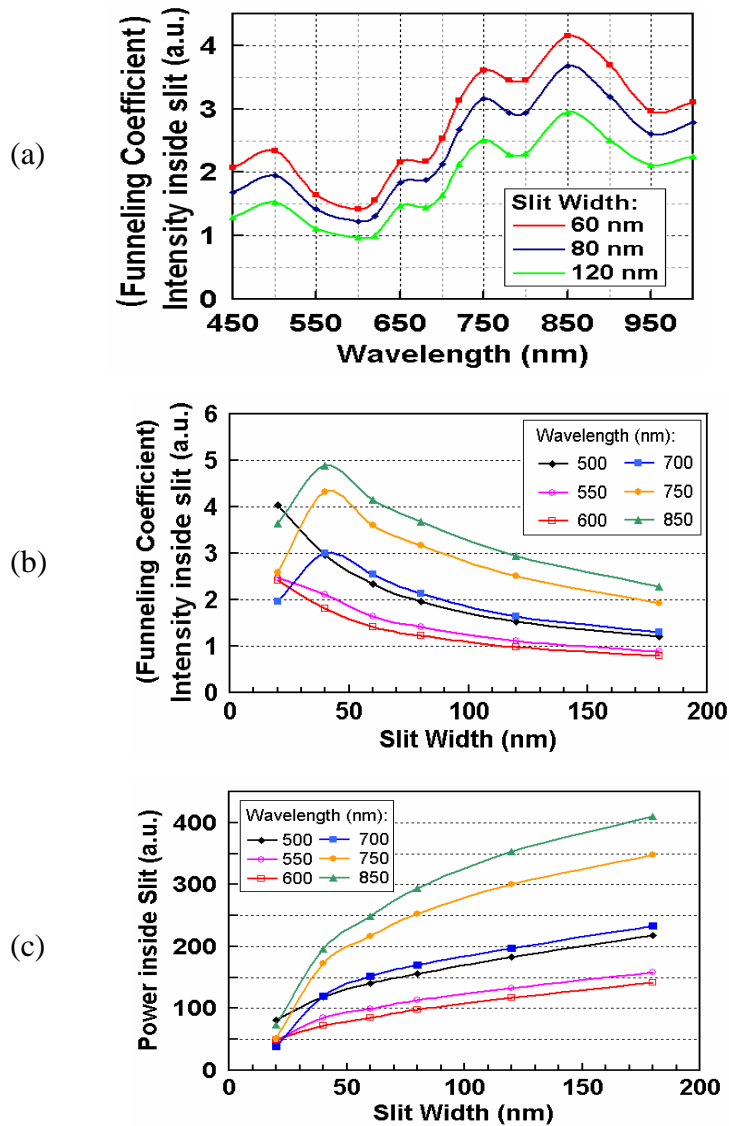


Figure 2.17. Dependence of funneling on slit width and incidence beam wavelength.

Since the incidence wave field amplitude is 1, the averaged intensity inside slit is equivalent to the normalized funneling coefficient. Thus (a) shows the dependence of funneling coefficient on wavelength for slits with different slit width; and (b) shows the dependence of funneling coefficient on slit width at different wavelengths. (c) shows the dependence of power funneled into the slit on slit width at different wavelengths. The normalized power is defined as the multiplication of funneling coefficient, slit width and incidence intensity (= 1).

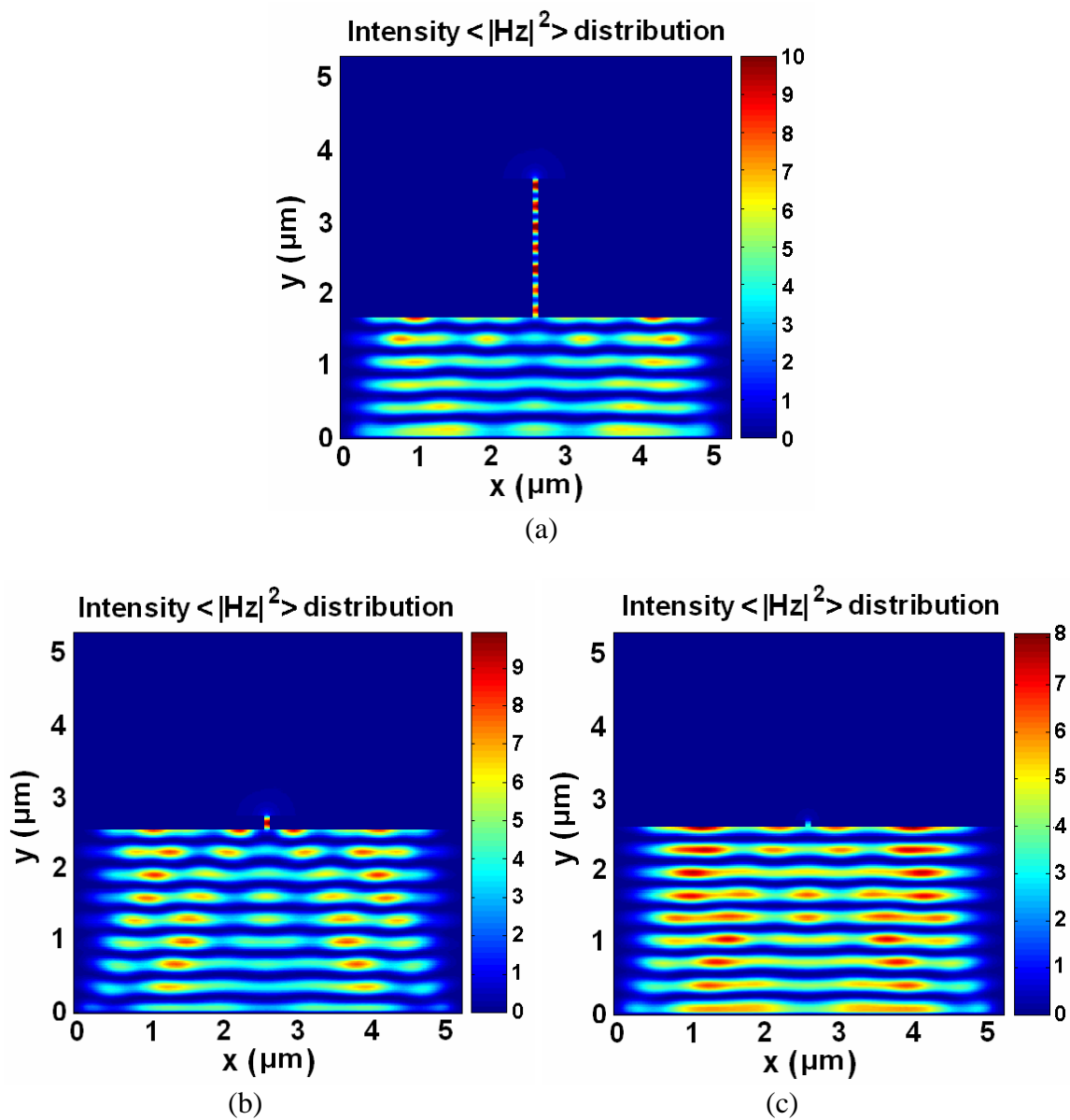


Figure 2.18. Time-averaged intensity distribution in light transmission through single slit in a metal layer of different thickness: (a) 2000-nm-thick; (b) 200-nm-thick; and (c) 100-nm-thick. In the simulation, the wavelengths are 650 nm, and the slit widths are all 80 nm. Dependent on the different thickness, different Fabry-Perot resonance modes are formed along the slit channel.

2.5 MODELING OF SURFACE PLASMON BAND STRUCTURES ON METALLIC GRATING SURFACE

Metallic reflection gratings with shallow periodic corrugations can be used for photon coupling into SP waves. Usually, the SP wave modes have bandgaps, i.e. SP waves within a certain range of frequency cannot be excited with the gratings. In other words, light with frequency in this range cannot be coupled into SP waves. The bandgap structures have been calculated by treating the reflection gratings as small perturbations on a smooth metal surface [34-36]. As a result, “minigaps” form at the centers and boundaries of Brillouin Zone (B.Z.) [36]. Such band gaps have also been observed in experiments [37-39].

For the problem, it would not be proper to treat the slit array structure as small perturbations. Here, we propose a model to calculate its band structures by extending the periodic interface into an infinite broad 1D multi-layer system, as schematically shown in Figure 2.19. In this model, we take into account the following considerations:

(1) The slit is very narrow ($a \ll \lambda$) so that there is a large impedance for plasmon funneling into the slit as the in-plane coherent SP waves are excited. This implies a strong near field coupling of SPs of two adjacent sections, and the fields “bridge” across the gap without strong scattering.

(2) There is no coupling between the SP modes at the top and bottom dielectric/metal interfaces through the narrow slits.

(3) The in-plane SP waves are effectively localized at the dielectric/metal interfaces such that there is no SP propagation wave vector component normal to the interfaces.

(4) Thus, we can extend the interface layer into an infinite broad multi-layer system. The SP waves are characterized by the frequency and the propagation media dielectric constants. At the layer extended from dielectric/metal interface, the effective dielectric constant is extracted from Equation (1.14) as

$$\varepsilon_{eff} = \frac{\varepsilon_d \cdot \varepsilon_m}{\varepsilon_d + \varepsilon_m} \quad (2.44)$$

where ε_d and ε_m are the dielectric constants of the two media that compose the interface. The dielectric constant for the layer of slit is that of the effective one composed by the slit media and outside dielectric. For the structure we formed shown in Figure 2.1, it is just taken as the air dielectric constant.

For calculation of energy band structure of a 1D periodic multi-layer structure, a transfer matrix method has been conveniently used in similar 1D material systems [40]. The dispersion relation was shown to be

$$\cos(k_{sp}d) = \cos(k_1a)\cos[k_2(d-a)] - \frac{1}{2}\left(\frac{k_1}{k_2} + \frac{k_2}{k_1}\right)\frac{\sin(k_1a)}{\sin[k_2(d-a)]}, \quad (2.45)$$

where d is the slit grating period, a is the slit width, and

$$k_1 = \sqrt{\varepsilon_1} \cdot k_0, \quad \text{and} \quad k_2 = \sqrt{\varepsilon_2} \cdot k_0 \quad \left(k_0 = \frac{2\pi}{\lambda_0} = \frac{\omega}{c_0} \right).$$

We also define a filling factor, $f = (d - a)/d$, as the metal portion of the period. For our demonstrated structures (Figure 2.1), taking

$$\varepsilon_1 = \varepsilon_{air} = 1, \quad \varepsilon_2 = \frac{\varepsilon_{air} \varepsilon_{Ag}(\omega)}{\varepsilon_{air} + \varepsilon_{Ag}(\omega)}$$

for the Air/Ag interface SP mode, and

$$\varepsilon_1 = \varepsilon_{air} = 1, \quad \varepsilon_2 = \frac{\varepsilon_{quartz} \varepsilon_{Ag}(\omega)}{\varepsilon_{quartz} + \varepsilon_{Ag}(\omega)} \quad (\text{Assume } \varepsilon_{quartz} = 2.16)$$

for the quartz/Ag interface SP mode, the band structures are calculated and shown in Figures 2.20 and 2.21 for varied periods (370 and 780 nm) and filling factors (0.6 and 0.8).

We should know that the dispersion relation (Equation 2.45) only describes the possible modes of in-plane surface plasmon waves that the periodic structure supports. It does not suggest how the surface plasmon waves are to be excited or coupled; it could be optically or electronically. Here, we are concerning the surface plasmon interaction of incidence light with the metallic nanostructures; the SP grating coupling condition is to be considered:

$$k_{sp} = k_x = \frac{2\pi}{d} \cdot m + k_0 \cdot \sin \theta \quad (2.46)$$

where d is the grating period, m is an integer indicating coupling order, $k_0 = \frac{2\pi}{\lambda_0} = \frac{\omega}{c}$, and θ is the beam incidence angle. In analysis, a combination of Equations (2.45) and (2.46) describes the characteristics of coupled in-plane surface plasmon waves; while they are independent with each other.

At normal incidence, $\theta = 0$, then $k_{sp} = \frac{2\pi}{d} \cdot m$. In the optical range and grating period that we are considering, the coupling order m could be +1 and -1 in the same configuration. The degenerate modes denote coupling of SP waves in opposite directions. Interference of the two modes forms resonant standing wave surface plasmons. Such modes become split (as indicated in Figures 2.20 and 2.21) at the center of the Brillouin Zone (B.Z.). This is similar to band splitting for Bragg scattering in photonic and electronic band structures, but here the interference beams are mainly due to direct couplings instead of reflections at boundaries.

For oblique incidence of light, the coupled surface plasmons are propagating waves; while scattering of SPs at layer boundaries modify the field distribution. The modification is rather weak at off-resonance. Generally, if the grating period is much larger than the wavelength, the resonance would not be restricted to normal incidence. But if the grating period is very large (vs. wavelength), SP resonance will not be coupled at normal incidence. Therefore the beginning statement was concluded for subwavelength gratings in our present case.

Further understanding of the in-plane SP band structures can be explained as follows. For a given frequency ω_0 (vacuum wavelength λ_0) of collimated incidence beam, from the SP band structures we can find the corresponding k_{sp} on the horizontal axis. Knowing k_{sp} and ω_0 , we can find the coupling angle θ with Equation (2.46) at a certain order m . For frequencies in the band gap, SPs cannot be coupled at any angle. Therefore, frequency is determinative for the state of SP coupling. On the other hand, in case of oblique incidence ($\theta \neq 0$), for a given θ , there may not exist a frequency for coupling of light into a certain SP mode, which also forms angular band gap. If a SP resonance happens at this angle, the frequencies are those at B.Z. boundaries since the SP propagation direction is only limited to the in-plane surface direction. In the plots of SP band structure, k_{sp} is not simply related to the projection of incidence beam wave vector on in-plane surface by $\sin\theta$. Some SP modes, which exist on the band structures, may not be coupled from incidence light according to Equation 2.46. Particularly at the reduced B.Z. boundaries ($kd/2\pi=0.5$), although there are also SP resonance modes, such modes may not be optically coupled with subwavelength gratings. If it is normal incidence, m is an integer, it's impossible that $\frac{kd}{2\pi} = m \cdot \frac{1}{2}$; if it is oblique incidence, the resonant SP mode may be coupled at a particular angle.

The resonance SP waves have standing wave characteristics. Thus we can describe the field distribution and correlated surface charge distribution based on an analysis of symmetry and Bloch's theorem. Since each metal stripe between two slits are separated, charge neutrality also need to be satisfied. Considering the $m=1$ mode, the charge distribution and field

distribution of only two possibilities are schematically shown in Figure 2.22. At this in-plane SP resonance state, polarization of each island is intensified at top (or bottom) surface. Polarizations of the island top/bottom segments are strongly coupled for adjacent islands. Charge neutrality is even maintained at the segment surfaces, which does not favor the flow of SP charges into the slit segments; at the same time, power dissipation is strong at this state. The reasons are related to the result of transmission dip in the SP polarization, localization and energy absorption points of view.

The above discussion is based on an ideal case of rectangular cross-section islands. Considering the non-ideal fabricated structure and actual small divergence of the incidence beam, two sub-modes of the $m=1$ mode is so close that, they easily overlap with each other and contribute to the spectra minimum. As the incidence angle becomes off-normal direction, the in-plane SP resonance will be weakened, which will result in broadened and shallower transmission dip. It is also seen that the SP mode position are much dependent on the filling factor. This explains the minima red shift with increasing Ag-thickness, which also increases the filling factor in our process.

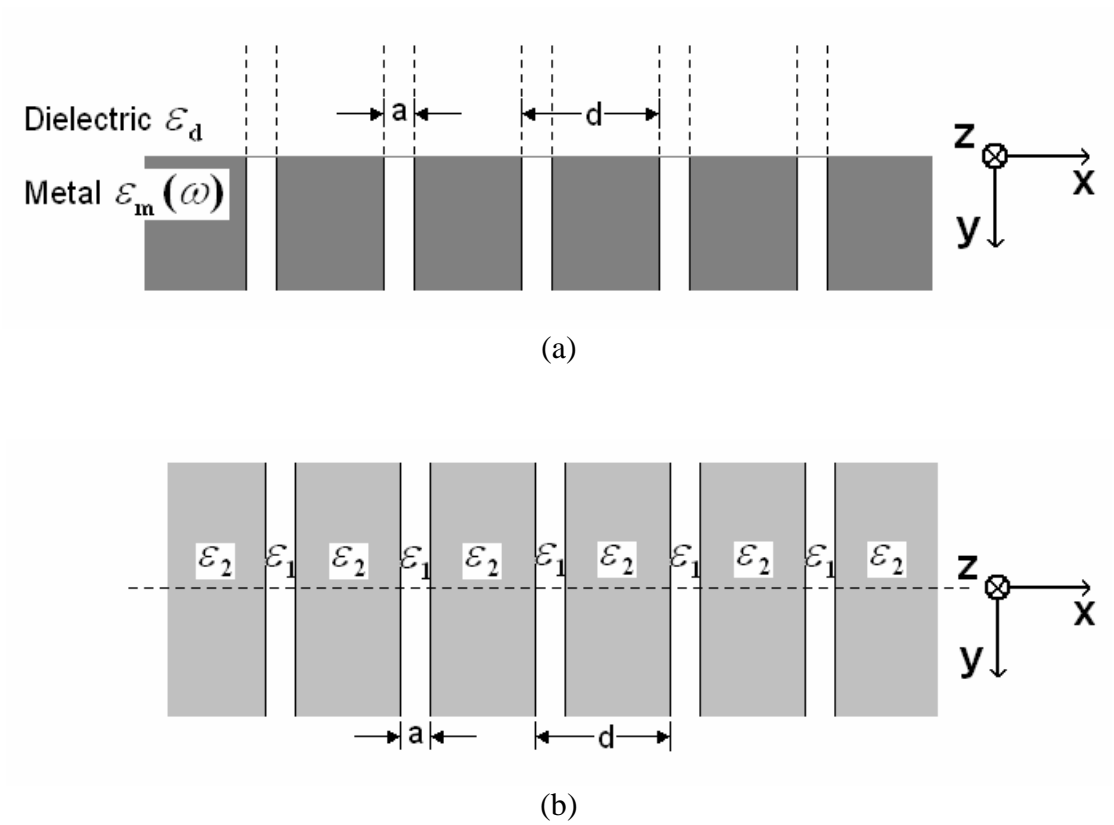
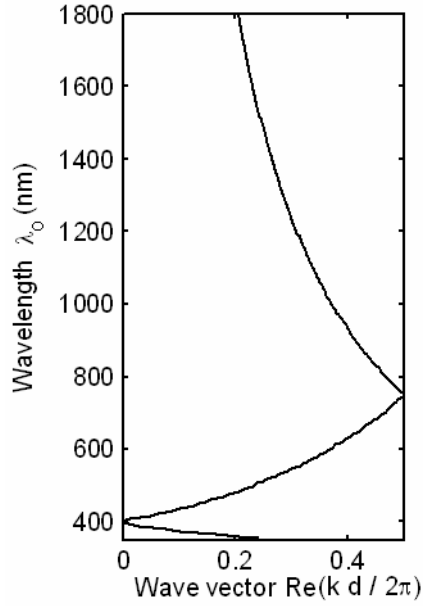
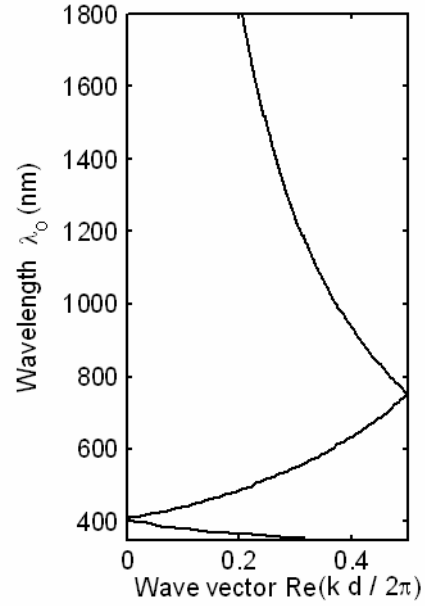


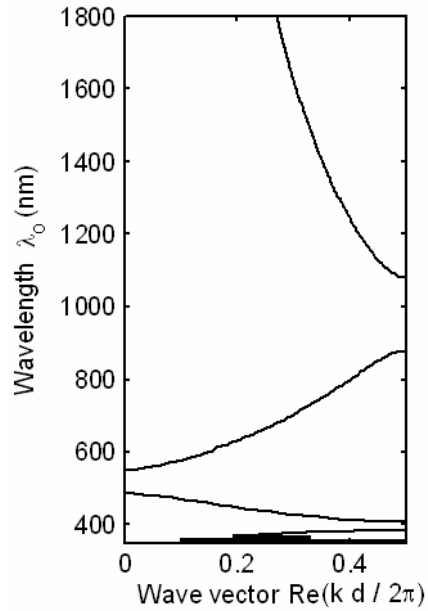
Figure 2.19. Schematic illustration of the model for band structures of SP waves at the top and bottom dielectric/metal interface. (a) The original structure for modeling of SP waves localized at the dielectric/metal interface; (b) The modeled 1D multi-layer structure extended in y -direction from the dielectric/metal interface.



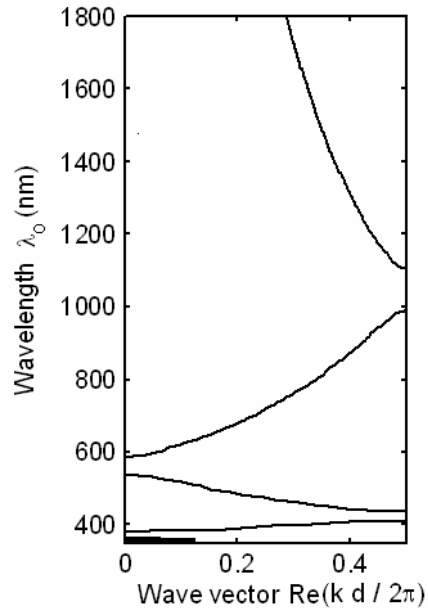
(a) Air/Ag mode: $f = 0.6$



(b) Air/Ag mode: $f = 0.8$

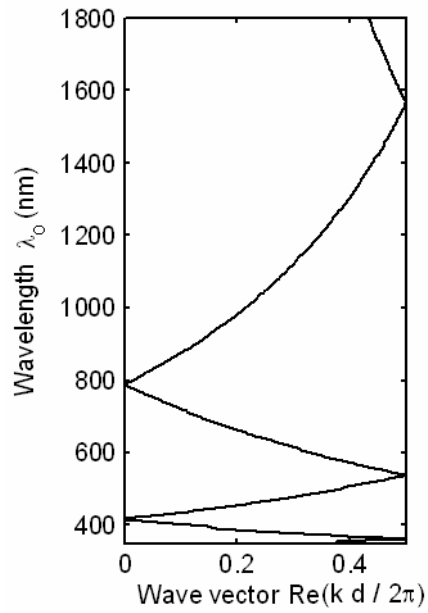


(c) Quartz/Ag mode: $f = 0.6$

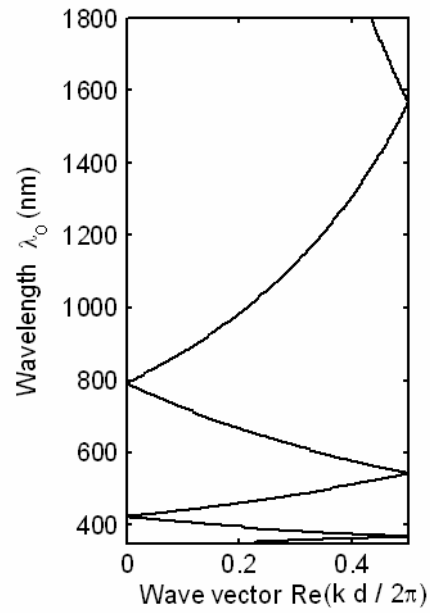


(d) Quartz/Ag mode: $f = 0.8$

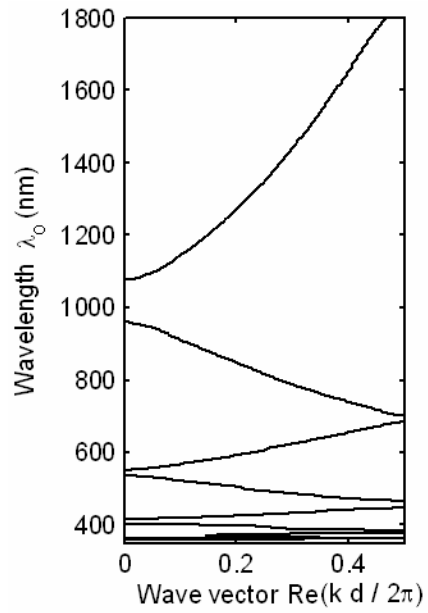
Figure 2.20. Photonic band structures of surface plasmons at the top and bottom dielectric/Ag interfaces of a thick Ag slab with narrow slit arrays. The period of slit arrays is 370 nm. The frequencies in ordinate-axes are converted into corresponding vacuum wavelengths.



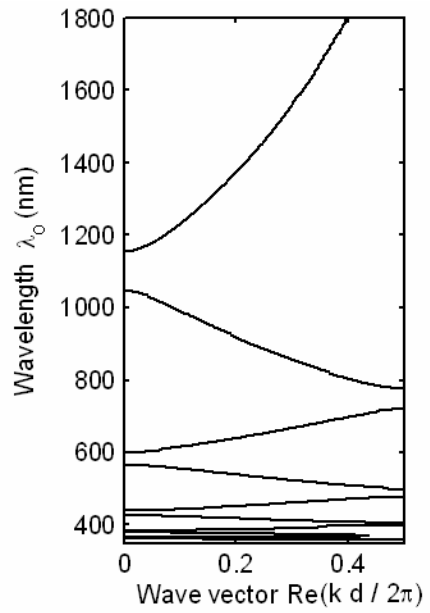
(a) Air/Ag mode: $f = 0.6$



(b) Air/Ag mode: $f = 0.8$

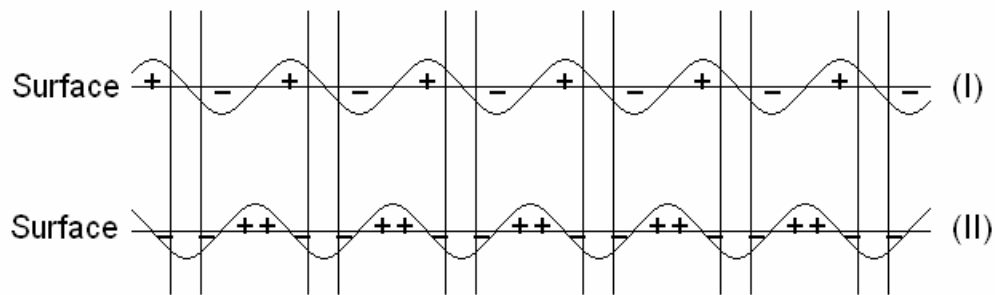


(c) Quartz/Ag mode: $f = 0.6$

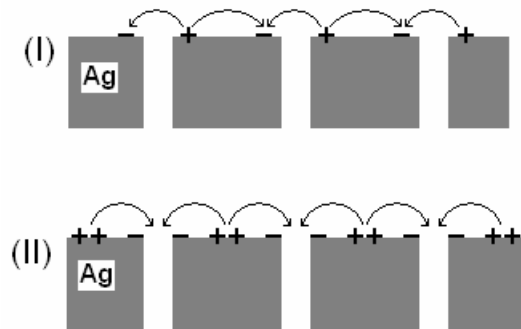


(d) Quartz/Ag mode: $f = 0.8$

Figure 2.21 Photonic band structures of surface plasmons at the top and bottom dielectric/Ag interfaces of a thick Ag slab with narrow slit arrays. The period of slit arrays is 780 nm.



(a) Charge distribution



(b) Electric field distribution

Figure 2.22. Schematic illustration of the charge and electric field distribution of the resonance SP wave modes at B. Z. center ($k_{sp} = 2\pi/d$, $m = 1$). Only two resonance modes shown above are possible for $m = 1$ order. Note that the charge density oscillates with the corresponding frequency of the SP wave mode, which is different for the two modes.

2.6 DYNAMIC POLARIZATION OF INFINITE METALLIC CYLINDERS

From a different perspective, a thick metal slab with narrow slit arrays can also be considered as closely spaced metal wire arrays. Thus, studying the metal wire response to an incident light should also have the same significance as those of a guided plasmon wave through narrow slit and surface plasmon wave propagation at top and bottom surfaces. For analytical modeling, it's easier to consider the metal wires as cylinders, although the shape anisotropy is also important in the process. It is widely studied for small metal spheres that, if the spheres are very small (a few nanometers in diameter), the polarization process is more an electrostatic process. As the structure dimensions scale to be large (10 ~ 100 nm), dynamical polarization effects would be prominent [41]. Similarly, for TM-polarized light incidence, if the wire diameter is on the order of 100 nm, the plasmon resonance induced by dynamical polarization would also play an important role. In the following subsections, we will first present a general and exact solution on dynamic polarization of a metal cylinder and the excited plasmon resonance; then a self-consistent calculation will be shown for the dipolar plasmon resonance of the metal cylinder; finally, the effects of the shape anisotropy on polarization will be discussed.

2.6.1 Exact Solution for the Dynamical Polarization in a Metal Cylinder

Assume a plane wave is incident on a single cylinder with the magnetic field parallel to the cylinder (z) axis, as shown in Figure 2.23. The direction of $\theta = 0$ is taken as the direction of

the wave vector \vec{k} of the incident plane wave. Thus, using polar coordinates (r, θ) , the magnetic field of the incident plane wave can be expressed as [12],

$$\begin{aligned} H_z(\vec{r}, t) &= H_0 e^{i(kr \cos \theta - \omega t)} = H_0 e^{-i\omega t} \sum_{l=-\infty}^{\infty} J_l(kr) \exp\left[il\left(\theta + \frac{\pi}{2}\right)\right] \\ &= H_0 e^{-i\omega t} \left[J_0(kr) + 2 \sum_{l=1}^{\infty} i^l J_l(kr) \cos l\theta \right], \end{aligned} \quad (2.47)$$

where H_0 is the amplitude of the incident wave, $k = |\vec{k}|$, and J_l is the Bessel function of the l -th order. The wave equation in the polar coordinate system that describes the magnetic field H_z is given by

$$\frac{1}{\varepsilon} \left(\frac{\partial^2}{\partial r^2} + \frac{1}{r} \frac{\partial}{\partial r} + \frac{1}{r^2} \frac{\partial^2}{\partial \theta^2} \right) H_z = -\frac{\omega^2}{c^2} H_z, \quad (2.48)$$

where ε stands for the position-dependent dielectric constant and c denotes the light velocity in free space.

As usual, H_z can be expressed by the product of two functions $R(r)$ and $\Theta(\theta)$. Then Equation (2.48) can be split into the following two equations:

$$\frac{\partial^2 \Theta}{\partial \theta^2} = -\varepsilon \lambda \Theta, \quad (2.49)$$

$$\left(\frac{\partial^2}{\partial r^2} + \frac{1}{r} \frac{\partial}{\partial r} + \frac{\varepsilon \omega^2}{c^2} - \frac{\varepsilon \lambda}{r^2} \right) R = 0, \quad (2.50)$$

where λ is the parameter for decoupling. Because $\Theta(\theta)$ should be a single-valued function, $\sqrt{\varepsilon \lambda}$ is an integer, which we denote by n . The solution of Equation (2.49) are thus given by

$$\Theta(\theta) \propto e^{in\theta}, \quad e^{-in\theta}. \quad (2.50)$$

For $r > r_0$ (radius of the cylinder), by defining a variable s , $s = kr$, Equation (2.50) is modified to

$$\left(\frac{\partial^2}{\partial s^2} + \frac{1}{s} \frac{\partial}{\partial s} + 1 - \frac{n^2}{s^2} \right) R = 0. \quad (2.51)$$

This is the Bessel equation and its solution is given by the Bessel and Neumann functions, both of which are analytic for $r > r_0$:

$$R(r) \propto J_n(kr), \quad N_n(kr). \quad (2.52)$$

On the other hand, for $r < r_0$, the dielectric constant $\varepsilon_m(\omega)$ is negative for $\omega < \omega_p$. In this case, s is taken as

$$s = \kappa r, \quad (2.53)$$

where

$$\kappa = \sqrt{-\varepsilon_m(\omega)} \frac{\omega}{c}. \quad (2.54)$$

We thus obtain for $r < r_0$

$$\left[\frac{\partial^2}{\partial s^2} + \frac{1}{s} \frac{\partial}{\partial s} - \left(1 + \frac{n^2}{s^2} \right) \right] R = 0. \quad (2.55)$$

This is the modified Bessel equation and its solution and its solution is given by the modified Bessel function of the first kind,

$$R(r) \propto I_n(\kappa r), \quad (2.56)$$

since the modified Bessel function of the second kind is not analytic at $r = 0$. When we take into account that the geometry is symmetric with respect to θ , the total field is given by [12]

$$H_z = \sum_{n=0}^{\infty} A_n I_n(\kappa r) \cos n\theta \quad (r < r_0), \quad (2.57)$$

$$H_z = \sum_{n=0}^{\infty} [B_n J_n(\kappa r) + C_n N_n(\kappa r)] \cos n\theta \quad (r > r_0), \quad (2.58)$$

where A_n , B_n , and C_n are constants that should be determined by the boundary conditions.

The independent boundary conditions at $r = r_0$ are the continuity of H_z and $\varepsilon^{-1} \partial H_z / \partial r$.

The latter is equivalent to the continuity of the tangential component of the electric field. From these conditions, we obtain

$$\frac{A_n}{B_n} = \frac{k\varepsilon_m [N'_n(kr_0)J_n(kr_0) - N_n(kr_0)J'_n(kr_0)]}{k\varepsilon_m N'_n(kr_0)I_n(\kappa r_0) - \kappa\varepsilon_b N_n(kr_0)I'_n(\kappa r_0)}, \quad (2.59)$$

$$\frac{C_n}{B_n} = -\frac{k\varepsilon_m J'_n(kr_0)I_n(\kappa r_0) - \kappa\varepsilon_b J_n(kr_0)I'_n(\kappa r_0)}{k\varepsilon_m N'_n(kr_0)I_n(\kappa r_0) - \kappa\varepsilon_b N_n(kr_0)I'_n(\kappa r_0)}, \quad (2.60)$$

where ε_b denotes the dielectric constant in the background region. Finally, by comparing Equations (2.47) and (2.58), we obtain

$$B_0 = H_0 \quad \text{and} \quad B_n = 2i^n H_0. \quad (2.61)$$

When A_n/B_n and C_n/B_n were calculated as functions of ω , sharp resonances were observed, which implies the excitation of surface plasmons by the incident plane wave. As shown in Figure 2.24, the ω dependence of A_n/B_n for $n = 1 - 6$ was calculated with an

assumption of Drude metal, $\varepsilon_m(\omega) = \varepsilon_\infty \left(1 - \frac{\omega_p^2}{\omega^2} \right)$. Sharp resonance peaks were shown for each

curve. There is no resonance peak observed with $n = 0$. With increasing n , the resonance frequency converges to $\omega_{sp} = \omega_p / \sqrt{1 + \varepsilon_b}$, a value same as that of the surface plasmon on a flat interface between a metal and a dielectric. As shown in Figure 2.24, the corresponding normalized frequency is

$$\frac{\omega_{sp} r_0}{2\pi c} = \frac{\omega_p}{\sqrt{2}} \cdot \frac{r_0}{2\pi c} = \frac{0.3}{\sqrt{2}} = 0.2122.$$

These resonant states have a finite radiative lifetime if the metal cylinder is a single scattering object. But as such cylinders are arrayed in a photonic crystal system, the resonant states can propagate from one cylinder to another to become a Bloch eigen-state and obtain a much extended lifetime. Because the resonant states are localized at each cylinder, they are similar to the atomic orbitals, i.e. the EM field of the eigenmodes of the SP polaritons is localized around the surface of the metallic cylinders and there is small overlapping of the field between adjacent cylinders, as stated in Reference [12]. The stable resonant states obey the symmetry of the 2D cylinder arrays with particular angular variation of the magnetic field around the surface of the metallic cylinders.

For 1D cylinder arrays, which we consider in modeling of our structure, propagating resonant modes can be formed along the cylinder chain directions. As shown in Figure 2.25(a), the structure is invariant when it is rotated by 180 degrees, which denote the symmetry operation C_2 . It is also invariant under the mirror reflection σ_x that changes x to $-x$. Together with the identity operation E that keeps the structure as it is, all the symmetry operations constitute the C_{2v} point group for the 1D structure:

$$C_{2v} = \{E, C_2, \sigma_x\}. \quad (2.62)$$

Since C_2 and σ_x operations are interchangeable with each other, they are conjugate and considered to be the same. With a little further investigation, we will find Γ , Δ ($0 < k < \pi/d$) and X point in the first Brillouin zone, shown in Figure 2.25(b), hold the same point group C_{2v} . Additionally, the eigenfunction at these points is either symmetric or anti-symmetric because of the mirror reflection symmetry about y-axis. When we combine it with the angular (θ) dependence of the resonant state, given by $e^{\pm in\theta}$ for each $n \geq 1$, the resonant states can be characterized by index n with one symmetric and one anti-symmetric mode for Γ (or Δ , X) point. Thus, the C_{2v} point group has two non-degenerate irreducible representations A_1 , A_2 and one two-fold degenerate irreducible representation E , as shown in Figure 2.25(c). The symmetric angular variation of the magnetic field of the resonant modes for $n=1-4$ is also shown in Figure 2.26.

If the cylinders are very close to each other, e.g. the separation is in the range of $\leq 100nm$ for visible and IR optical frequencies, the cylinder surface field will be coupled to each other in a similar way as discussed in Section 2.4. Large overlapping of the adjacent cylinder field will be analogous to “covalent electron cloud” of atomic electronic bonding in some condensed matters. Since our structure is a 1D chain, there are only propagation resonance modes in one direction (along x-axis). The field in y-axis will radiate and be released into propagation modes in far field. Thus the coupling between 1D cylinders has low efficiency for higher resonance modes. For low order resonance mode (e.g. $n = 1$), surface plasmon waves will be more easily coupled and propagating along the cylinder chain direction with high absorption, which will result in low transmission, e.g. the transmission dip at ~ 800 nm in Figure 2.5.

In the next subsection, a self-consistent analysis will be shown for a calculation of the dipolar ($n = 1$) plasmon resonance of the metal cylinder.

2.6.2 Dipolar Plasmon Resonance inside a Metal Cylinder

We still consider a plane wave incident on an infinite metallic cylinder (ε) in air background with TM-polarization, as shown in Figure 2.23. Starting from a fundamental level, we assume the polarization \vec{P} is homogeneous over the cross section of the cylinder, which can be calculated from

$$4\pi\vec{P} = (\varepsilon - 1)(\vec{E}_0 + \vec{E}_{dep}), \quad (2.63)$$

in Gaussian units, where \vec{E}_0 is the externally applied field and \vec{E}_{dep} is a depolarization field generated by the polarized matter surrounding the center. Each volume element in unit length (take r_0 , radius of the cylinder, as the length scale), $dV(\vec{r}) = r d\theta dr$, can be considered to contribute a dipole moment

$$d\vec{p}(\vec{r}) = \vec{P} dV(\vec{r}) = \vec{P} r_0 r dr d\theta. \quad (2.64)$$

Thus we can calculate the depolarization field by first calculating the retarded dipolar field $d\vec{E}_{dep}$ generated by $d\vec{p}(\vec{r})$ at the center and then integrating over the volume of the cylinder with a unit length.

It is known that the field produced by a linear retarded electric dipole $[p] = pe^{ikr}$ is given by [2]

$$\vec{E} = \vec{D} = \left\{ \frac{3[p]}{R^5} + \frac{3[\dot{p}]}{cR^4} + \frac{[\ddot{p}]}{c^2R^3} \right\} (\vec{n} \cdot \vec{R}) \vec{R} - \left\{ \frac{[p]}{R^3} + \frac{[\dot{p}]}{cR^2} + \frac{[\ddot{p}]}{c^2R} \right\} \vec{n}, \quad (2.65)$$

$$\vec{B} = \vec{H} = \left\{ \frac{[\dot{p}]}{cR^3} + \frac{[\ddot{p}]}{c^2R^2} \right\} (\vec{n} \times \vec{R}), \quad (2.66)$$

Here, \vec{n} denotes the dipole orientation; \vec{R} is the displacement of the observation point to the dipole position; and c is the light speed in free space. In the polar coordinate, taking the \vec{n} direction as the y -axis (see Figure 2.23) and denoting by \hat{e}_r , \hat{e}_θ and \hat{e}_z the unit vectors in the direction of increasing r , θ and z , we have in the cross section of the cylinder

$$\begin{aligned} \vec{R} &= r\hat{e}_r, & \vec{n} &= (\sin \theta)\hat{e}_r + (\cos \theta)\hat{e}_\theta, \\ (\vec{n} \cdot \vec{R}) &= r \sin \theta, & (\vec{n} \times \vec{R}) &= -(r \cos \theta)\hat{e}_z, \end{aligned} \quad (2.67)$$

and Equations (2.65) and (2.66) give

$$\vec{E} = E_r\hat{e}_r + E_\theta\hat{e}_\theta, \quad \vec{H} = H_z\hat{e}_z, \quad (2.68)$$

where

$$E_r = 2 \left(\frac{[p]}{r^3} + \frac{[\dot{p}]}{cr^2} \right) \sin \theta, \quad (2.69a)$$

$$E_\theta = - \left(\frac{[p]}{r^3} + \frac{[\dot{p}]}{cr^2} + \frac{[\ddot{p}]}{c^2 r} \right) \cos \theta, \quad (2.69b)$$

$$H_z = - \left(\frac{[\dot{p}]}{cr^2} + \frac{[\ddot{p}]}{c^2 r} \right) \cos \theta. \quad (2.69c)$$

By expanding e^{ikr} , retaining terms up to order k^3 , i.e.

$$e^{ikr} \approx 1 + ikr - \frac{1}{2}k^2 r^2 - \frac{1}{6}ik^3 r^3 + O(r^4), \quad (2.70)$$

and considering $k = \frac{\omega}{c}$, $[\dot{p}] = (-i\omega)[p]$, and $[\ddot{p}] = (-\omega^2)[p]$ for a monochromatic dipole, we can

have approximately

$$E_r = 2 \left(\frac{1}{r^3} + \frac{k^2}{2r} + \frac{ik^3}{3} \right) p \sin \theta, \quad (2.71a)$$

$$E_\theta = - \left(\frac{1}{r^3} - \frac{k^2}{2r} - \frac{2ik^3}{3} \right) p \cos \theta. \quad (2.71b)$$

In this problem, the components of depolarization field, generated by element dipole $d\vec{p}(\vec{r})$, perpendicular to \vec{E}_0 cancel on integration, only the parallel component $dE_{dep, //}$, along y -

axis, must be considered. By substituting the corresponding relations of Equations (2.71a) and (2.71b) for element dipole $d\bar{p}_{//}(\bar{r})$, field $dE_{dep,r}$ and $dE_{dep,\theta}$ into

$$dE_{dep,//} = dE_{dep,r} \sin \theta + dE_{dep,\theta} \cos \theta, \quad (2.72)$$

we have

$$dE_{dep,//} = \left[\frac{1}{r^3} (2 - 3 \cos^2 \theta) + \frac{k^2}{2r} (2 - \cos^2 \theta) + \frac{2}{3} ik^3 \right] d\bar{p}_{//}(\bar{r}), \quad (2.73)$$

where $d\bar{p}_{//}(\bar{r}) = d\bar{p}(\bar{r}) = \bar{P} r_0 r dr d\theta$. Integration over the volume of the cylinder with radius r_0 and unit length r_0 yields

$$\bar{E}_{dep} = \left(-2\pi + \frac{3\pi}{2} r_0^2 k^2 + i \frac{2\pi}{3} r_0^3 k^3 \right) \bar{P}. \quad (2.74)$$

Here, the first term is the electrostatic depolarization, which needs to be introduced by the approach of static electromagnetism because of the non-converging in integration here; the second term is the dynamic depolarization; and the third term accounts for damping of the dipole by radiative losses. Inserting this result into Equation (2.63), one obtains

$$\bar{P} = \frac{1}{2\pi} \frac{(\varepsilon - 1)}{(\varepsilon + 1) - \frac{3}{4}(\varepsilon - 1)q^2 - i \frac{1}{3}(\varepsilon - 1)q^3} \bar{E}_0 \quad (q = kr_0). \quad (2.75)$$

Under plasmon resonance, the denominator in Equation (2.75) vanishes. Assume $\varepsilon = \varepsilon_1 + i\varepsilon_2$, the resonance condition is

$$\varepsilon_1 \left(1 - \frac{3}{4} q^2 \right) + \left(1 + \frac{3}{4} q^2 \right) + \varepsilon_2 \left(\frac{1}{3} q^3 \right) = 0. \quad (2.76)$$

Since usually $|\varepsilon_2| \ll |\varepsilon_1|$, imaginary part of the denominator is not considered here. If the cylinder radius r_0 is much smaller than the free space wavelength ($\lambda_0 = \omega/c$), the third term in Equation (2.76) can be neglected, i.e.

$$\varepsilon_1 \left(1 - \frac{3}{4} q^2 \right) + \left(1 + \frac{3}{4} q^2 \right) = 0 \quad \left(r_0 \ll \frac{\omega}{c} \right). \quad (2.77)$$

Numerically, the dipolar plasmon resonance position (λ_0) dependence on a silver cylinder radius (r_0) was calculated within a free space wavelength range of 350 ~ 1800 nm and shown in Figure 2.27(a). And it was compared that, in this wavelength range, the result discrepancy from Equations (2.76) and (2.77) is really negligible. In the calculations, the dielectric constants of silver were taken from experimental data [6]. The dependence on circumference ($L = 2\pi r_0$) of the cylinder cross-section was also shown in Figure 2.27(b). At longer wavelengths, the dependence can be linearly fitted by $\lambda_0 = 0.85L + 50$. Usually in the wavelength range being considered, $50 \ll 0.85L$ (corresponding $L = 500 \sim 2000nm$), we can approximately determine the dipolar plasmon resonance position with

$$\lambda_0 \approx 0.85L. \quad (2.78)$$

Although Equation (2.78) is obtained based on the analysis of a circular cylinder, it fits the transmission dip at longer wavelength in Figures 2.5 and 2.6 (with 240 nm-thick-Ag), due to negative role of dipolar plasmon resonance of the Ag islands on transmission, rather well considering certain assumptions and taking the circum-length of the cross-section as L . Thus, we may extend the relations, Equation (2.78), to roughly determine the dipolar plasmon resonance position of a silver rod with its non-regular cross-section having close lengths in two dimensions and not having sharp curvatures. Otherwise, effects of shape anisotropy on surface plasmon distribution become prominent [43, 44]. It is noted that all the analysis above have included an assumption of having small/negligible imaginary part of dielectric constant; thus, the results may not be readily applied to metals other than silver.

Generally, when TM-polarized light is incidence on a metal nano-rod, the fields are enhanced at the metal surfaces. Under plasmon resonance, the metal rod is polarized in dipole or multi-pole mode; along the circum-path of the rod cross-section, amplitudes of the fields vary in phase. If the metal rod has an isotropic shape, the same surrounding media and symmetric nearby scatterers, the fields will distribute along the circum-path symmetrically; and the charge distribution, simply the divergence of the electric field, will be also symmetric. If the metal rod has a cross-section with an anisotropic shape, the fields and also the charges will concentrate at sharp corners. Then, each relatively uniform segment of the circum-path will introduce sub-modes of plasmon resonance for the metal rod.

2.6.3 Coupling of Plasmon Resonance Mode between Arrayed Metallic Cylinders

With exact solutions for scattering of TM-polarized light by a metallic cylinder, in Figure 2.28, plotted are the polar H_z -field distributions of $n = 1, 2$ local surface plasmon resonance modes and an off-tuned non-resonance state in both near ($r = r_0$) and far ($r = 100r_0$) fields. It is seen that, at the metal surface ($r = r_0$), the field is dramatically enhanced in certain symmetric directions for resonance mode; while the field is not much enhanced for non-resonance and the corresponding angular distribution is not highly symmetric. But, far from the cylinder ($r = 100r_0$), both field magnitude and angular distribution are rather similar. It suggests the local surface plasmon resonance does not apparently affect the field (and intensity) distribution in far field if $|Im(\varepsilon)| \ll |Re(\varepsilon)|$ is assumed, e.g. for Ag. As it was stated in Subsection 2.6.1, it is the coupling of the field of resonance modes between cylinders and guiding of localized photon waves along the cylinder chain that dramatically reduced light transmission (or guiding) through the slits with plasmon modes of different characteristics.

Since the 1D cylinder array has only 1D resonance “cavity” along the chain direction, only dipole plasmon resonance coupling is efficient. The Figure 2.29 schematically illustrates the fields (or charge) distributions of the coupling between cylinders. Shown in the figure, $\psi_a^{(s)}$, $\psi_b^{(s)}$, $\psi_a^{(a)}$, and $\psi_b^{(a)}$ are states of the plasmon modes in single metal cylinders with subscripts distinguishing different cylinders and superscripts distinguishing the symmetry of the plasmon

mode relative to coupling direction. As dipolar plasmon resonant cylinders are adjacent to each other, there are two combinations, which result in $\psi_1^{(s)}$ coupling and $\psi_2^{(s)}$ anti-coupling (or $\psi_1^{(a)}$ and $\psi_2^{(a)}$). For anti-coupling, the cylinders will be in great potential and thus the system is not stable; for coupling, the system maintains with low energy potential, therefore, it's a stable state. Any dipolar component of coupling between the adjacent cylinders is a combination of these two eigenstates. The situation rather resembles the bonding between atoms in condensed matter molecules: the dipole plasmon resonance is an equivalent to the atom p-orbit resonance and the coupling forms π_p -bond and π_p^* -bond corresponding to $\psi_1^{(s)}$ and $\psi_1^{(a)}$ coupling. Here, the 1D cylinder array can be considered as a “super-molecule-chain” bonded by resonant plasmon couplings.

Figure 2.30 also shows the dipolar plasmon coupling of metallic rods with rectangular-like cross-sections, where fields and charges are more concentrated at the corners due to shape anisotropy. Since analytical solution of such a structure is difficult, FDTD simulations showed such distributions in Section 2.7. For normal incidence of light onto the 1D structures, the anti-symmetric mode coupling $\psi_1^{(a)}$ is reasoned to be more prominent with more overlapping of fields between cylinders, which can be also inferred from Ref. [45] indicated with higher scattering cross-section peak.

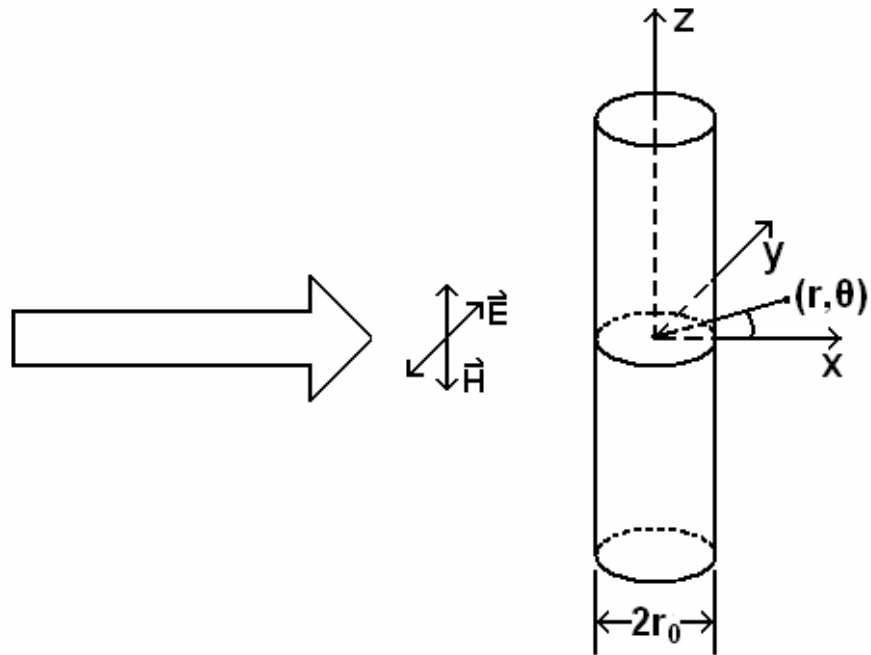


Figure 2.23. Illustration of a plane wave incident on an infinite length metal cylinder with TM-polarization. Also defined in the figure are rectangular coordinate and polar coordinate for analysis.

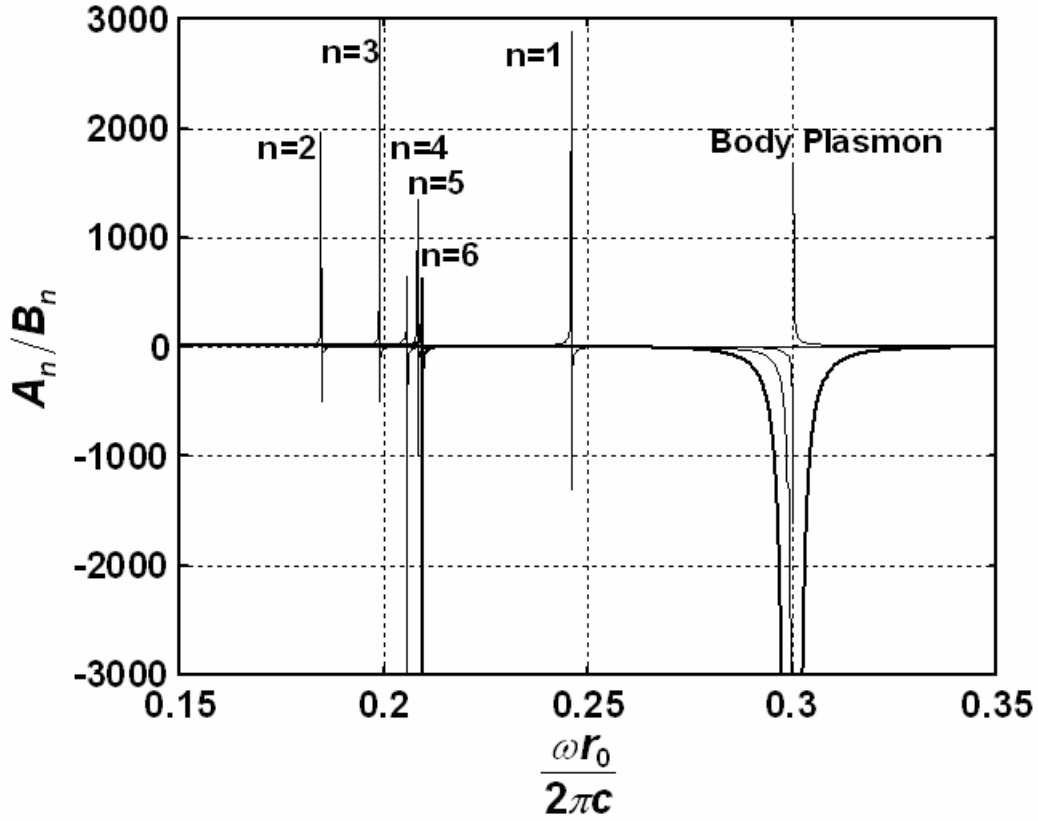
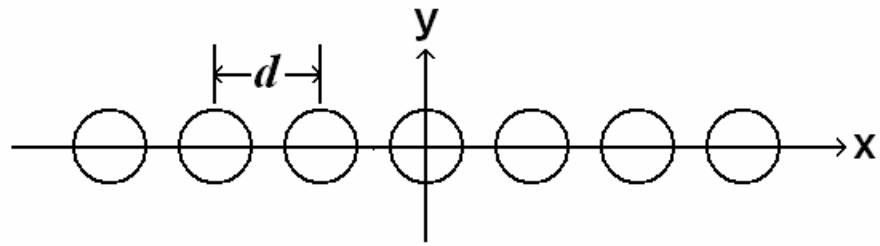
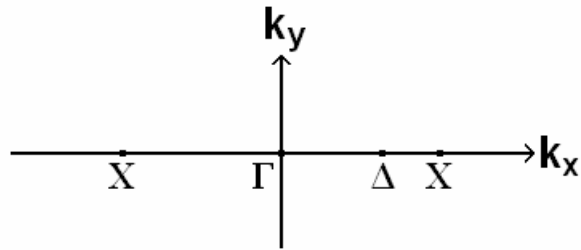


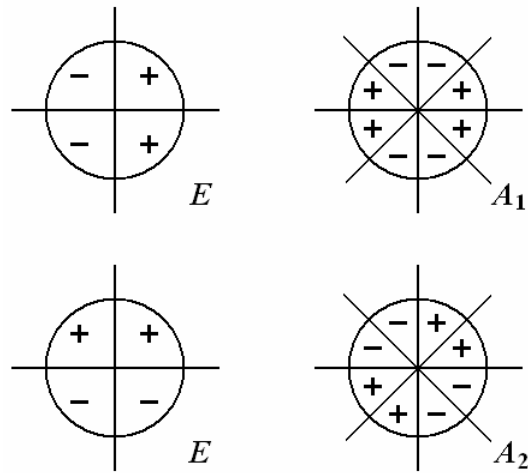
Figure 2.24. Dependence of A_n/B_n on ω for $n=1-6$. The following parameters were assumed for the Drude metal: $\epsilon_\infty = 1$, $\omega_p r_0 / 2\pi c = 0.3$, and $\epsilon_b = 1$ (air). The body plasmon resonance is also shown. The normalized frequencies for $n=1-6$ are 0.2458, 0.1845, 0.1989, 0.2054, 0.2081 and 0.2093 respectively. Refer to Reference [33].



(a) Geometry of the metallic cylinder array



(b) First Brillouin zone of the 1D cylinder array



(c) Symmetry of irreducible representations of the C_{2v} point group

Figure 2.25. Symmetry of irreducible representations of the C_{2v} point group for a metallic cylinder array.

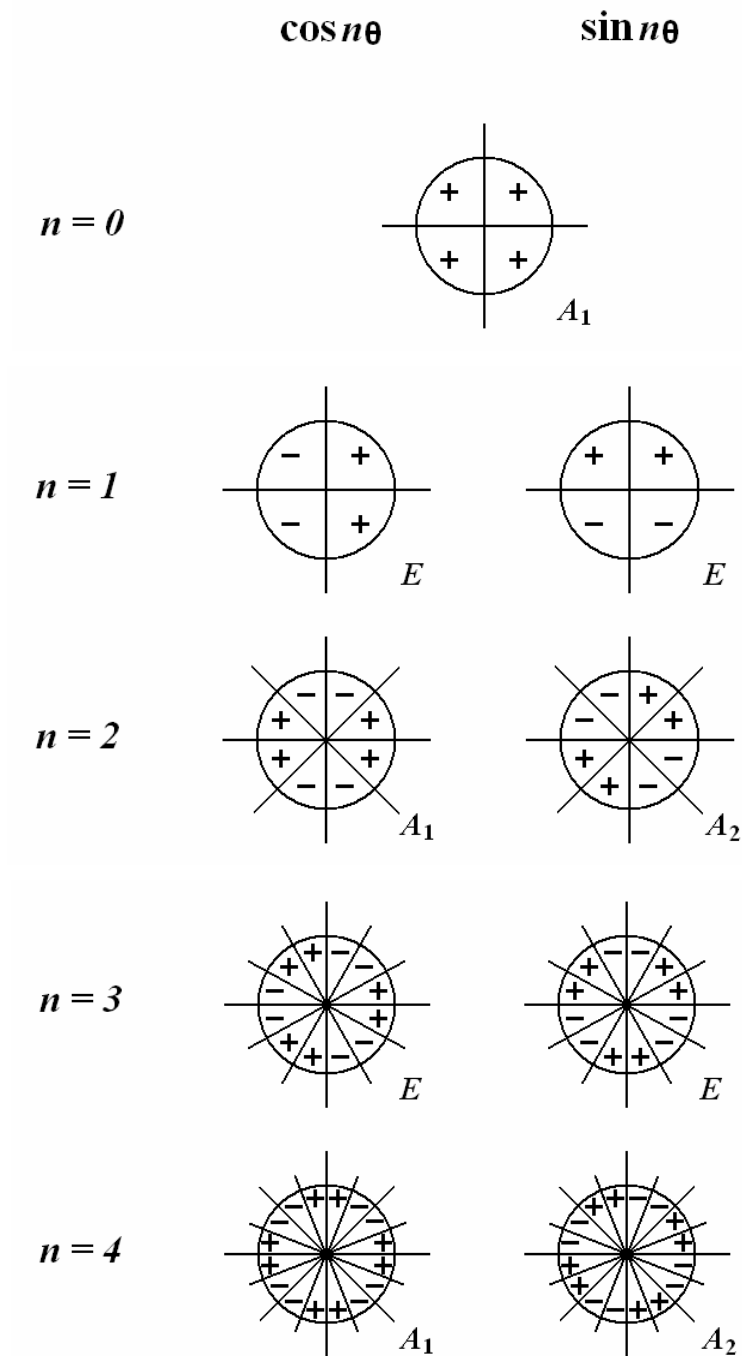
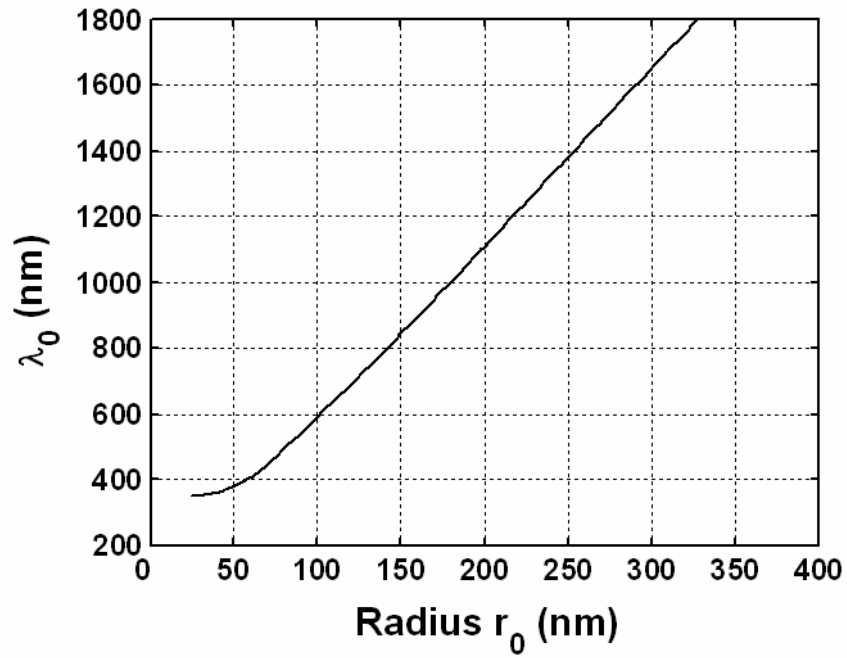
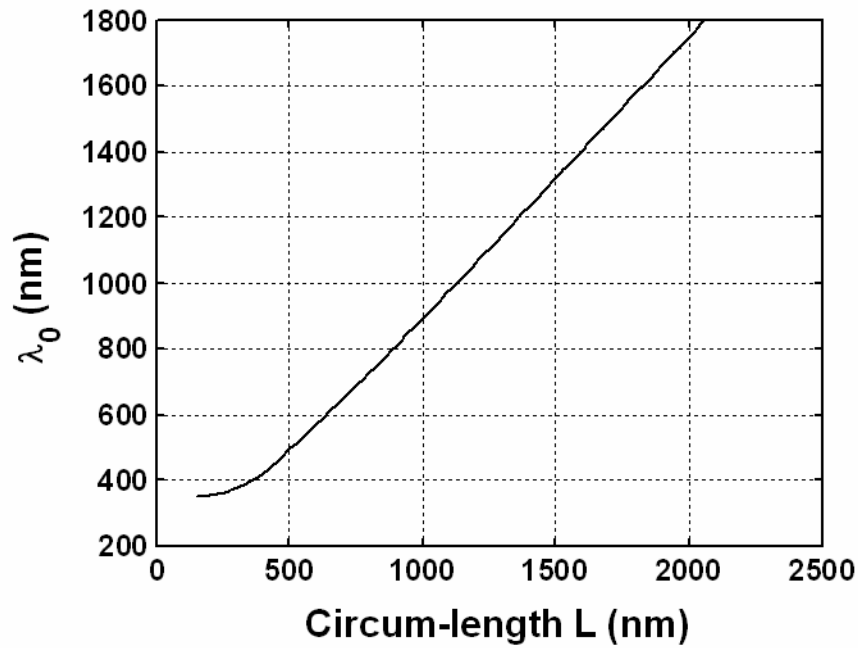


Figure 2.26. The angular variation of the magnetic field and the symmetry assignment of the resonant states according to the irreducible representations of the C_{2v} point group.



(a)



(b)

Figure 2.27. Dipolar plasmon resonance position dependence on size of a silver cylinder in air background. Shown in the figure are dependences of corresponding free space wavelength on cylinder cross-section (a) radius r_0 and (b) circum-length $L = 2\pi r_0$.

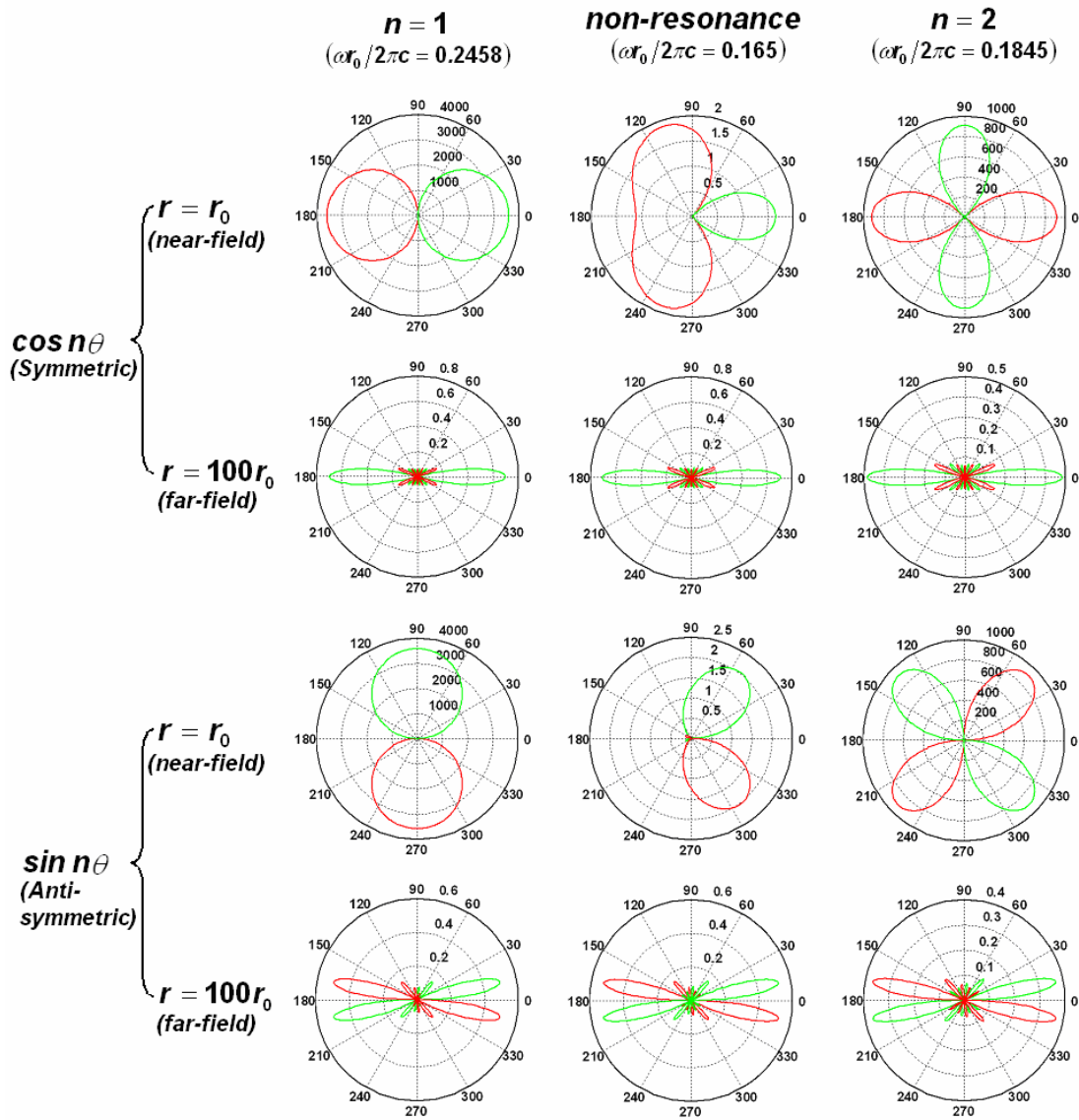


Figure 2.28. Polar distribution of the Hz-field scattered by a metallic cylinder at near and far fields. The coordinate is as defined in Figure 2.19. H_0 of incident light is one. Red and green color of the curves indicates the opposite sign (“+” and “-”) of the field.

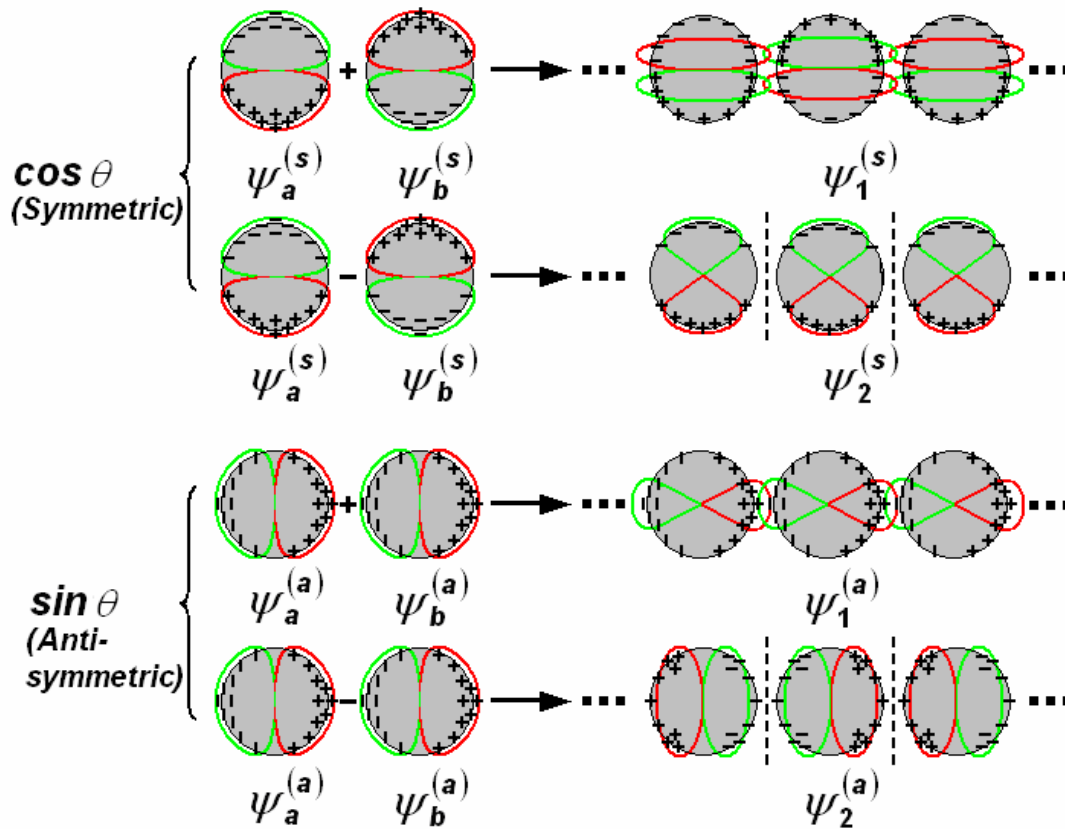


Figure 2.29. Coupling of dipolar plasmon modes between 1D-arrayed metallic cylinders. $\psi_1^{(s)}$ and $\psi_1^{(a)}$ are stable coupling; $\psi_2^{(s)}$ and $\psi_2^{(a)}$ are unstable anti-coupling. Red and green curves are schematic polar distribution of the charge density (or field intensity) at the metal surfaces; the color shows the polarity of charges or field.

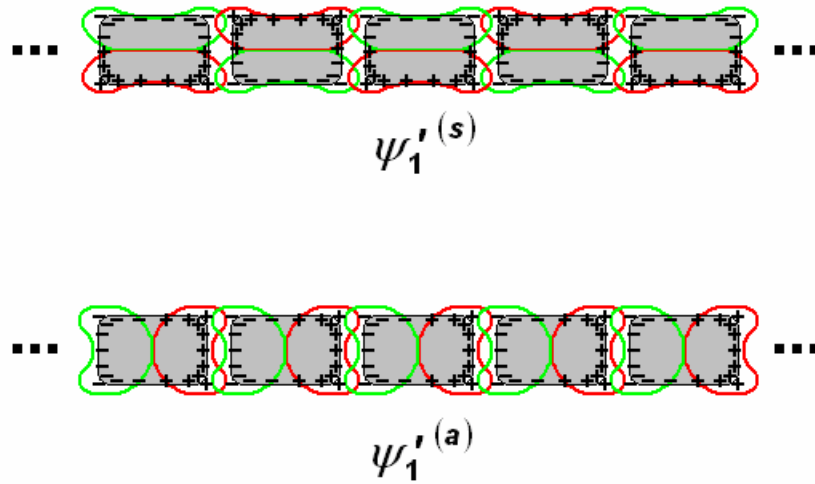


Figure 2.30. Coupling of dipolar plasmon modes between 1D-arrayed metallic rectangular pillars. Shown in figure are two stable coupling states $\psi_1^{(s)}$ and $\psi_1^{(a)}$. Red and green curves are schematic polar distribution of the charge density (or field intensity) at the metal surfaces; the color shows the polarity of charges or field.

2.7 FDTD SIMULATION OF FIELD AND CHARGE DISTRIBUTIONS

Using the finite-difference time-domain (FDTD) simulation method, Maxwell equations were solved numerically for the transmission problem, which is schematically illustrated in Figure 1.4(a). The problem region was uniformly discretized with 551×551 mesh points; each mesh unit represents for a real dimension of 10 nm. The structure simulated has a thickness of 200 nm, slit width of 80 nm and slit spacing (center to center) of 370 nm involves adjacent media of silica ($\varepsilon = 2.16$) on the top side and air ($\varepsilon = 1$) on the bottom side. The imaginary part of the dielectric constants of silver was ignored in this simulation for convenience. The field components (H_z , E_x , E_y) were calculated in a wide range of wavelengths from 400 ~ 1500 nm. The excitation source was TM polarized sinusoidal monochromatic wave at individual wavelengths. While the slit spacing (center to center) was fixed to 370 nm, the silver thickness was varied to 80, 120 or 200 nm, and slit width to 50, 80, or 120 nm. The number of time steps is 2000 generally unless being specified.

Figure 2.31 shows the transmission spectra obtained from the simulation with different structural conditions. It should be noted that the small fluctuations of transmittance should not be considered in the analysis, which is due to the cavity effects introduced by non-ideal absorbing boundary conditions of the problem region in simulation. Generally, it is seen that (1) the wavelength filtering is more prominent with increased metal film thickness, and there is almost no clear pass band for the thickness of 80 nm; I.e., the main pass band transmittance is higher for increased film thickness, while transmittance at side lobes is lower with increased film thickness;

(2) The decreased slit width does not apparently reduce the transmittance at main pass band; (3) With increased slit width, the transmittance at longer wavelengths are apparently increased; (4) At large film thickness, 120 nm and 200 nm, the main transmission peak shifts towards longer wavelength with thicker film, which shows the same trend as those experimental results shown in Figure 2.5 and Figure 2.6; (5) the transmission spectra for thick films show a prominent dip at the wavelength of 540 nm, which is at the in-plane surface plasmon resonance condition at silver/silica interface.

Figure 2.32 and Figure 2.33 show the simulated Hz-field and charge distribution at particular wavelengths. The charge distribution was calculated with the electric Gauss's Law

$$\nabla \cdot \bar{D}(\bar{r}) = -\rho(\bar{r}) \quad \text{with} \quad \bar{D}(\bar{r}) = \varepsilon(\bar{r}) \cdot \bar{E}(\bar{r}), \quad (2.79)$$

where ρ is the charge density. Since no free charges are assumed ($\rho = 0$), the SP polarization charge density, $-\nabla \cdot P$ is equal to $\varepsilon_0 \nabla \cdot E$, where P is the SP polarization. For charge distribution in Figure 2.33, the instant states were shown at different time steps within $0 \sim 5\pi/6$ phase interval. The states within $\pi \sim 2\pi$ can be obtained by transforming those within $0 \sim 5\pi/6$ phase interval. It is noted that, although shown in Figure 2.32 is Hz-field distribution, the total electric field has the same distribution, which is just related to the magnetic field with media

$$\text{impedance at each local point, } |\bar{E}(\bar{r})| = \sqrt{\frac{\mu(\bar{r})}{\varepsilon(\bar{r})}} \cdot |\bar{H}(\bar{r})|.$$

With the field and charge distributions information available, the transmission characteristics can now be better understood. It should be mentioned that, in interpreting the simulation results we should also take into account the shape anisotropy and local scattering effects. Particularly at the sharp corners, the fields and charges tend to concentrate. Thus, the overall evolution of charge distribution along the metal surface shows a complex pattern, revealing the retardation/acceleration effects caused by reflection at the corners.

At 420 nm wavelength, the metal surface is polarized with multipoles (hexa-pole dominant), which evolves along the surface over time. Due to the mismatch between the hexa-pole odd-symmetry (3-fold) and structural even-symmetry (2-fold) and influence of shape anisotropy, the charge distribution may also appear as a quadrupole at some time point. Overall, there is no stable resonance state of charge fluctuation along the metal surface or any segment. Field distribution also changes correspondingly. Although the (λ/a) ratio is small, the transmission of guide plasmon mode is much retarded due to the large effective refractive index at this wavelength regime. The near-field field distribution is rather complex and is not favorable for release of power into far field.

At 540 nm wavelength, the in-plane resonant surface plasmon wave is excited, which satisfies the phase matching conditions of photon-SP coupling at the silver/silica interface. It is clearly seen that the field is strongly localized and much extended near the silver/silica interface and the field polarity fluctuation perfectly matches the periodicity of the silver grating structures. The light-plasmon wave is retarded at this interface, which results in low transmission in far field. From the charge distribution, it is also seen that a stable charge distribution is formed at the

silver/silica interface. The distribution is not consistent with the symmetry of the silver cross-section. The silver/silica in-plane charge distribution does not evolve within phase intervals.

At 680 nm wavelength, a maximum transmission is observed. From the field distribution, it is seen that, after transmission of light through the slits, the power is quickly released to a propagating plane wave. There is no strong retardation of the power at the silver regions. The transmission through the slits with a plasmon mode is more easily seen from the charge distribution. Affected by the shape anisotropy, it looks like a quadrupole at each silver island cross-section surface. But when we carefully inspect the charge distribution along the sides of the slits, it is seen that it evolves like a passing plasmon wave. Since the slit depth is small, the transmission plasmon wave resonance cannot be well confined.

At 800 nm (or 820 nm) wavelength, a discrepancy between the simulation result and experimental and analytical result appears. No sharp transmission dip is observed in the simulation, and no strong local dipolar surface plasmon resonance appears along the cross-section metal surface. This may be attributed to the effects of structural difference. It rather appears to be a transition state from the shape anisotropy induced 2-fold quadrupole polarization to the low 1-fold dipole polarization at longer wavelengths where fine shape effects are emerged.

At 1500 nm longer wavelength, it's seen that the metal islands are dipolar polarized and coupled with adjacent ones. This may not necessarily be a resonant coupling between the neighbored islands. The phase mismatching between the local surface plasmon resonance and the dipolar coupling can be compensated by retardation/acceleration or scattering at the island

boundaries. This scattering contributes to the reflection and transmission in part. It is speculated that the deep transmission dip in experimental result is where there is a good match of the local surface plasmon resonance and dipolar coupling, which retard the power transmission.

The transmission problem may be better understood with simulation of the energy flow. In Figure 2.34, the instant power flows, i.e. Poynting vector, were calculated with FDTD simulated field distributions: $\vec{S} = \vec{E} \times \vec{H}$. At the wavelength of 540 nm, Figure 2.34 (a) shows a significant amount of power flows out of the slits, but it sharply deflects towards the metal surface upon exiting the slits. The excited power flows back and forth along the in-plane direction on the metal surface. The spatial period of the power flow distribution matches the field distribution shown in Figure 2.32 (at 540 nm wavelength), equal to the array period. A power flow component normal to the substrate exists in some near field region, but it does not propagate away into the far field region. At the wavelength of 680 nm [Figure 2.34 (b)], the power flow distribution reveals that the incident power is well funneled into each slit. The effective area of funneling is found to be extensive covering nearly entire spacing between slits. The transmitted power radiates away from slits and forms a propagating wave in the far field region. The fields localized on the slit array surface quickly evolve into planar wavefronts in less than one wavelength of propagation. At the wavelength of 1500 nm optical transmission is found significantly decreased. A fraction of incident power transmits through each slit, but the funneling effect is significantly reduced. This suggests that near-field coupling between neighboring metal islands may occur altering the SP dynamics and the far-field distribution of optical fields. At narrow slit width, the surface plasmon fields localized at each metal island are expected to couple each other via a tunneling process [45-47]. Once strong coupling occurs

between metal islands, the islands become virtually connected (despite a gap) from the surface plasmon oscillation point of view. AP propagation along the slits will eventually be blocked and the transmission spectra would show profiles similar to those of metal without slits.

Generally, it is shown that the lateral resonant coupling of (in-plane or local) surface plasmon waves redirect the power flow and retard the power transmission in far field. While higher order localized surface plasmons around islands enhances the transmission by funneling of power into the slits and efficiently reradiate into the other side. In the present case, the metal layer is relatively thin compared to wavelength; the resonance along the slit depth has no strong effect on transmission.

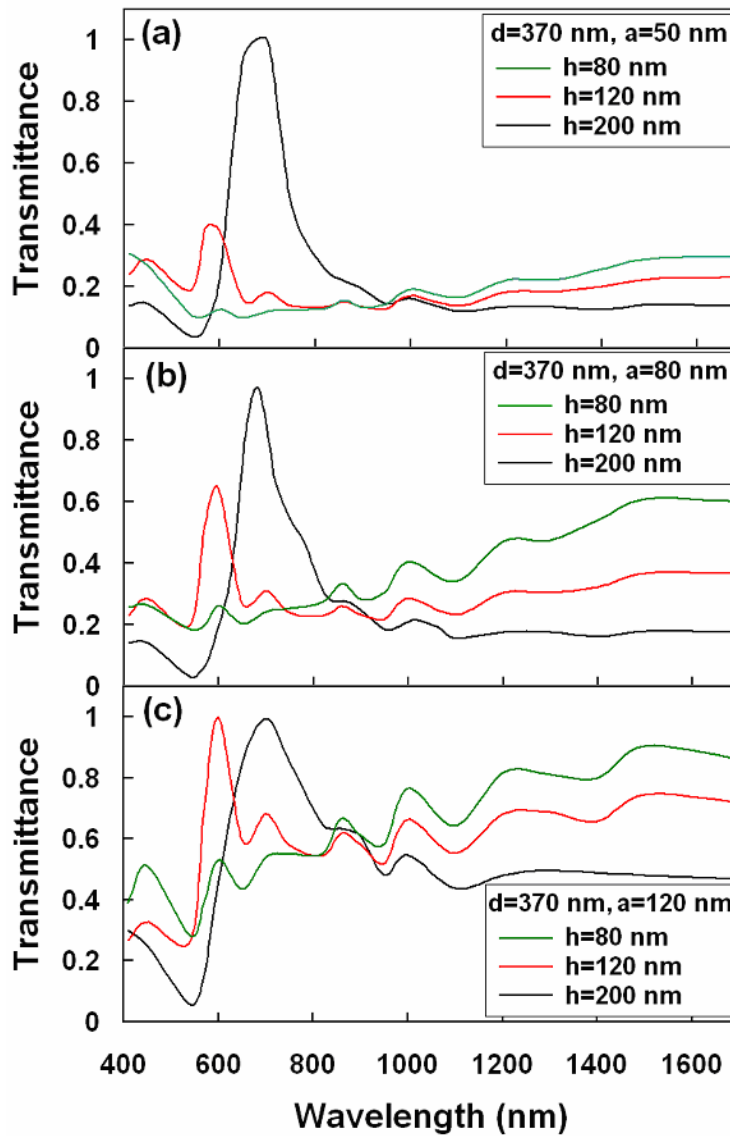


Figure 2.31. FDTD simulated transmission spectra of light through 1D narrow slits in thick silver slab. The dimensions of the structure are shown in the insets with the silver thickness (h), slit spacing (d) and slit width (a). The problem region was discretized with 551×551 mesh points; each mesh unit represents for a real dimension of 10 nm. The time step is 2000 with each spatial step corresponding to two time steps. Small fluctuations of transmittance are due to the cavity effects introduced by non-ideal absorbing boundary conditions of the problem region in simulation.

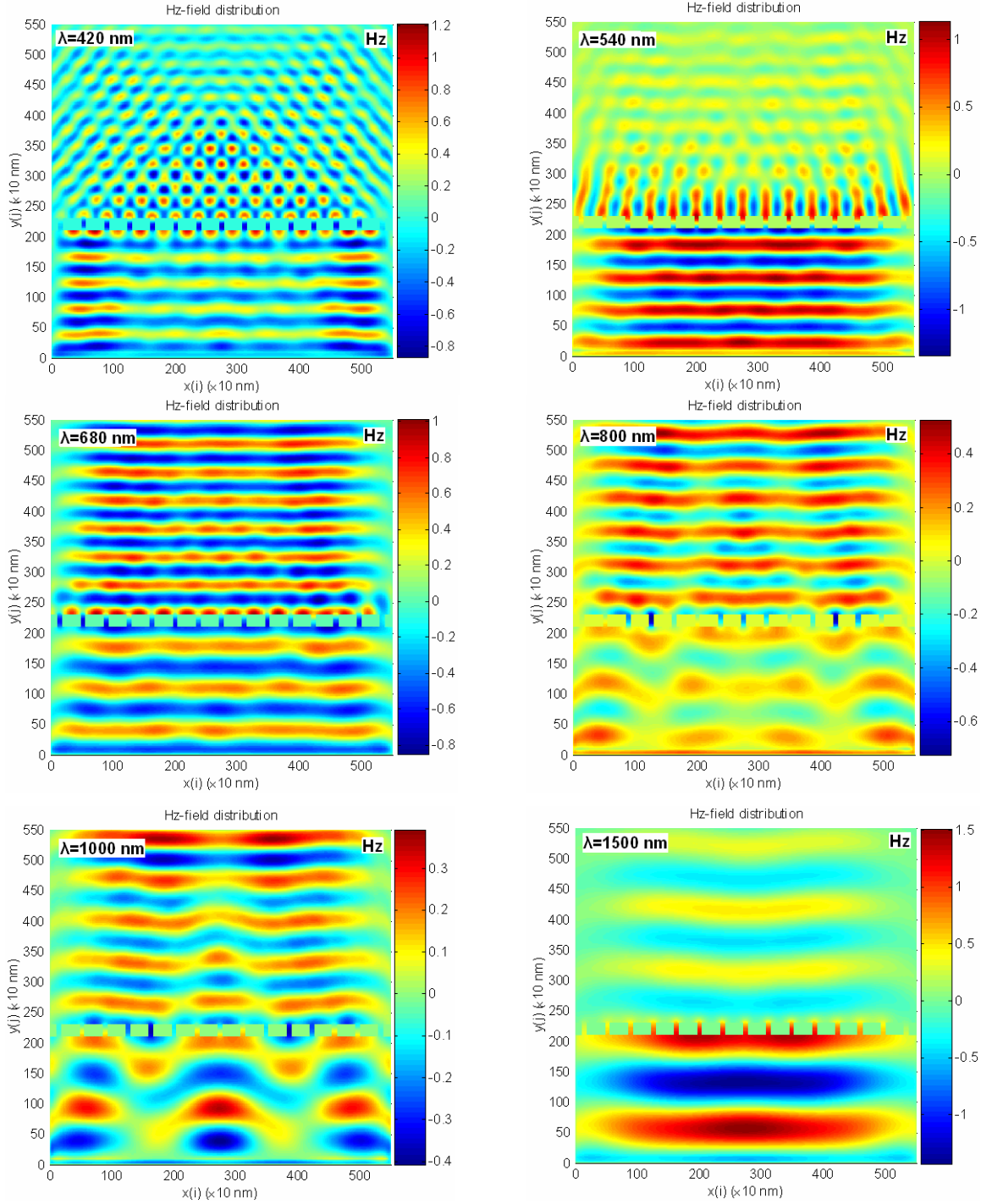
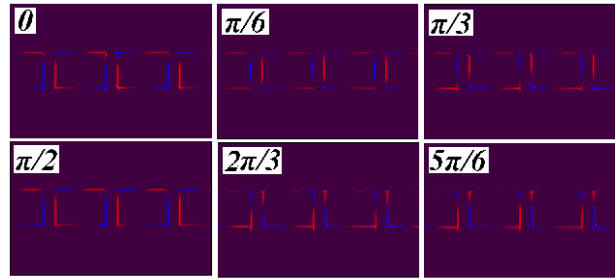
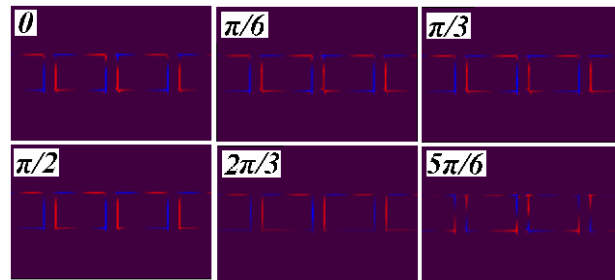


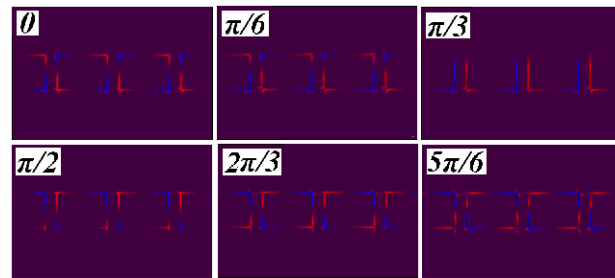
Figure 2.32. FDTD simulated Hz-field distribution at particular wavelengths. The silver structure has thickness of 200 nm, period of 370 nm, and slit width of 80 nm. On the top of silver is silica ($\epsilon = 2.16$) and below the silver is air ($\epsilon = 1$). The monochromatic waves were normally incident onto the slit arrays from air side.



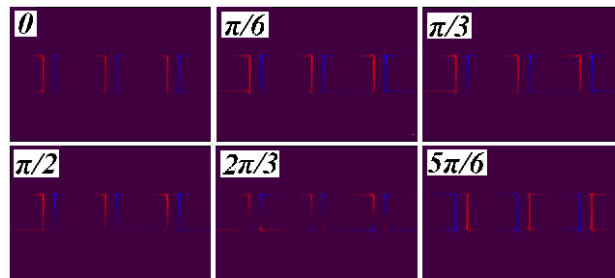
(a) $\lambda = 420 \text{ nm}$



(b) $\lambda = 540 \text{ nm}$



(c) $\lambda = 680 \text{ nm}$



(d) $\lambda = 1500 \text{ nm}$

Figure 2.33. FDTD simulated charge distribution at particular wavelengths. Charge distribution evolution are shown within $0 \sim 5\pi/6$ phase interval. (a) - (d) correspond to wavelengths of 420 nm, 540 nm, 680 nm and 1500 nm . The colors blue/red represent for the charge polarity negative/positive.

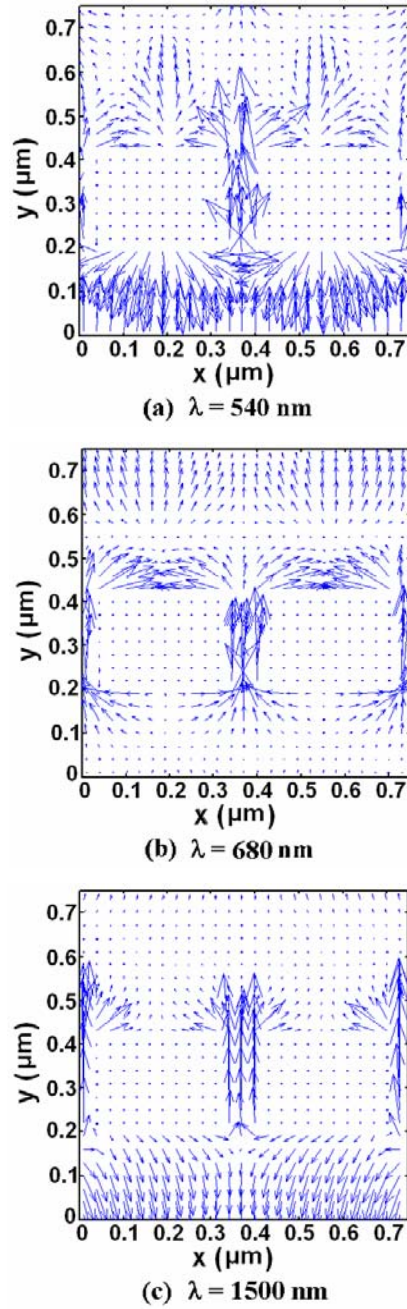


Figure 2.34. FDTD simulated instant power flow at particular wavelengths. (a) - (c) correspond to wavelengths of 540 nm, 680 nm and 1500 nm . The arrows represent direction and relative magnitude of Poynting vectors.

2.8 SUMMARY

- The optical transmission through nanoslit arrays formed in metal films was characterized and analyzed. Near full transmission of light was observed in the pass-band for TM polarization.
- Various physical effects are found to involve in this transmission phenomenon such as fundamental guided-mode transmission through the nano-slits, in-plane surface plasmon coupling by the metallic grating at both sides of metal/dielectric interfaces, dynamic polarization of the isolated grating stripes and inter-coupling between them, etc.
- Analytical and numerical analysis were performed to understand this complex phenomenon.

3.0 OPTICAL INTERACTION WITH PERIODIC METALLIC NANOSTRUCTURES

3.1 BAND-PASS TRANSMISSION OF LIGHT THROUGH 2D METALLIC NANOPORE ARRAYS

Light transmission through a thick metal slab with periodic 2D nanopore arrays exhibits extraordinary transmission efficiency as mentioned in Chapter 2. The transmission spectra show certain pass-bands, which depends on the geometry and configuration, both of the pore array and of the incident light, and the refractive index of the adjacent dielectric media [14-18]. The phenomenon offers potential applications in optical switching, optical filter and polarizer, color control in flat-panel display, near-field microscopy and photolithography [16, 17]. In the experimental work reported so far, focused ion beam etching has been used in forming the nanopores in thick metallic slabs. Although ion-beam milling shows good controllability, it is a costly process with low throughput. In this thesis, we investigated the feasibility of forming metallic nanopore arrays by utilizing the alumina nanopore arrays as a template [28].

Anodic alumina is known as a typical nanoporous material that shows a tendency to form self-organized pore arrays of triangular symmetry, and has been extensively studied, especially with bulk aluminum foils [48-52], due to their potential applications in various fields such as in electronic, photonic, magnetic, biochemical devices, etc. Highly regular arrangement of pores,

however, occurs only for a small process window, and the domain size is usually limited to a micrometer scale on bulk foils. To improve, nano-indentation and focused-ion-beam systems have been applied to prepattern the bulk aluminum foils for guiding the pore growth [53-56]. But practically, drawbacks and limitations exist for these techniques [28]. Furthermore, Alumina pore arrays grown with aluminum films that are deposited on foreign substrates (such as silicon or silica) would potentially offer flexibility and much broader applications than those on bulk aluminum foils. But anodization of aluminum films usually results in amorphous-like arrangement of pores [57, 58]. By anodizing prepatterned aluminum films, we grew large-scale highly ordered, single-domain alumina pore arrays with controlled symmetry on silica substrate [28]. We prepattern the aluminum films by evaporating aluminum onto holographically patterned photoresist (PR) gratings on silica. Both the order and symmetry of pore array were well controlled by initial periodic surface corrugations. But underlying photoresist exists causing potential problems, such as reducing the adhesion of the alumina layer to substrate and limitation for high temperature thermal processing. In this work, we further developed the method transferring the photoresist patterns onto silica substrate, so that aluminum films are deposited directly on substrate corrugations. We also found that aluminum film surface corrugations conformed from a shallow initial corrugation depth on substrate (~ 20 nm) has been enough to compensate the randomizing effect of grain boundaries in aluminum films to guide the pore growth. Under certain processing conditions, thermal annealing can be performed to improve the transparency of the as-anodized alumina films.

3.1.1 Fabrication

First, we briefly describe the process flow for the pattern transfer as illustrated in Figure 3.1. The initial one-dimensional (1D) and two-dimensional (2D) grating patterns of photoresist (PR) were defined using a holographic lithography process. The double-exposure technique for 2D grating fabrication was described elsewhere [29]. Both the period and symmetry of the gratings were controlled in process. In this work, the grating period was designed to be 350 nm. The height of 1D PR gratings is ~100 nm, and that of the thinnest ridge of 2D PR gratings is ~50 nm. The patterns were then transferred by plasma etching with a Unaxis ICP-RIE 790 system. Limited by the photoresist thickness of the grating patterns and its low selectivity to silica in etching, a transfer layer of thin Cr film was introduced on substrate, as shown in Figures 3.1(b) and (c). Cr has high selectivity to silica with $\text{CF}_4 + \text{O}_2$ gas. The etching selectivity between PR and Cr determines the maximum thickness of the Cr layer, and thereafter the maximum corrugation depth on silica substrate. A high etch ratio can be achieved for PR and silica with this transferring process. In spite of this high ratio, tolerances were usually given in determining Cr thickness and etching time for uniform transferring of patterns. Since 2D grating patterning is a delicate process, we developed a multi-step process by patterning and transferring 1D gratings twice, as shown in Figure 3.1(c). 1D PR gratings were first patterned on Cr film and the Cr layer was etched with its half depth then. The second 1D PR gratings were patterned in another direction with rotation of 60° or 90° . After another Cr etching of its half depth, areas that were etched for two times were open. A scanning electron microscope (SEM) image of as-transferred Cr mesh pattern is shown in Figure 3.2. Then the patterns can be further transferred onto substrate. It is noted that, for the uniform PR coating and grating fabrication, the first etched

corrugation depth should not be too large. With this process, an array of isolated dots was also obtained by full etching for each time.

After the pattern transfer and removal of remaining Cr mask with chemical etching, highly pure (99.999%) aluminum films (300-800 nm thick) was deposited on corrugated silica substrate using a thermal evaporation process. The corrugation profile of the substrate was conformed by the film surface. Anodic oxidation was then carried out on the as-deposited aluminum films in dilute electrolyte ($\text{H}_3\text{PO}_4 + \text{H}_2\text{O}$ in 1: 800 volume ratio) at room temperature using a Pt wire as a counter electrode. The anodization was conducted under a constant voltage (140 V) that matches the pattern period with the relation $\sim 2.5 \text{ V/nm}$. To avoid electric discharge on aluminum surface, the voltage was applied with a lower voltage ($\sim 50 \text{ V}$) at the beginning and increased to the constant voltage ($\sim 3 \text{ V/sec}$) within 30 seconds. After anodization, the samples were treated with a short-time (1- 2 min) etching in hot ($60 \text{ }^\circ\text{C}$) phosphoric acid (diluted with deionized water in 1: 3 volume ratio). Figure 3.3 shows SEM micrographs of alumina pores obtained following this process. It is shown that highly ordered, single-domain square-lattice pore arrays was obtained in a large scale. The pores grew well aligned to the concaves of the substrate patterns.

Basically, during anodization of both aluminum bulk foils and films, the pores are initiated at sites that cause nonuniform distribution of electric field on surface. Further developing of pores includes merging, overgrowing and self-reforming towards equilibrium between oxidation and dissolution for steady-state pore growth. Under constant anodic voltage, it's the pore bottom barrier oxide layer thickness and radius that affect the field distribution and

thus the oxidation and dissolution. For Al bulk foil with crystal grain size ($\sim 100 \mu\text{m}$) much larger than pore spacings, pores are self-organized statistically into triangular arrays within multi-domains ($\sim \mu\text{m}$). For thermally evaporated Al films, whose grain size ($\sim 100 \text{nm}$) is comparable or even smaller than pore cell dimensions, the pores were observed mostly likely to initiate at grain boundaries that are completely random-distributed. And pores are developed without any order in any scale. With prepatterned periodic corrugations on Al film surfaces, the pores are guided to locate at sites of concaves. Since the corrugation period matches condition for the equilibrium of steady-state pore growth, further development do not rearrange the pores. It should be noted that pores were also initiated at the grain boundaries, but their effects were fully compensated by prepatterned corrugations and cannot be developed into deep pores. To guide the pore growth, the corrugation should be deep enough to compensate any randomizing effects and also be able to arrange the pores into controlled order and symmetry that is even not favorable to spontaneous self-assembly dynamics. In experiment, a depth of $\sim 20 \text{nm}$ substrate corrugation was shown to be enough to guide the growth of 350nm period square-lattice pore arrays with 400nm -thick Al film. With our usual corrugation depth of $50\text{--}100 \text{nm}$, 800nm Al films were deposited without any obvious degradation of surface morphology. (Further increase of film thickness was limited by our evaporation source capacity.) And the pores were well guided during growth. It appeared that, although the transferred corrugation had irregular shape and varying size, the as-processed pores had rather uniform size and symmetry-dependent shape.

Usually, the anodized alumina films appear greenish/violet. To improve its optical transparency, we carried out annealing of the samples in oxygen ambient so as to oxidize remaining aluminum, reduce contained OH^- anions and oxygen vacancies that act as light

absorbing centers. It was found that fine cracks were generated at temperatures above 600 °C due to mismatch of thermal expansion coefficients of anodic alumina and silica substrate. While below 800 °C, the visible light transparency of the films was not apparently improved. Cracks were avoided by increasing and decreasing temperatures slowly before and after annealing at 800 °C. Especially between 600 and 800 °C, temperature was ramped up and down at a rate of 2 °C/min.

Afterwards, a thick layer (> 200 nm) of silver was deposited on the porous anodic alumina template. As shown in Figure 2.3 previously, if the sample is mounted normally right to the evaporation source, the silver will be deposited both on top of the ridges and bottom of the pores; if the sample is mounted obliquely tilted to the source, the silver film is only deposited on the top of the ridges. The top-view SEM micrographs of the as-prepared silver pore arrays are shown in Figure 3.4 for both cases.

3.1.2 Characterization and Discussion

The zero-order transmission spectra were characterized with the same setup as shown Figure 2.4(a). The spectrum is shown in Figure 3.5 for the sample with its silver layer deposited obliquely. The spectrum for the sample with silver deposited normally cannot be well resolved due to weak signal that emerged with noise. It can be seen that the spectrum (Figure 3.5) shows a clear pass-band with three peaks at wavelengths around 700 nm, 600 nm and 450 nm. Transmittance is somewhat low, around 1.5 % for maximum, compared to that, around 5 ~ 15%,

obtained by utilizing advanced ion-beam etching techniques [14, 15, 31]. This discrepancy is ascribed to inaccuracy on characterization and calculation of the transmissivity; another also very important reason is the strong diffusive scattering due to the rough granular metal layer as shown in Figure 3.4. The number that we observed, however, is higher than that, $\sim (d/\lambda)^4$, expected from Bethe's theory [13].

As mentioned in Chapter 2, optical transmission property of subwavelength holes is different from that of subwavelength slits. There exists a cutoff frequency (or wavelength) for EM wave propagation mode inside the small holes [33], i.e. the evanescent component of the wave vector inside slit dominates the propagation component. Thus, unlike the slit case, the transmission through holes is highly attenuating at long wavelengths due to the cutoff restriction. At shorter wavelengths, the wave mode inside a slit transits to be propagation dominant. Since the hole size is much smaller than the wavelength dimension, there is no matching of the light momentum and mode momentum for coupling; by excitation of local surface plasmons by hole edges, the plasmons with higher momentum can be coupled with the propagation mode inside slit and perform power transmission. For such plasmon modes, the fields are highly "squeezed" inside holes and coupled with the harmonic electron oscillation at metal surfaces such that the electron entity involves in energy transportation, which is different from EM energy transmitting in free space or dielectric media. At shorter wavelengths, the plasmon modes should still be supported; the reduced transmission is due to the densely packed higher order coupling of incidence light and coupled plasmon wave inside hole with in-plane surface plasmon modes at the top (Ag/air) and bottom (Ag/anodic-alumina) interfaces of the Ag layer. The mode position is basically determined by [15]

$$\lambda_0 = \frac{d}{\sqrt{i^2 + j^2}} \sqrt{\frac{\varepsilon_m \varepsilon_d}{\varepsilon_m + \varepsilon_d}}, \quad (3.1)$$

where d is the hole square lattice constant, ε_m and ε_d are dielectric constants of the metal and adjacent dielectric media; i and j are integers denoting the coupling order in two directions of the square lattice. Due to the small structure dimensions relative to the wavelengths in the range, the spectrum features at short wavelengths cannot be well distinguished. But the main transmission peak position is certainly at longer wavelengths than that for the lowest order in-plane SP modes.

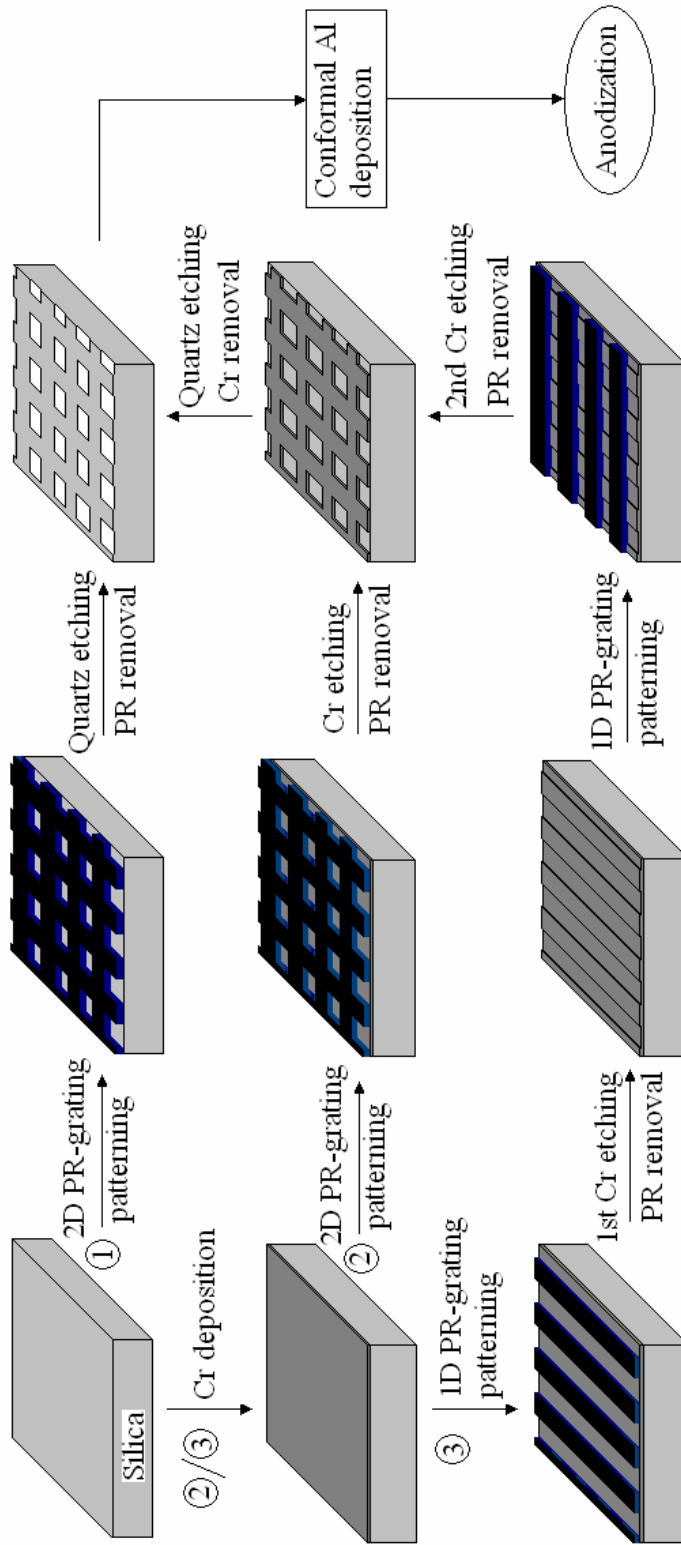


Figure 3.1. Schematic illustration of procedures transferring holographic photoresist grating patterns onto substrate. Three ways: (a) directly transferring 2D PR-grating patterns onto substrate; (b) Using a Cr layer as a sacrifice layer transferring 2D PR-grating patterns onto substrate; (c) Using a multiple 1D grating patterning process transferring 2D grating patterns onto substrate.

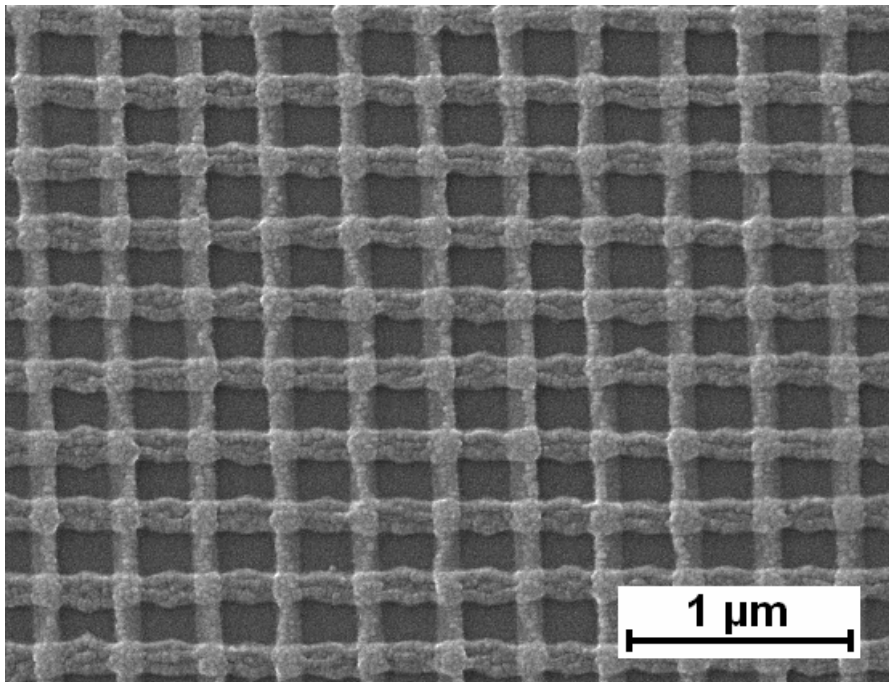


Figure 3.2. SEM micrographs of Cr mesh patterns on silica substrate obtained with the two-step 1D grating fabrication process. The initial Cr thickness is 50 nm.

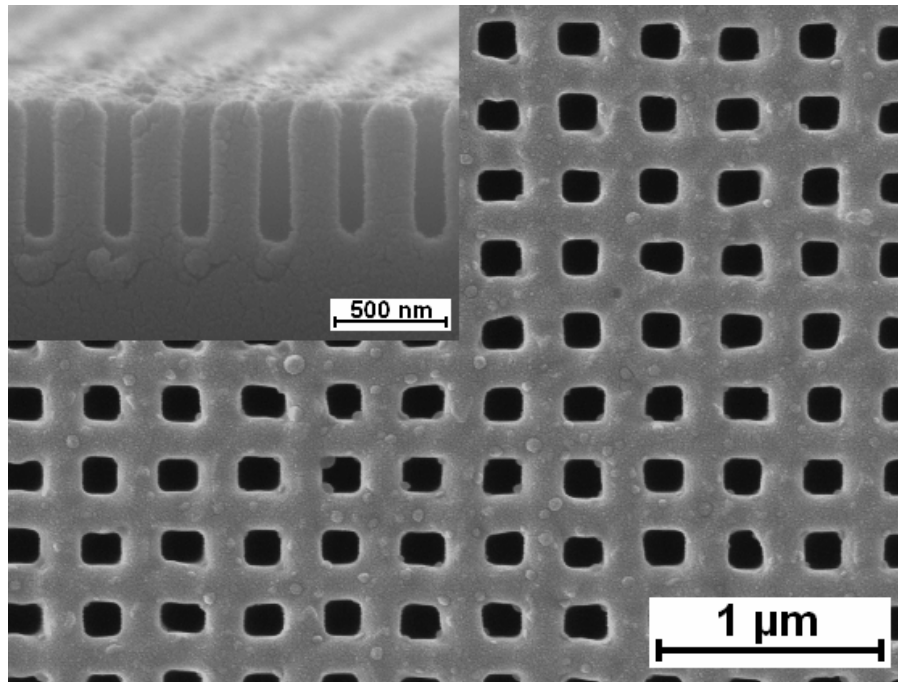
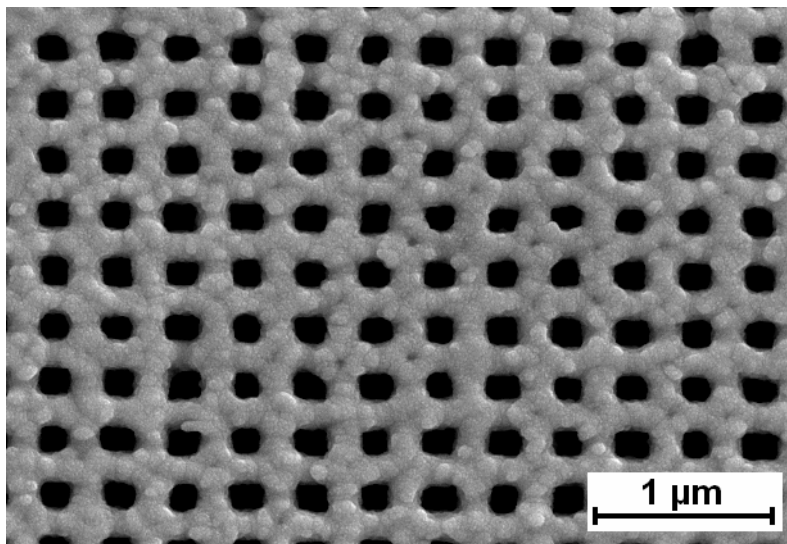
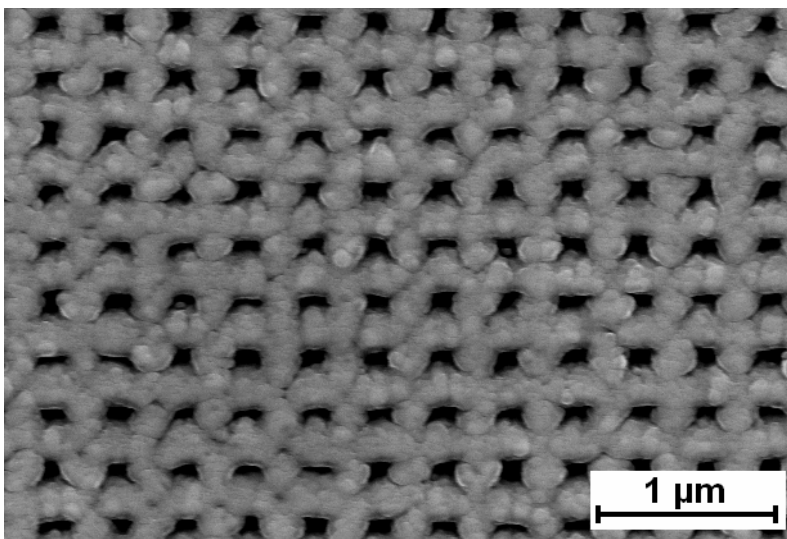


Figure 3.3. SEM micrographs of anodic alumina pore arrays on silica substrates. Top-view image (a) showing square-lattice arrangement of square-shaped pores. (b) Cross-sectional image showing that the pores grew well aligned to the center of the corrugation bottoms. The Cr mask for pattern transfer was obtained from the two-step 1D-grating patterning process. The transferred substrate corrugation can be seen in the cross-sectional image (b). The initial deposited aluminum film was 350 nm thick and anodized at 140 V for 40 min.



(a)



(b)

Figure 3.4. SEM micrographs of silver pore arrays formed on porous anodic alumina template. The silver film of thickness ~ 200 nm was deposited onto the template (a) normally, and (b) obliquely tilted with an angle of 45 degrees.

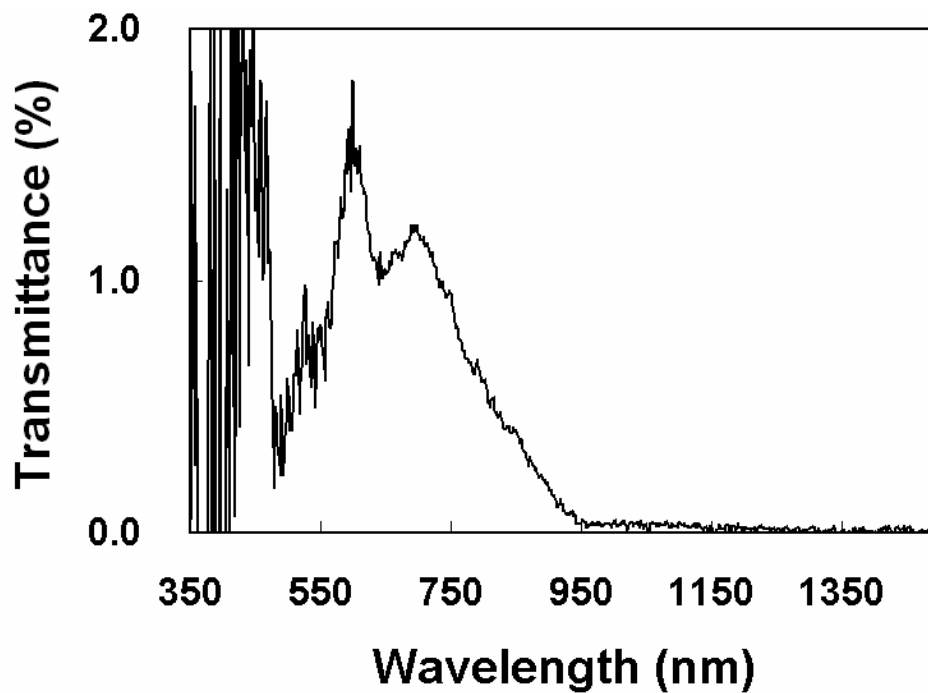


Figure 3.5. Transmission spectrum of 2D square lattice silver nanopore arrays formed on porous anodic alumina template. The silver on the sample was deposited obliquely.

3.2 OPTICAL TRANSMISSION THROUGH BI-LAYER 1D NARROW METALLIC SLIT ARRAYS

3.2.1 Fabrication and Characterization

The 1D narrow slit arrays were fabricated with the same techniques as described in Section 2.2.

Then, a bi-layer structure was formed by stacking two single-layer 1D slit samples with the metal sides facing each other. The two metal faces were separated by photoresist ($<3 \mu\text{m}$) or a plastic film of known thickness cushioned out of the grating areas and thus the actual medium between metal films in grating area is air. The cross angle between the two gratings was also varied in the range of 0° to 90° . The configuration is schematically shown in Figure 3.6.

The zero-order transmission was also characterized with the same set-up as shown in Figure 2.4(a). The transmission was normalized with that of the same configuration but without silver layers.

3.2.2 Results and Discussion

1. Single-layer vs. Bi-layer Structures

Two pieces of a 1D slit array sample were configured with a separation of $\sim 10 \mu\text{m}$, and same grating directions (i.e. $\varphi = 0^\circ$). The silver grating layer has a thickness of 240 nm, period of 780 nm and slit width of 50~150 nm along the slit depth. The transmission was characterized and compared with that of a single-layer (one half). The results are shown in Figure 3.7. It is noted that slits of the two layers were not controlled to be in alignment laterally. Considering the separation ($\sim 10 \mu\text{m}$) being in a far-field regime, the lateral alignment is not expected to have any effect on the transmission.

It is seen from the figure that (1) the two spectra have similar features, and positions of the main pass-bands did not shift; (2) the transmittance at the main pass-band does not change much for the bi-layer configuration; (3) the transmittance at side-lobes is strongly reduced; and (4) Fabry-Perot-like cavity resonance is observed at longer wavelengths.

A further inspection shows that, within the experimental errors, $T_{2L} \approx T_{1L}$ at the main pass-band with T_{2L} and T_{1L} denoting the transmittance of the bi-layer and single-layer samples; while $T_{2L} \approx T_{1L}^2$ at the side lobes. Since the incident beam is unpolarized, if we scale the transmittance by a factor of 2 for only TM-polarized component to be considered, there would be a relation of $T_{2L}^{TM} \approx T_{1L}^{TM^2}$ in all the wavelength range. This is another indication of the strong polarization of the 1D thick metallic grating slit arrays, and a nearly full transmission of the TM-polarized light at the main peak wavelength.

It also suggests that, although light is localized and nonuniform in near field (close to the metallic grating surface), the light is nearly uniform plane waves in far field (at 10 μm away). The transmission is not dependent of mutual alignment of the grating lines of the two samples, but only on wavelength (or frequency) and polarization.

The transmission oscillations at long wavelengths were confirmed due to Fabry-Perot cavity resonance by consistence of the peak spacings with the resonance conditions, i.e.

$$\Delta\left(\frac{1}{\lambda}\right) = \frac{1}{2nh}, \quad (3.2)$$

where n is the index of the medium between the two layers, h is the separation of the two layers and λ is the corresponding wavelength in vacuum. It suggests the normal transmission is strongly limited by normal reflection at long wavelengths. While at shorter wavelengths, the resonance is not apparent mostly due to the much denser peak spacings and the large transmission in the main pass band, which weakens Fabry-Perot resonance.

Overall, the band pass characteristics of transmission spectrum are improved by the bi-layer structure, which strongly suppresses the side transmission lobes while maintaining good transmission in the main pass-band.

2. Transmission Modulation by Varying the Crossing Angle

We used the sample same as that in Figure 3.7, and characterized the transmission at different cross angles 0° , 45° and 90° . The results are shown in Figure 3.8.

It is seen that the transmission in the pass bands are maximum at 0° cross-angle and almost zero at 90° . Again, by considering the unpolarized nature of the incident beam and thus by scaling the transmission by a factor of 2 for TM-polarization incidence on the first impinged layer, the transmission follows the similar principle as Malus's law:

$$T_{2L}(\lambda) \approx T_{1L}^2(\lambda) \cdot \cos^2 \varphi, \quad (3.3)$$

where $T_{2L}(\lambda)$ is the total transmission of a bi-layer sample for incidence of TM-polarized light with respect to the first impinged gratings, T_{1L} is the transmission of a single-layer sample for TM-polarized incidence.

Comparing the transmission spectra for different cross-angles, it is obvious that there is almost no Fabry-Perot (F-P) resonance for 0° at the main pass band, but there is for 45° and 90° . For the 0° case, after the first layer polarization, the beam can be almost fully transmitted by both layers, thus FP resonance cannot be formed. For 45° case, after the first layer polarization, the second layer is partially transmission, i.e. the TM component will fully be transmitted but the TE component will be bounced back; again the bounced beam will be decomposed into TM and TE components impinging on the first layer, and it will also be partially transmission / reflection.

Thus a FP resonance is formed. The reflectivity (R) and transmissivity (T) of the two layers for the cavity resonance can be approximated with

$$R = \sin \varphi , \quad T = \cos \varphi . \quad (3.4)$$

Note that the relations are based on an assumption that the degree of polarization for a single layer transmission is nearly 100 %. The transmitted and reflected beams are all polarized in the grating directions of the first layer and second layer. Thus, Equation (3.3) is the transmittance of such a F-P cavity under zero-order approximation.

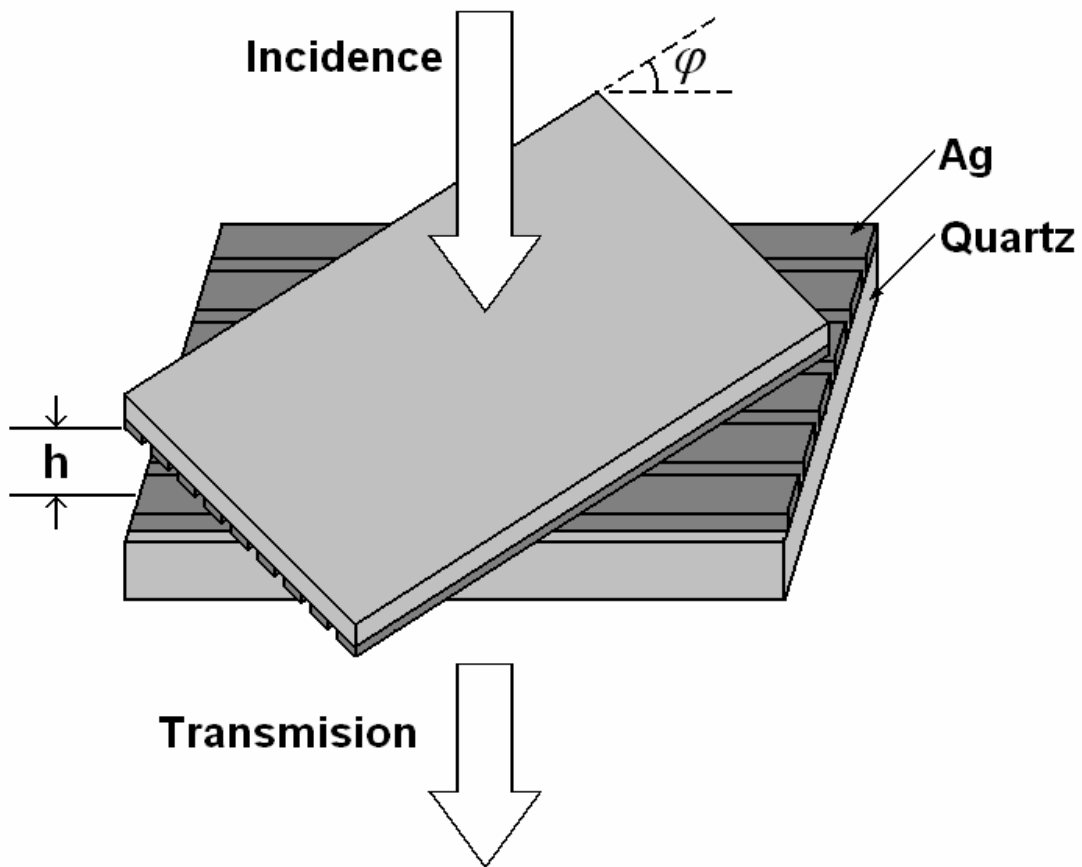


Figure 3.6. Schematic diagram of the configuration of the bi-layer 1D narrow metallic grating slits. The two layers are separated by air with a distance of h ; cross-angle of the gratings is φ .

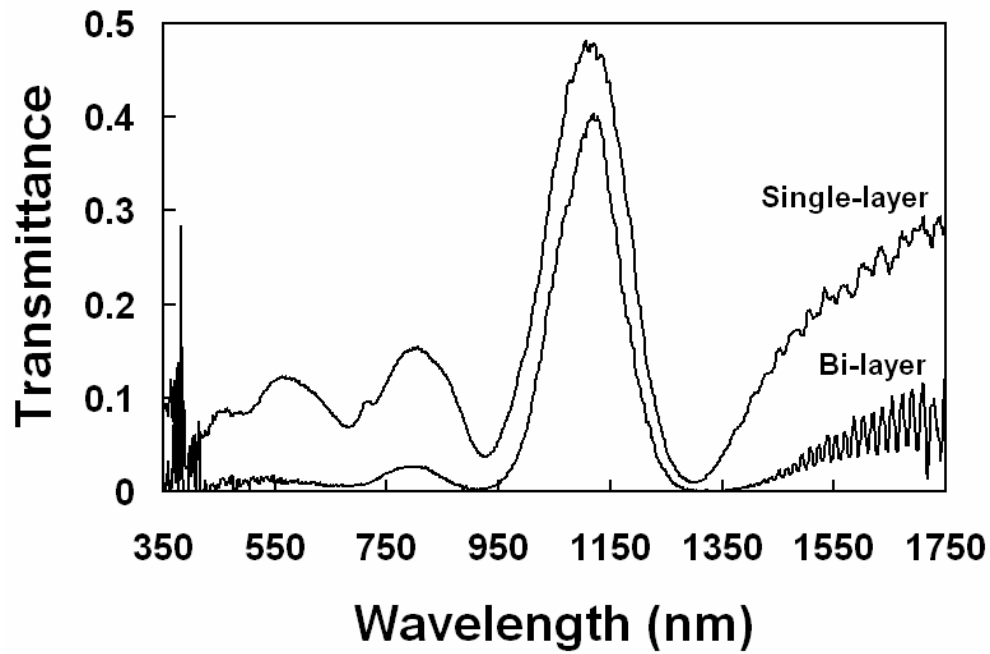


Figure 3.7. Comparison of transmission spectra of a bi-layer metallic grating slit array and a single-layer one. The metallic grating period is 780 nm. The silver layer thickness is 240 nm. The slit width is ranging in 50 ~ 150 nm along the slit depth. Separation of the two layers is ~ 10 μm . The incidence beam is unpolarized.

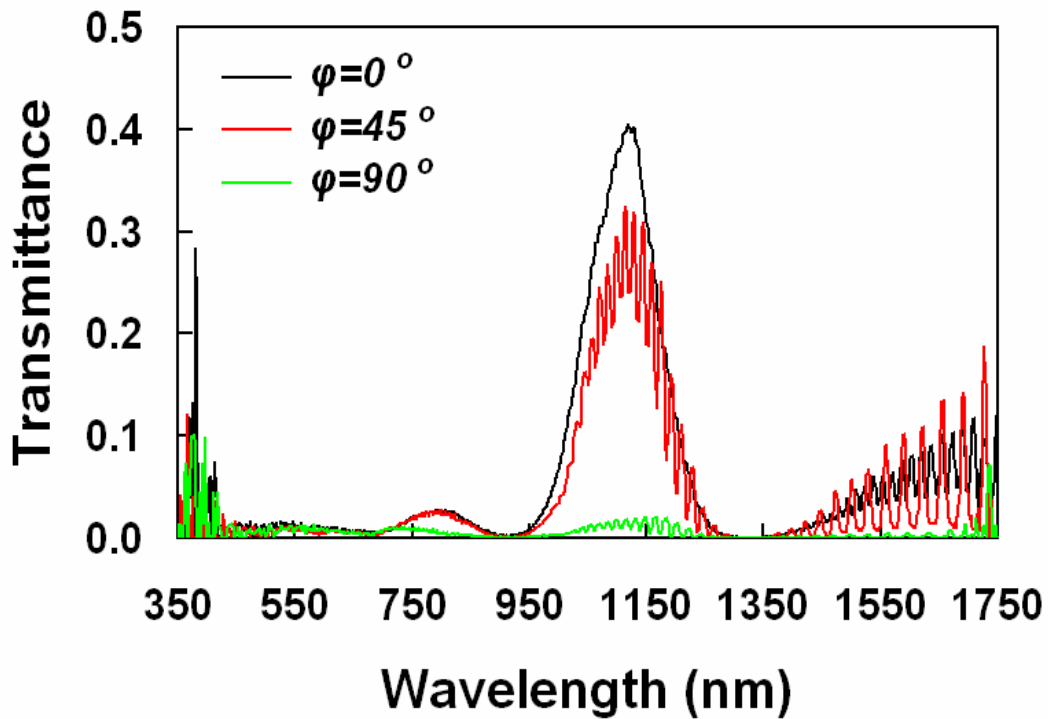


Figure 3.8. Transmission modulation by varying the cross angle of the gratings on a bi-layer metallic narrow slit arrays. The metallic grating period is 780 nm. The silver layer thickness is 240 nm. The slit width is ranging in 50 ~ 150 nm along the slit depth. Separation of the two layers is ~ 10 μm . The incidence beam is unpolarized. Cross-angle of the gratings on two layers were varied for 0° (black), 45° (red) and 90° (green).

3.2.3 FDTD Simulation of Near-field Interaction between Bi-layer Slit Arrays

We experimentally investigated the transmission characteristics of bi-layer metallic narrow slit arrays and modeled with a special Fabry-Perot resonator. As the layers are far separated, the phase shifts at each reflection interfaces can be neglected, which is much smaller than the internal optical path phase accumulation. Thus the resonance peak intervals can be estimated with Equation (3.2), but not the exact peak positions, which require knowledge of interface phase shifts. Suppose the two layers are stacked close enough to each other, we can have only a few resonance peaks within the visible and near infrared wavelength range. A narrower transmission pass-band is expected if one of the F-P peaks located inside the main transmission pass-band of the metallic narrow slit arrays; and, by eliminating or strongly suppressing other F-P peaks with corresponding low transmissions, we may realize single F-P pass-band within the spectrum range of interest with this assembly. So far, it has been difficult to realize precisely controlled separation of the bi-layer structures in experiments. In this section, a FDTD simulation analysis is performed for a primary investigation of this case. In the simulations, the TM polarized light was incident on the slit arrays and slit line directions are in parallel for the bi-layer case. Here, all the dielectric regions were assumed to be air and the index of silver was applied for metal.

1. Simulated Transmission of Single-layer Metal Slit Arrays with Different Periods

Using FDTD method, the field distribution was calculated for the transmission problem, and the transmittance was calculated by averaging the integrated light intensities in far-field

region. As shown in Figure 3.9, the main pass-band peak shifts to longer wavelengths with the increase of slit array periods. The field and charge distributions at the main transmission peaks show characteristics of resonant quadrupole polarizations of each silver island. The high transmission is resulted from coupling of the surface plasmon wave mode with the resonant quadrupole polarization. The peak position can be roughly estimated with

$$\sum_i n_i \left(\frac{2\pi}{\lambda_0} \right) \cdot L_i + \Delta\varphi = m(2\pi), \quad m = 2 \text{ for quadrupole.} \quad (3.5)$$

where n_i is the effective index for surface plasmons at each island surface segment, and L_i the length of each surface segment around the periphery of metal island; λ_0 is the free space wavelength.; $\Delta\varphi$ is the phase retardation introduced by shape anisotropy (or scattering at sharp corners) and/or scattering due to other surface defects. Take $\Delta\varphi = 0$, the peak position can be estimated with $\lambda_0 = \frac{1}{2} \sum_i n_i L_i$. The model is consistent quite well with simulation and experimental results.

2. Bi-layers Composed of Metal Slit Arrays with Different Periods

Motivated by narrowing the transmission pass-band by superposing closely located pass-bands of individual layers, bi-layer metal slit arrays with different periods are assembled and investigated. The FDTD simulated transmission spectra of two assemblies are plotted in Figure 3.10 (a) and (b).

Generally, the simulation indicates that the as-resulted transmission spectra are explicitly multiplication of two individual spectra. The bi-layer transmission spectrum for smaller period difference (Figure 3.10 (a)) shows apparent narrower pass-band. But as the period difference is much larger (Figure 3.10 (b)), the bi-layer transmittance within the pass-band is much lowered; this results actually no effective narrowing of the pass-band evaluated with full-width-half-maximum (FWHM).

An obvious improvement of the transmission spectrum for filtering is the dramatic suppression of the transmission outside of the pass-band for both cases.

3. Effects of Bi-layer Separation on Transmission Spectrum

Figure 3.11 shows a set of bi-layer transmission spectra obtained with FDTD simulation for different layer separations but with same period of 370 nm. It's identified that two types of transmission peaks are resulted. One is mainly due to the high transmission of single layer, which locates at ~ 600 nm wavelength for all cases; the others are due to Fabry-Perot resonances. There seems to be no confusion as for separation of $0.2 \mu\text{m}$ and $0.5 \mu\text{m}$, which do not have F-P resonance peaks around 600 nm wavelength, the main pass-band peak of the single layer structure. But for bi-layers with separation of $0.3 \mu\text{m}$ and $0.6 \mu\text{m}$, which have F-P resonance peaks at 600 nm wavelength, two side peaks appear at shifted shorter and longer wavelengths around 600 nm. And the F-P resonance peak at long wavelength also blue-shift from 1200 nm.

Then, the bi-layer structures are modeled with F-P resonance by applying the numerically simulated transmittance of a single layer structure and assuming a zero phase shift at the internal air / Ag-slit-array-layer interfaces. The internal reflectance is assumed to be complementary to the transmittance and both are also multiplied with factors considering certain absorption. The results are as shown in Figure 3.12 (a), (b) and (c) for bi-layer separation of 0.3, 0.5 and 0.6 μm . Without considering the sharpness of the peaks, the one for 0.5 μm separation (b) is consistent with the FDTD simulated transmission spectrum quite well, but for those with separation of 0.3 and 0.6 μm it doesn't give indication of the side peaks around 600 nm wavelength. Then further investigation shows that, if wavelength-dependent phase shifts are considered for internal reflections of the resonance, features of the FDTD simulation transmission spectra can be well reproduced as shown in Figure 3.12 (d), (e) and (f). A negative phase shift at wavelengths smaller than 600 nm and a positive phase shift at wavelengths larger than 600 nm have the resonance conditions (phase matching) also satisfied at their positions, while they have the same resonance order as that at 600 nm wavelength. Such wavelength dependent phase shifts have been clearly observed in FDTD simulation for transmission, which is mainly induced by scattering interaction of light with the metallic nanostructures instead of material absorption. The phase shift effects are prominent especially for the low order resonance.

4. Effects of Lateral Shifts on Bi-layer Transmission

As the two layers are separated in far field, there is certainly no direct interaction between their near-field field distributions; between them are plane waves, and the lateral shift is not concerned. Using FDTD method, we simulated the situation for effects of lateral shift on near-

field interactions. The as-analyzed transmission spectra are shown in Figure 3.13, which compared the cases for two layers being aligned, quarter-period-misaligned and half-period-misaligned. Basically, only a slight difference is observed. For identical two layers, it suggests still better to have them aligned for narrower main pass-band and low side transmission. This should be advantageous in future experimental realization with integrated fabrication methods.

Figure 3.14 further shows the Hz-field distributions for misaligned bi-layers under a separation of 200 nm. Periods of both layers are same for (a), (b) and (c), and slightly different for (d). In (a), (b) and (c), between the two layers is just periodic lateral variation of the field with the pitch of the slit arrays. It's observed that the islands of each slit array is "bonded" to the one of the other layer with the nearest path. And strong phase retardation between the two layers is expected for transmission. This situation resembles the interface of epitaxial layers "strained" with a lamination fault. For slit arrays with different periods in (d), there appear asymmetric bonds and local "defects" are induced to compensate the mismatch.

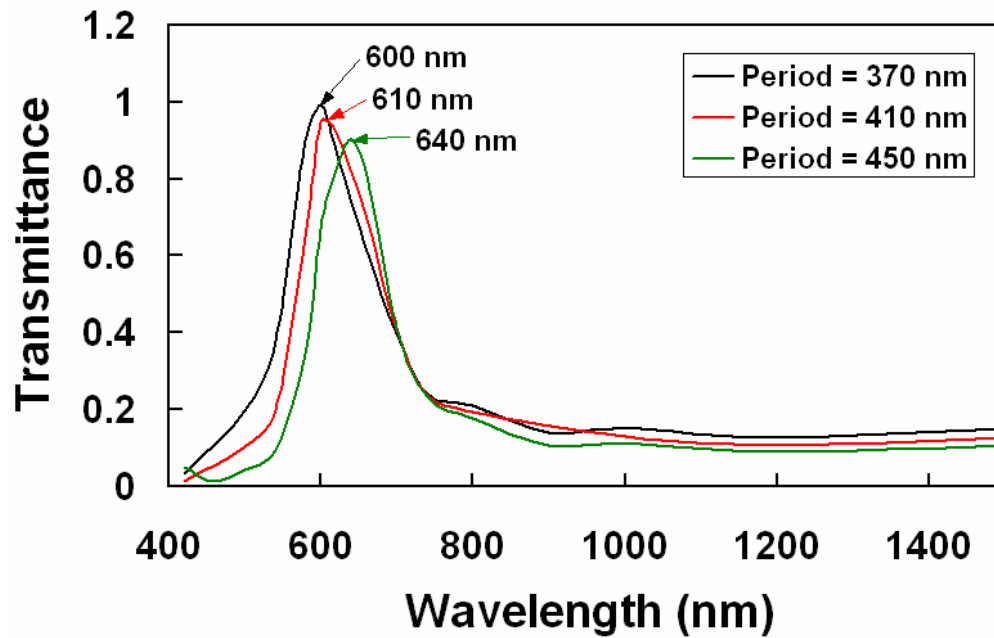
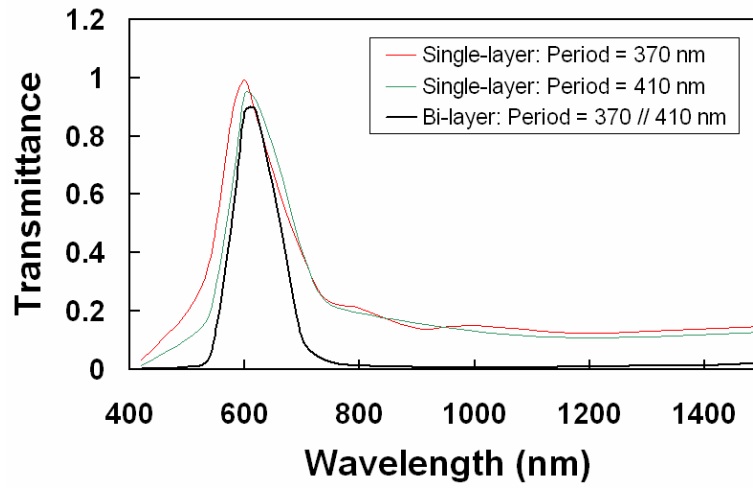
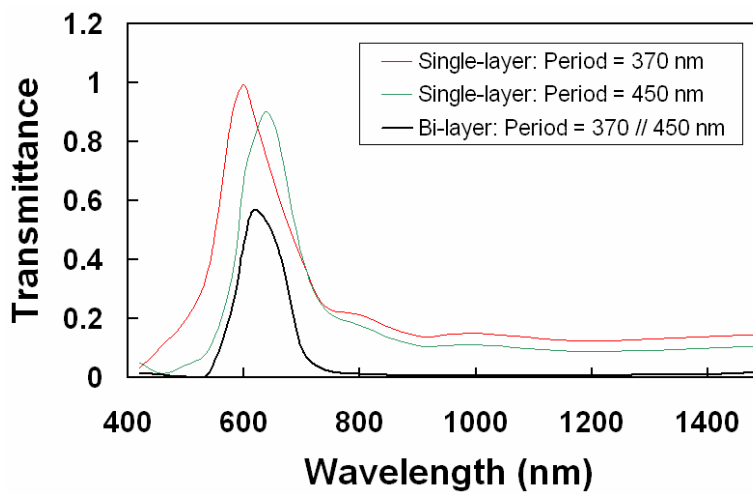


Figure 3.9. FDTD simulated transmission of light through single layer of silver films with narrow slit arrays of different periods. The dielectric background of the metallic structure is assumed to be air. The silver layer thickness (200 nm) and slit width (80 nm) are all the same.



(a)



(b)

Figure 3.10. FDTD simulated transmission of light through bi-layer of silver films with narrow slit arrays of different periods. The dielectric background of the metallic structures is assumed to be air. The silver layer thickness (200 nm) and slit width (80 nm) are all the same for each layer. The separation of bi-layers for (a) and (b) are both 200 nm.

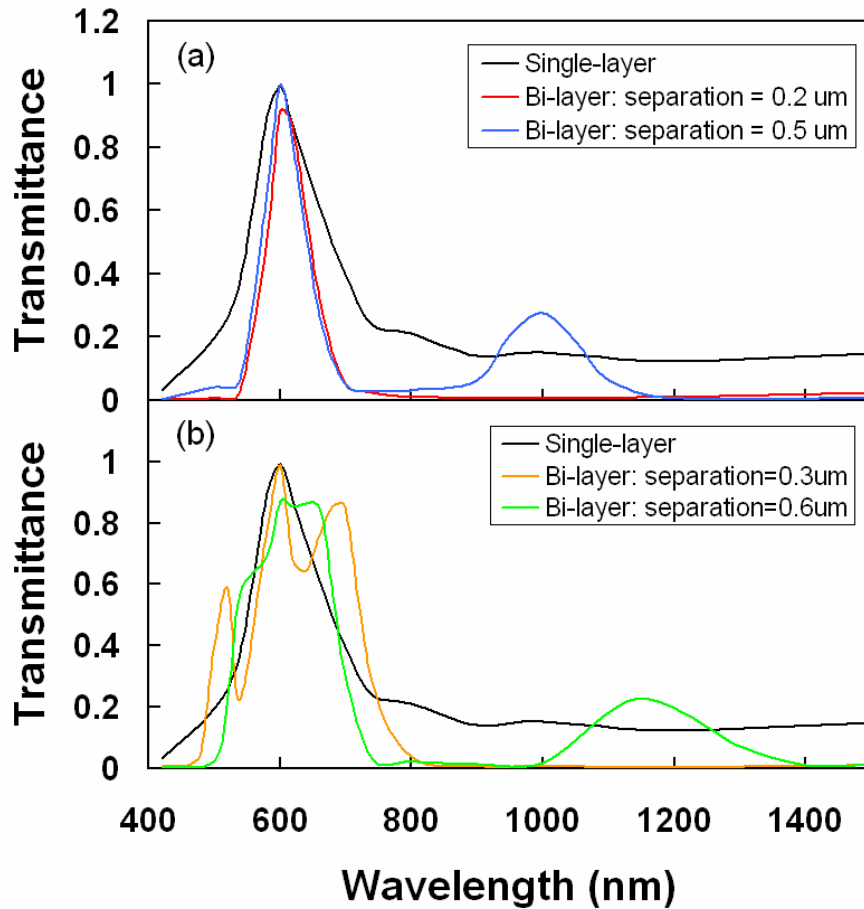


Figure 3.11. FDTD simulated transmission of light through bi-layer of silver films with narrow slit arrays at different layer separations. The dielectric background of the metallic structures is assumed to be air. The silver layer thickness (200 nm), slit array period (370 nm) and slit width (80 nm) are the same for all layers. The separations vary at 0.2, 0.3, 0.5 and 0.6 μm .

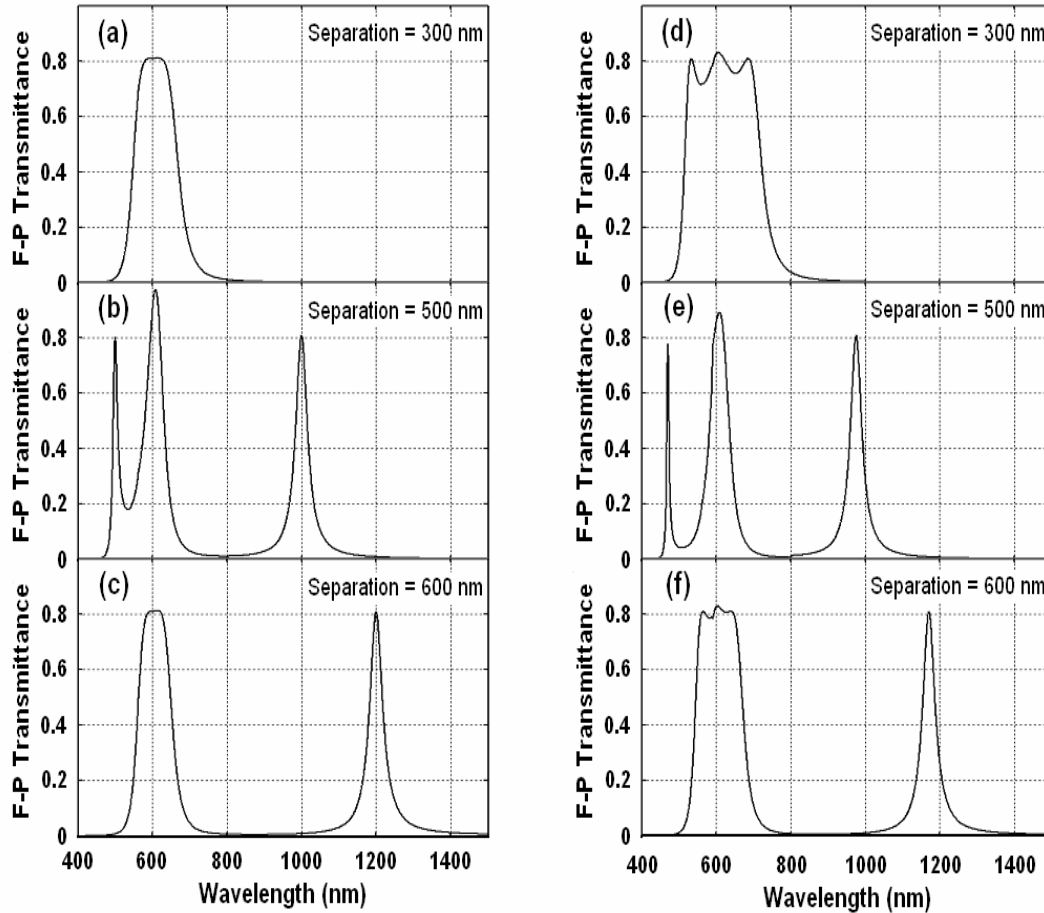


Figure 3.12. Transmission of bi-layer metallic narrow slit arrays modeled with Fabry-Perot cavity modes. The transmission of each layer has property of filtering characteristics. And the internal reflection has strong wavelength-dependent phase shifts at interfaces. The dielectric background of the metallic structures is assumed to be air. The silver layer thickness (200 nm), slit array period (370 nm) and slit width (80 nm) are the same for all layers. The separations vary as indicated. In modeling, for the reflection phase shift, $-\pi/4$ was taken below 600 nm wavelength, 0 at 600 nm, $+\pi/4$ between 600 and 800 nm, and $-\pi/20$ above 800 nm.

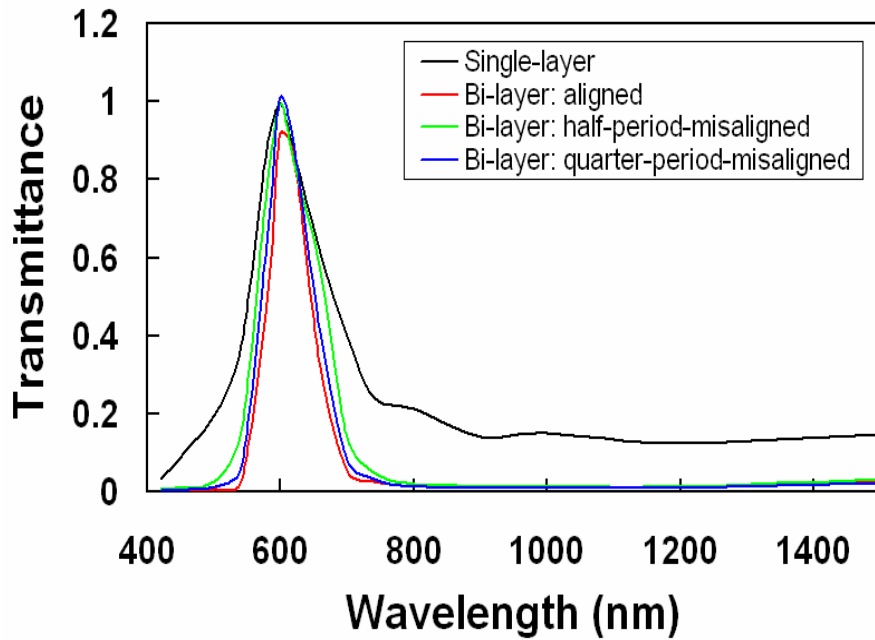


Figure 3.13. Effects of lateral shifts on transmission of bi-layer silver narrow slit arrays simulated with FDTD method. The dielectric background of the metallic structures is assumed to be air. The silver layer thickness (200 nm), slit array period (370 nm), slit width (80 nm) and separation (200 nm) are the same for all layers. The two layers are misaligned with shifts of a half period and a quarter period.

Bi-layer separation: 200 nm

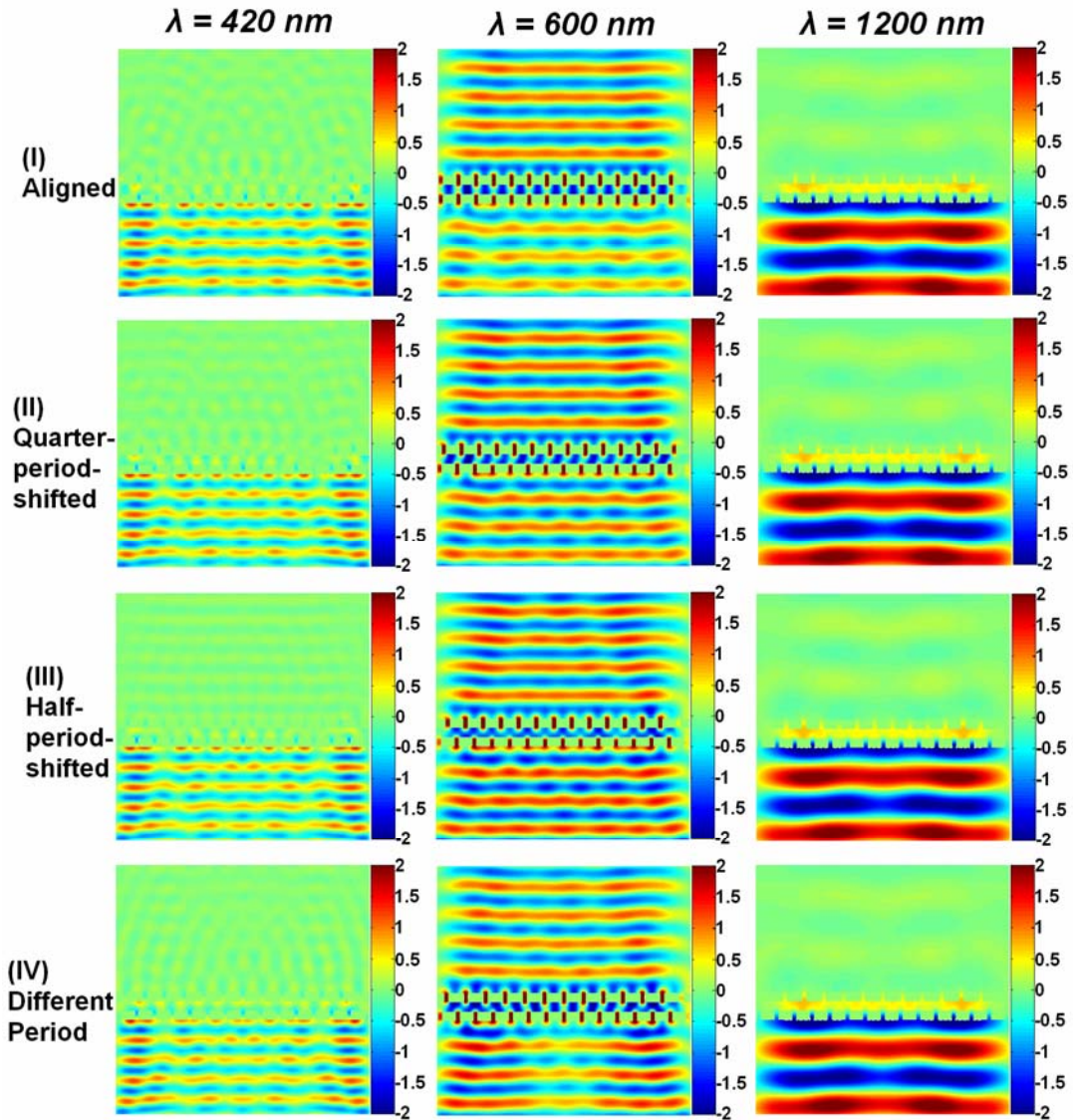


Figure 3.14. Hz-field distribution in transmission of light through bi-layer of silver narrow slit arrays under different alignment simulated with FDTD method. The dielectric background is assumed to be air. For (a), (b) and (c), the silver layer thickness (200 nm), slit array period (370 nm), slit width (80 nm) and separation (200 nm) are the same for all layers. The two layers are misaligned with shifts of a half period and a quarter period. For (d), the periods of two layers are different (370 nm vs. 410 nm).

3.3 REFLECTION QUENCHING OF 1D METALLIC GRATINGS

3.3.1 Fabrication and Characterization

The techniques used for fabrication of the 1D reflective gratings with subwavelength period are similar to that described earlier. First, grating grooves were formed on silica substrate by transferring the holographic photoresist gratings. The grating depth was varied between 30 ~ 120 nm. Then, a silver layer was deposited onto the silica gratings with thickness varying between 40 ~ 180 nm. Since the silver deposition is nearly a conformal process, the grating depth can be adjusted by varying the transferred substrate grating depth. A schematic drawing of the structure is shown in Figure 3.15.

The angular dependent zero-order reflection and transmission (through tunneling) were characterized with TM-polarized incidence at the fixed wavelength (633 nm) with the setup shown in Figure 2.4(b).

3.3.2 Results and Discussion

The zero-order TM reflection and transmission of two grating samples with same period but different depth were characterized. The periods for both are 370 nm. One has the grating depth of 30 nm and deposited silver thickness of 40 nm; the other has the grating depth of 120 nm and deposited silver thickness of 170 nm. The measured spectra are shown in Figures 3.16 (a) and (b).

It is obviously seen that (1) both of the reflection spectra show reflection peaks at 45° ; (2) there is a sharp reflection quenching dip at 42° for the shallower one, but not for the deeper one; (3) overall, the reflectance at smaller angles are larger than those at larger angles for each of the samples; (4) the overall reflectance of the shallower gratings at non-peak/dip angles are larger than that of the deeper gratings; (5) general trends of the angle dependent transmission spectra are complementary to the reflection spectra for both samples, and the transmittance is rather low due to strong absorption in tunneling transmission.

In analysis of interaction of light with the metallic gratings, the following processes need to be considered: (1) grating diffraction coupling, i.e. photon-photon coupling; (2) coupling of propagating light into metal surface plasmon waves, i.e. photon-plasmon coupling; (3) decoupling of metal surface plasmon waves into propagating light; i.e. plasmon-photon decoupling; and (4) transmission of light through thin metallic grating films by tunneling, which is enhanced where field is strongly localized.

As an optical diffraction coupler, the optical wave momentum along the grating surface should be conserved for phase matching. Along the grating surface, coupled diffraction beam should satisfy the wave vector component

$$k_x^{(m)} = k \sin \theta + \frac{2\pi}{d} m \quad (m = 0, \pm 1, \pm 2, \dots), \quad (3.5)$$

where $k = 2\pi/\lambda$, the wave vector in the medium at the incidence side of the gratings; d is the grating period; and m is the order of grating vector for coupling. Directions of the diffracted beams are determined by $k_x^{(m)}$ and $k_y^m = \pm\sqrt{k^2 - k_x^{(m)2}}$ (the sign “+” indicates the direction away from the surface). If the grating period is much smaller than the incident light wavelength, $d \ll \lambda$, only $m = -1$ order backward coupling is possible at certain range of incident angles. The condition can be obtained from $[-k_x^{(-1)}] \leq k$, i.e.

$$\sin \theta \geq \frac{\lambda}{d} - 1 \quad \left(0 \leq \theta \leq \frac{\pi}{2} \right). \quad (3.6)$$

The “=” corresponds to the (-1)-order Wood’s anomaly. For $\lambda = 633nm$ and $d = 370nm$, it is obtained that $\theta \geq 45.3^\circ$. This will accordingly reduce the zero-order reflected beam power for energy conservation, which explains the overall lower zero-order reflectance at larger incidence angles. At smaller angles, the light cannot “see” the grating structures. Losses are also introduced by absorption and diffusive scatterings in all the angular range.

The Wood’s anomaly position is close to but different from that of the surface plasmon coupling due to the different coupled wave vector (or momentum). One is an optical mode; the other is a surface plasmon mode. The related dielectric constants are slightly different. At silver/air interface, the surface plasmon wave vector is denoted by

$$k_{sp} = k_0 \sqrt{\frac{\epsilon_m}{1 + \epsilon_m}}, \quad (3.7)$$

where k_0 is the wave vector in air, ε_m is the dielectric constant of silver at the wavelength of 633 nm. Assume $\varepsilon_m = -15 + 1i$, the effective index of surface plasmons at the interface will be $n_{eff} = \sqrt{\varepsilon_m / (1 + \varepsilon_m)} = 1.035 + 0.0025i$, compared to $n = 1$ in air for the Wood's anomaly.

Since the surface plasmon wave has an evanescent wave vector in the directions normal to the interface, it only propagates along the surface. The phase matching condition also need to be conserved in the photon-plasmon coupling and plasmon-photon decoupling processes, i.e.

$$k_{sp} = k \sin \theta + \frac{2\pi}{d} m \quad (m = 0, \pm 1, \pm 2, \dots), \quad (3.8)$$

The propagating surface plasmon coupling and decoupling processes are schematically illustrated in Figure 3.17 with phase diagram. The diagram is sketched in scale resembling the case with $\lambda = 633\text{nm}$ and $d = 370\text{nm}$, where only (-1)-order backward SP coupling is possible. And the coupling angle is calculated with Equations (3.7) and (3.8) to be 45° .

It has been widely studied experimentally and theoretically, and is well known that main feature of zero-order reflection of a shallow metallic grating (1~20 nm) is a dip near the SP coupling angle [7]. But shown in Figure 3.16, for the grating depth of 30 nm, a sharp dip appears at the angle 42° slightly smaller than the SP coupling angle of 45° calculated from Equation (3.8). And as the grating depth is increased to 120 nm, no sharp dip appears; it corresponds to an overall low reflectance at all angles. Here, we will clarify that, ideally, the SP coupling and

decoupling are symmetric reverse processes, there should be no reflection quenching at this angle for semi-infinite metal. For smooth thin metal films, SPs are coupled from light with ATR method; it is the strong damping due to destructive plasmon wave resonances across the thickness of metal film that causes the reflection quenching [7, Section 2.2]. For thin metal films with shallow sinusoidal gratings, the reflection quenching position shifts depending on the grating depth [7, Sections 6.2 and 6.3]. It has been shown experimentally and also explained with calculations of Rayleigh method. Explicitly, we can attribute it to the variations of phase retardation on grating depths during coupling. Physically, it is related to the scattering of SP charges and surface EM waves by small curved features of corrugated metal surfaces. If the grating film is thin enough, the locally intensified field by scattering enhances the tunneling of plasmon waves through the film; as destructive resonance is established inside, strong reflection quenching is resulted.

Generally speaking, in the above cases, the reflection quenching is a result of enhanced power leakage and absorption due to destructive resonance in thickness. The general internal processes at SP coupling condition are shown in Figure 3.18(a). And this is also the similar case for the shown metallic gratings of Figure 3.16(a) with rectangular corrugations, depth of 30 nm and Ag thickness of 40 nm. The SP wave propagation has the traveling wave characteristics. The reflection spectrum peak at $\sim 45^\circ$ in Figure 3.16(a) has the same nature as reflections in smaller angles; it is formed by neighboring with the -1 -order diffractions at larger angles and the SP resonance resulting reflection quenching at $\sim 42^\circ$. This SP resonance angle is slightly smaller than that calculated from planar surface SP coupling conditions because of phase retardation

introduced from scatterings at small features of grating edges. Over one grating period, the phase matching conditions can be written as

$$k_{sp} \cdot d + \Delta\varphi^{(m)} = (k \sin \theta) \cdot d + \frac{2\pi}{d} m \cdot d \quad (m = 0, \pm 1, \pm 2, \dots), \quad (3.9)$$

where $\Delta\varphi^{(m)}$ is the phase retardation for m -th order coupling, $\Delta\varphi^{(m)} > 0$. For backward coupling, $m < 0$, the coupling angle θ shifts to be smaller; and for forward coupling, $m > 0$, it shifts to a larger angle. The forward coupling is realized with gratings with period larger than the incidence wavelength, which is shown in Figure 3.20 for $d = 780\text{nm}$. Accordingly, the spectrum profile is inverted from that of the 370-nm-period case. It is readily to be understood with the above explanations. The SP coupling was calculated at an angle of $\sim 13^\circ$.

If the depth of a subwavelength metallic gratings is very large and film is thick, e.g. for that of Figures 3.10(b) and 3.13(a), the SP propagation does not involve the metal surface at the bottom of the grating grooves. Although the SP energy flow is coupled through the air space between adjacent grating ridges, there is almost no charge exchange between them. The charge oscillation is localized at each ridge surfaces. Since the film is thick, there is no resonance formed through the thickness of the grating film. Coupled SP waves are readily decoupled into reflected light. In this case, there is still -1 -order diffraction coupling at larger angles. At small angles, low reflectance can be ascribed to large diffusive Mie-scatterings of the rough grating film. Shown in Figure 3.19(a) is a schematic model of the charge/field distributions. The similar case for thick transmissive metallic gratings with very narrow slits is also shown in Figure 3.19(b), which gives a reflection spectrum as Figure 2.7. It is distinguished that, for the thick

deep reflective gratings, there is very weak energy tunneling and leakage; while there is strong energy leakage through the slits for transmissive gratings. This basically explains the difference of reflection and transmission spectra of the two type gratings in small angle range shown in Figure 3.16(b) and Figure 2.7. Additionally, Fabry-Perot-like resonance characteristic is also shown for the transmissive gratings.

Experiments were also performed for samples with same grating period, depth but different deposited metal thickness. A weaker reflection quenching was observed although they have the similar reflection and transmission spectra features.

The corresponding low reflectance to high transmittance in all these spectra also strongly suggests the reflection quenching as a result of power tunneling/leakage and absorption.

The phenomena suggest applications of subwavelength metallic gratings without interference of higher order diffractions in spatial and power distribution. The reflection quenching for thin metallic gratings at SP coupling conditions can be used as a stop-band filter. By varying the incidence angle for a designed grating structure, the stop-band can be shifted in the wavelength range of interest. Optimizing the grating structures and dimensions, a narrow, near-zero reflectance stop band is expected to be achievable. The very thin subwavelength metallic gratings have also been shown to greatly enhance the responsivity of compound semiconductor photodetectors [59], efficiency of ultrafast photodetections [60] and the photoluminescence intensities of quantum wells [25], etc.

The SP excitation on thick shallow metallic gratings is accompanied with a great enhancement ($> 10^2$) of field intensity in the near field of the grating surfaces. The strongly localized field can be used to excite organic molecules and active quantum particles for applications in sensor detections, material chemical spectrum analysis and fundamental study in optical quantum effects of small particles.

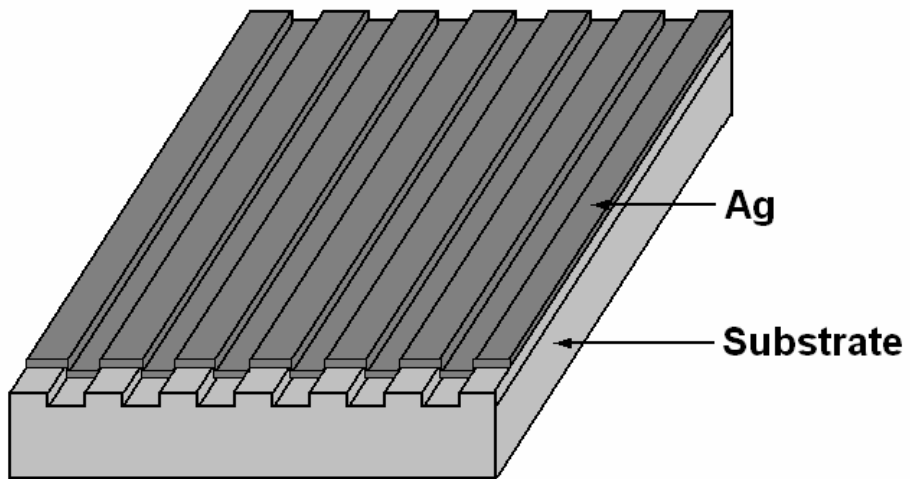
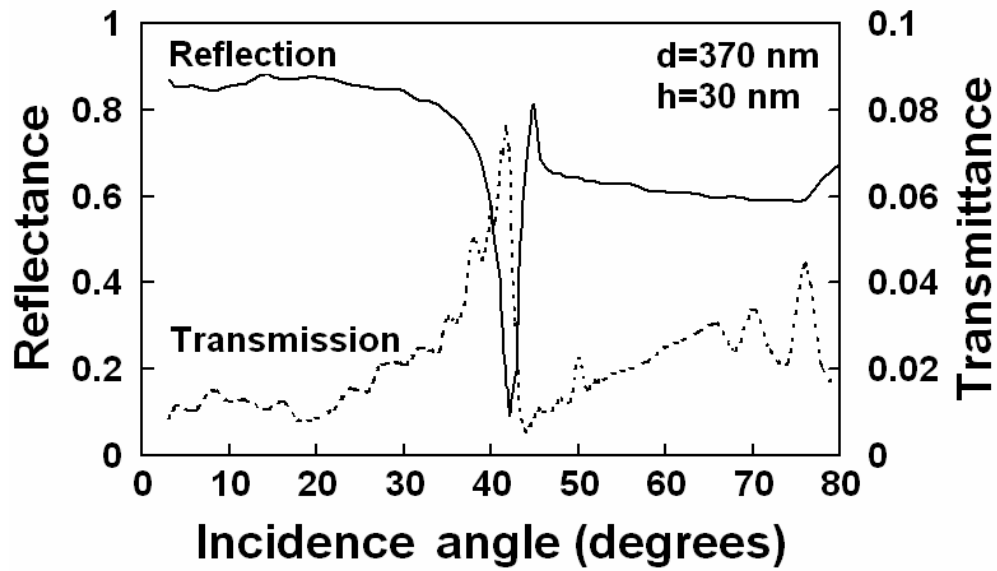
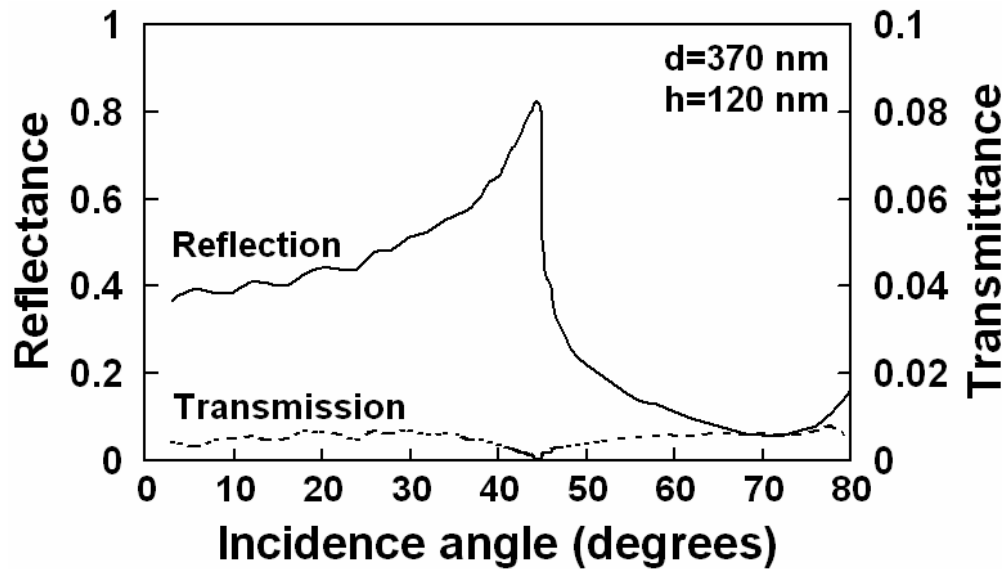


Figure 3.15. Schematic drawing of the 1D metallic reflective gratings. Silver is normally deposited onto the gratings etched into the surface of silica substrate.



(a)



(b)

Figure 3.16. Angular dependence of TM-polarized Zero-order reflection and transmission of thin metallic reflective gratings with different depth thickness. (a) Period $d=370$ nm, depth $h=30$ nm, Ag thickness $t=40$ nm; (b) Period $d=370$ nm, depth $h=120$ nm, Ag thickness $t=170$ nm. The incidence beam is collimated output of a He-Ne laser with its wavelength of 633 nm.

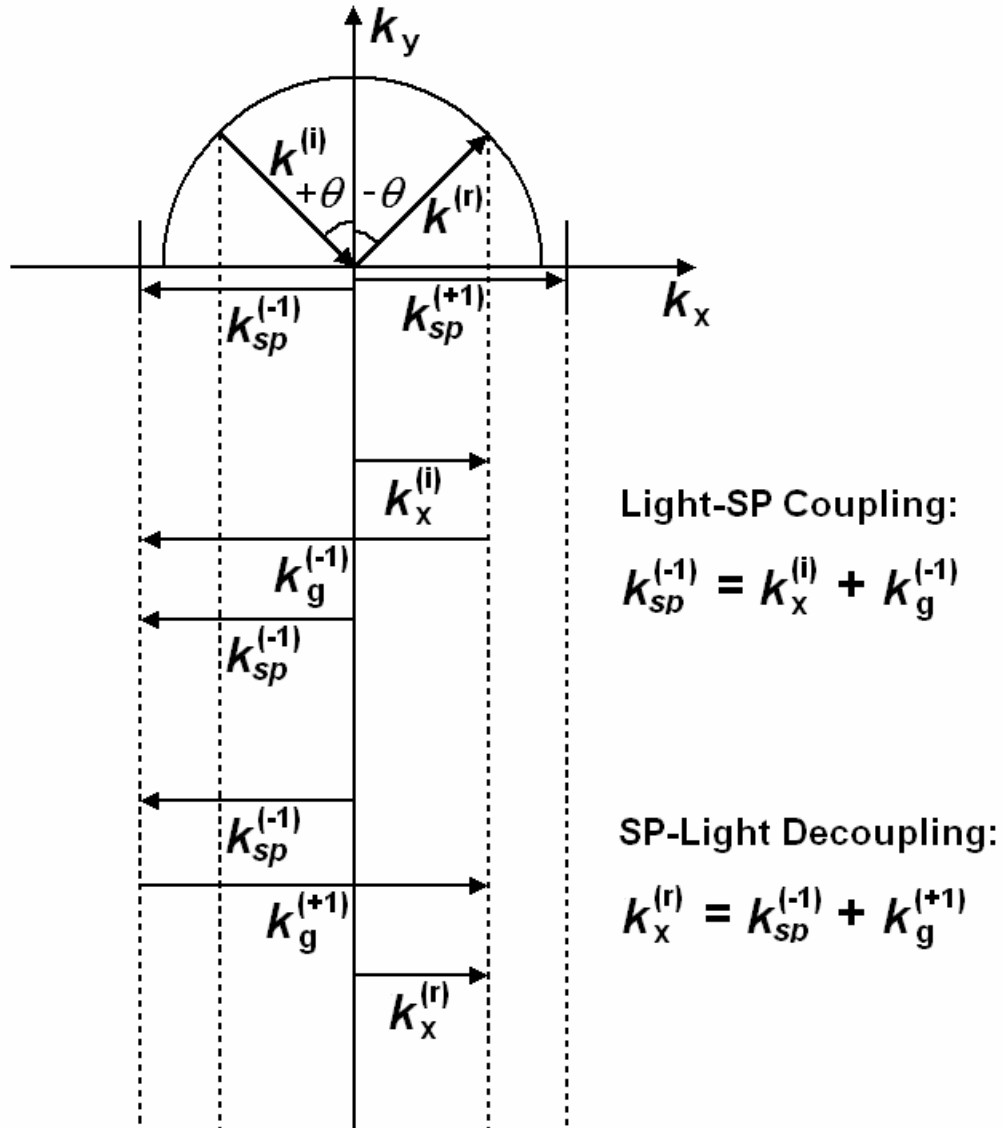


Figure 3.17. Schematic phase matching diagram of backward light-SP coupling and SP-light decoupling with subwavelength metallic gratings. In the diagram, $k^{(i)}$ and $k^{(r)}$ denote the incidence and decoupled (reflection) light wave vector, $k_x^{(i)} = k^{(i)} \sin \theta$, $k_x^{(r)} = k^{(r)} \sin \theta$, $k_x^{(i)} = k_x^{(r)}$, $k_g^{(m)} = \frac{2\pi}{d} m$ ($m = 0, \pm 1, \pm 2$), and $k_{sp}^{(\pm 1)} = \pm |k_{sp}|$.

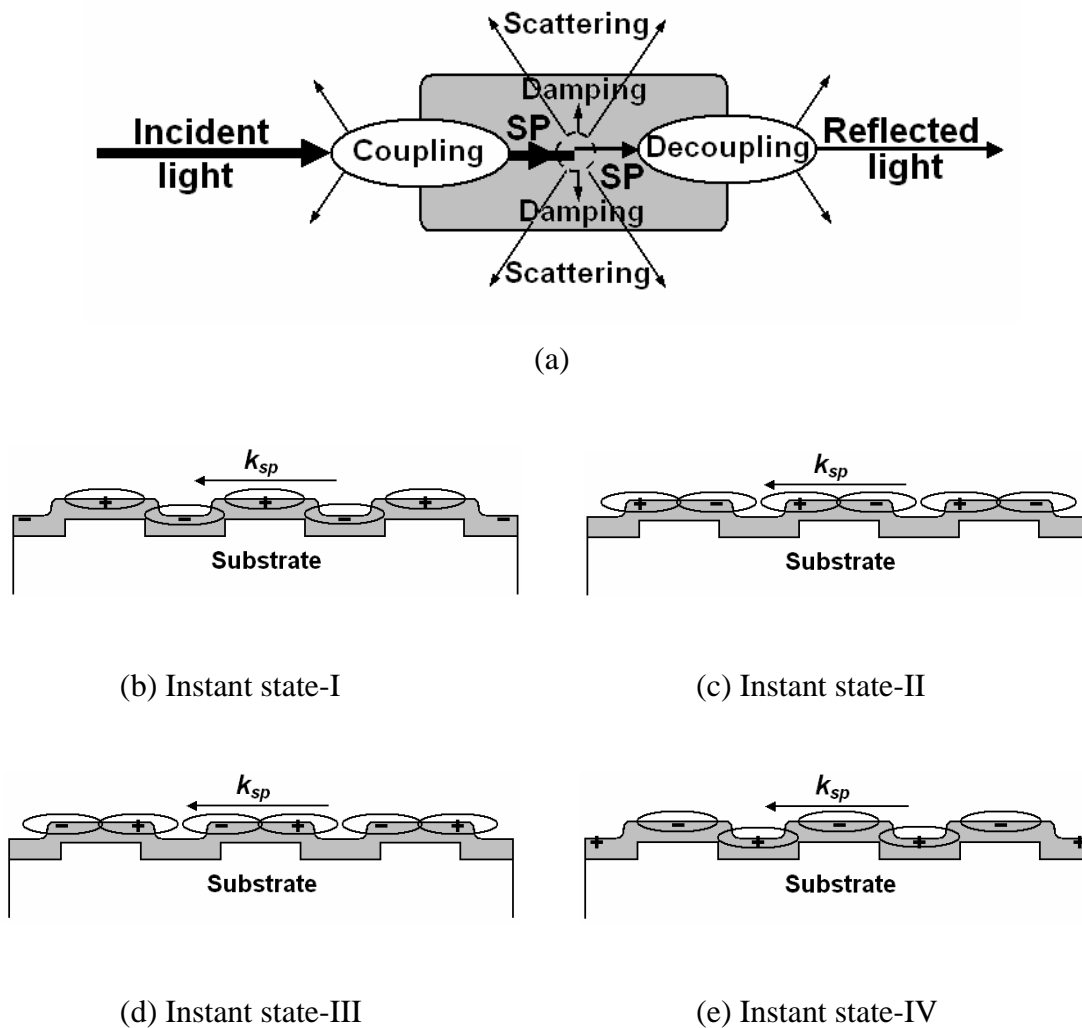
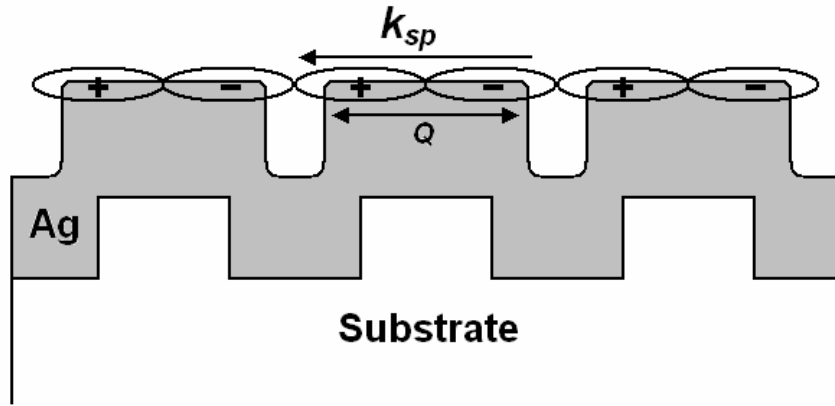
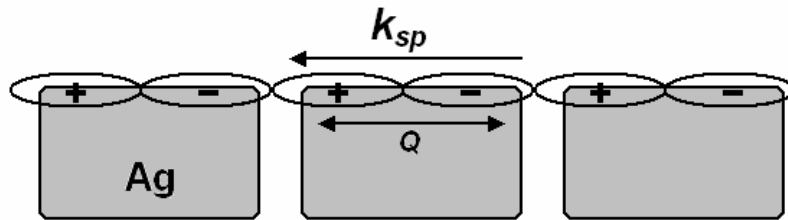


Figure 3.18. Coupling of light into surface plasmon waves with shallow silver gratings. (a) schematic illustration of the physical processes during coupling of light into SPs and decoupling of SPs into light. (b)-(e) are four instant state of coupled SP propagations with $\pi/4$ phase intervals. The schematics are scaled to the gratings of Fig. 3.10(a).



(a) Very deep metallic reflective gratings



(b) Thick metallic transmissive gratings with very narrow slits

Figure 3.19. Coupling of light into surface plasmon waves with deep reflective gratings and thick transmissive gratings. (a) deep reflective silver gratings: . (b) thick transmissive gratings with very narrow slits. The schematics are scaled to the gratings of Fig. 3.10 (b) for (a) and Fig. 2.7 for (b).

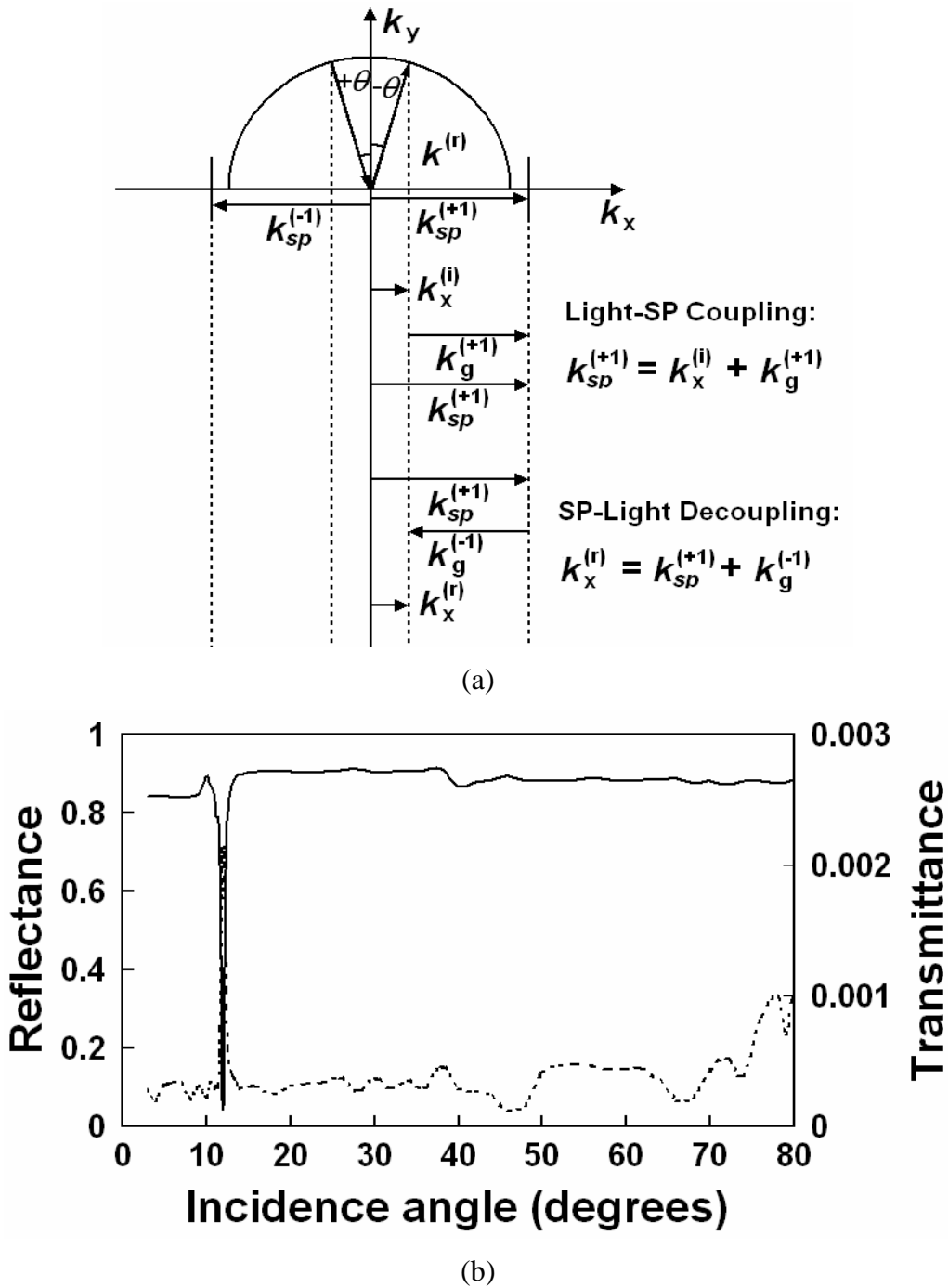


Figure 3.20. Forward coupling of light into surface plasmons with metallic gratings. (a) Schematic phase matching diagram for SP coupling and decoupling; (b) TM zero-order reflection and transmission dependence on incidence angles. A reflection dip appears at SP coupling conditions around 13° . The grating has a period larger than wavelength.

3.4 SUMMARY

- The 2D nano-hole arrays in thick metallic film were formed utilizing anodized alumina pore arrays as a template; enhanced transmission was observed in the pass band which is determined by the periodicity.
- Combining the wavelength and polarization filtering property of the nano-slit arrays in thick metallic films, a tunable resonator structure was demonstrated.
- Near-field interaction in optical transmission through bi-layers is studied. Their characteristics and interaction mechanisms are explored with FDTD simulation and model analysis.
- The reflection and transmission properties of 1D metallic reflective gratings were studied; the defined reflection quenching and field localization suggest wide potential applications in photonics, optoelectronics, chemical sensing, biomedical analysis, and small particle assembling.

4.0 REFRACTIVE TRANSMISSION OF LIGHT AND BEAM SHAPING WITH METALLIC NANO-OPTIC LENSES

Beam shaping is an important concept in optics, and is commonly involved in a variety of optical components and instruments. Focusing and/or collimating an optical beam through dielectric lenses with curved surfaces are a classical example of conventional refractive optics. In diffractive optics, the refractive elements are modified by microscale modulation of incident light. The optical fields emitted from different diffraction zones interfere and form a desired wavefront. Here we propose a metallic nanoaperture array structure that performs beam shaping in a way distinctively different from the refractive or diffractive optics and that can overcome limitations of the conventional optics, especially in the scalability of physical dimensions and designability of beam shaping. The nanoaperture array structure, involving a plasmonic interaction with an incident beam, is designed to transmit light with proper phase retardation among aperture elements such that the optical fields emanating from the apertures evolve into a certain beam shape. Finite-difference time-domain (FDTD) analysis demonstrates the beam shaping functions (refraction, focusing and near-field collimation) of the metallic nano-optic structures.

Conventional dielectric lenses focus light via refraction at curved surfaces with index contrast. In the language of wave optics, a lens provides proper phase retardation to the optical fields emanating from infinitesimal dipole elements that are continuously distributed on the exit surface of a lens [2]. In diffractive optics, optical fields are changed by means of diffraction

through zones of microscale features formed on a dielectric [62]. An incident beam diffracts at each zone with different angle, and this has the effect of modulating the phase of the incident field, thus enabling flexible beam shaping even at reduced sizes of optical elements. Whereas dielectric is commonly used in conventional refractive or diffractive optics, utilization of metal in beam shaping has been limited to the non-transmissive mode of operation such as reflection or diffraction [7]. This is mainly due to the blocking nature of metal in interacting with light. It is, however, worth mentioning that nano-apertured metal structures have been drawing increasing attention as an interesting medium for optical interaction since the recent experimental observation of an extraordinary transmission of light through nanometer-sized hole arrays or through a single hole (or slit) surrounded by surface corrugations formed in metallic films [14, 15, 63-67]. While this opens up a new avenue for transmissive optics, the potential for metallic refractive optics has not been explored yet.

Recently, we reported the refractive transmission of light through a metallic nanoslit array and demonstrated beam shaping (focusing or collimating) functions of the convex-shaped metallic lenses [68]. Each nanoslit element in the lens structure was designed to transmit light with a phase relationship controlled by the metal thickness profile of the array lens. The metal-based refractive optics was shown to offer functions that would complement the beam shaping capability of conventional refractive or diffractive optics. Let's start the review with analyzing the optical transmission of a single narrow slit.

Figure 4.1 shows a FDTD simulation of optical transmission through a single nanoaperture (80-nm-wide single slit) formed on a metal layer (200-nm-thick silver). An optical

beam (TM-polarized plane wave with 650 nm wavelength) is incident from the bottom side in the image. The dielectric constant $\epsilon=-16.19+i1.05$ is used for silver. The incident wave excites a surface plasmon (SP) mode at the slit entrance. The SP wave propagates along the slit region with a complex propagation constant, and then decouples into radiation modes at the slit exit, diffracting into all radial directions with a uniform power distribution. In order to establish a quantitative understanding, we analyzed the SP propagation in the slit region by solving the Maxwell's equations with proper boundary conditions, i.e., that the tangential components of the magnetic and electric fields are continuous at the metal/dielectric interface, as described in Section 2.4. The surface plasmon wave vector and thus the complex index n_l are calculated for TM wave propagating in a silver slit region. [See Figure 4.2(a)] Here the complex refractive index n_l relates the surface plasmon wave vector k in the slit region to the wave vector in the air region, $k=n_l k_0$. The real part of the propagation constant is shown to be much larger than the imaginary part; therefore the wave is propagation dominant. For an 80-nm-wide slit formed in silver, for example, n_l is calculated to be $1.27+i0.01$ at 900 nm wavelength. As the slit width is further reduced, both the real and imaginary parts of index n_l increase, indicating that the portion of the SP field in the metal region grows.

The transmittance through a slit of finite depth is expressed as follows:

$$A = \left| \frac{\tau_{01}\tau_{12}e^{ikh}}{1 + \rho_{01}\rho_{12}e^{i2kh}} \right|, \quad (4.1)$$

$$\phi = \phi_{01} + \phi_{12} + n_l k_0 h - \theta. \quad (4.2)$$

Subscripts 0, 1, and 2 denote the media before, inside, and after the nanoslit array, respectively, in terms of beam propagation. ρ_{01} and ρ_{12} are the reflectivity of surface plasmon wave at the air-metal and metal-substrate interfaces of the α -th slit, respectively, and are given as $\rho_{01} = (n_0 - n_1)/(n_0 + n_1)$ and $\rho_{12} = (n_1 - n_2)/(n_1 + n_2)$. $\phi_{01} = \arg(\rho_{01})$ and $\phi_{12} = \arg(\rho_{12})$. $\tau_{01} = 1 - \rho_{01}$ and $\tau_{12} = 1 - \rho_{12}$. n_0 and n_2 are the refractive indices of the media outside the slit array layer. $\theta = \arg(1 + \rho_{01}\rho_{12}e^{i2kh})$. h is the slit depth. In general, both the amplitude (i.e., transmittance) A and phase ϕ are complex functions of the structural and materials parameters (such as slit width, depth and spacing, and dielectric constants) and the operating wavelength relative to slit spacing [20, 22, 69, 25, 70, 27]. In the regime where the surface plasmon waves localized at each slit do not couple to a significant degree, both the transmittance (A) and phase (ϕ) of optical field are primarily determined by slit depth, i.e., metal thickness [Figure 4.2 (b) and (c)]. The calculation shows that the amplitude change remains relatively insignificant over a broad thickness range, i.e., with a variation of 0.89 – 0.98 for the metal thickness of 100 – 1000 nm in the case of 80 nm slit width. The periodic fluctuation of amplitude indicates the Fabry-Perot resonance of surface plasmon wave in the nanoslit region. The calculation also shows that the phase of optical field is almost linearly proportional to slit depth.

Here, two factors can be used to control the phase difference during light transmission through the slits, and thus perform beam shaping, i.e. the metal layer thickness (slit channel length) and slit width (modifying the effective index).

Figure 4.3 shows FDTD simulation of transmission of light (TM-polarized and 900 nm wavelength) through a three-slit structure. 80-nm-wide slits are introduced on a Ag layer with a

370-nm spacing (center to center), and the Ag layer thickness is varied with a 50-nm step profile such that the slit depth becomes 250, 300, and 350 nm in sequence. The different slit depth is to introduce phase retardation among the radiation components at the exit surface of metal. The FDTD analysis result clearly reveals that the transmitted beam propagates along the direction tilted towards the thicker side of metal. This behavior is reminiscent of the refraction of light in conventional dielectric optics. This observation is corroborated with the following simple analysis. The optical fields (the magnetic field H_z) in the far-field regime of a beam transmitted through the nanoslit array can be expressed as a summation of the cylindrical waves from each nanoslit element.

$$H_z(x, y) = \sum_{\alpha} \frac{A_{\alpha}}{\sqrt{r_{\alpha}}} e^{i\phi_{\alpha}} e^{ik_0 r_{\alpha}} \quad (4.3)$$

Here, $r_{\alpha} = \sqrt{(x - x_{\alpha})^2 + (y - y_{\alpha})^2}$, and k_0 is the wavevector of the transmitted beam in the air region. A_{α} and ϕ_{α} are respectively the amplitude and phase of the radiation component emanating from the α -th slit located at (x_{α}, y_{α}) , and are expressed as Equations (4.1) and (4.2) if we assume no resonance coupling occurs between the neighboring slits. It can be shown that the transmitted waves through the nano-slits will beam into the direction that satisfies the following phase matching condition at the metal/air interface: $k_{sp} \sin \theta_i = k_0 \sin \theta_t$. Here θ_i is the incidence angle of the surface plasmon wave to the hypothetical planar surface that comprises the slit apertures, and θ_t is the tilt angle of the transmitted beam. This formula basically tells that light will refract at the nano-apertured metal surface in the same manner as in the case of dielectric interfaces. From the phase matching condition and the information on the nano-optic structure shown in

Figure 4.3(a) (the index ratio of 1.27 and the incident angle θ_i of 9 degrees), the transmission angle θ_t is calculated to be 11 degrees, which shows a close reasonable match to the angle observed in the FDTD simulation (~ 12 degrees). It should be noted that the slit spacing in this design is smaller than the wavelength of light. Therefore, no grating diffraction effect is involved in the optical transmission through the nano-optic structure, unlike the diffractive optics case.

Figure 4.4 (a) shows a nanoslit array lens that has a convex profile in its metal thickness. The convex region is with 2- μm -diameter, and accommodates up to five slits (80-nm slit width) for 400-nm slit spacing (center to center). The metal thickness in the lens region is designed to vary in a half-elliptical profile such that the slit depth in the array is 250, 320, 400, 320, and 250 nm. Figure 4.4(b) shows the beam shaping (TM-polarized wave with the wavelength of 650 nm) through a three-slit lens structure. (The outer two slits in Figure 4.4(a) are omitted in this three-slit lens.) The simulation result shows that the incident beam becomes sharply focused right after the lens with a beam waist of ~ 400 nm. Figure 4.4(c) shows optical transmission through a five-slit lens structure. The incident beam becomes focused after the lens and remains well collimated with negligible divergence even after many wavelengths of propagation in the far field region. This indicates an increase of focal length in the five-slit lens compared to the three-slit case. This also demonstrates that the radiation components from the outer slits also reach the far-field region and contribute to beam shaping with proper phase retardation.

In order to compare the beam shaping characteristic of the nanoslit array lenses with that of conventional dielectric lenses, we also simulated the optical transmission through a dielectric

lens structure. Figure 4.4(d) shows the cross-section of a glass convex lens, whose dimension is approximately the same as the nanoslit array lens shown in Figure 4.4(a): 2- μm lens width and 600-nm lens thickness. A beam (650 nm wavelength) is incident from the bottom side in the image. The transmitted beam shows a strong diffraction effect at the lens edges, although a focusing effect is also evident in the central region. As the lens width is further reduced, the edge diffraction effect gets even more serious, becoming one of the limiting factors in scaling down the conventional optics components to a wavelength or subwavelength range. This is a big contrast to the nanoaperture array lens case, in which the edge effect is absent due to the blockage of light outside the array region. The maximum lateral dimension of a transmitted beam is basically determined by the aperture array dimension, an interesting feature that would enable beam shaping at various length scales in a discrete or array form. In the nano-optic lens structures described above, the phase relationship among slits is primarily controlled by metal thickness. While the shape (geometry)-controlled beam-shaping of metallic lenses resembles conventional refractive optics, the mechanisms involved in optical interactions are distinctly different, and as such their beam-shaping characteristics. The discrete distribution of propagation channels (nanoslit arrays) across a metallic lens is contrasted to the continuous nature of a conventional refractive lens, analogous to digital versus analog.

The phase of each nanoslit element can also be controlled by adjusting other structural and/or material parameters of nanoslits, such as slit width or the dielectric constant in the slit region. The principle is that, by controlling the slit width, the effective indices of plasmon waves inside slits are modified, and hence we can control the phase retardation at different slits. Our investigation also shows that, except for the phase retardation, the field amplitude of the dipole

source at each slit exit also significantly modify the beam profile in the near field regime. Other factors, such as the slit spacing, number of slits, and metal layer thickness, all closely relate to the beam shaping in different ways.

Figure 4.5 and shows FDTD simulation indicating beam steering and focusing with metallic nanoslit array structures, in which the slit widths are modified to control the transmission beam profile. For comparison, we also show the case with equal slit widths in Figure 4.5 (a), where there is no indication of any beam shaping and clear beam confinement for focusing. In Figure 4.5 (b), a light beam (TM-polarized, wavelength 650 nm) is incident onto a metallic slit array of thickness 300 nm. The five slits are equally spaced (200 nm center-to-center) and their widths are linearly varied (40, 60, 80, 100 and 120 nm). The simulation clearly indicates that the transmission beam profile is well confined and propagates in the direction that is tilted (~ 7 degrees) toward the narrower slit side, which is supposed to have larger effective index for plasmon waves inside slits and thus induces larger phase retardation. Mentioned that increasing the metal layer thickness at the same time will further result in even larger phase difference for deep refraction. In Figure 4.5 (c), to realize focusing, we tend to construct the slit array with the middle slits having larger indices, so we set the slit width to be narrower for the middle ones, and the slit widths are 120, 80, 40, 80 and 120 nm in sequence. In this simulation, the slits are separated with 200 nm (center-to-center) spacing and the metal layer thickness is also 300 nm. TM-polarized light of wavelength 650 nm is normally incident on to the slit arrays.

Basically, the beam profile simulated in Figure 4.5 can be reproduced with the models proposed previously with Equation (4.3), in which the phase term ϕ_α is the product of the metal

layer thickness (channel length) and plasmon effective index that was calculated and shown in Figure 4.2 (a). A close inspection of the beam steering shows that, in the near field, as-formed beam propagation direction is gradually bended and more complex than that in the far field [see Figure 4.6 (a)]. In Figure 4.6 (b) and (c), we modeled the problem by assuming equal element source magnitudes [in (b)] and slit width dependent element source magnitudes [in (c)]. This clearly reveals the near field beam profile dependence on element source magnitudes resulted from different slit widths.

In overview, we realized beam shaping with metallic nanoslit array lenses either by geometrically design the slits with different channel lengths or different widths to modify the phase retardation. The discrete nature of apertures that emit radiation with proper phase relationship also resembles the phased array antennas used in the microwave regime [71]. It is then expected feasible to have an individual control of the phase (and also amplitude) of optical field at each slit of an array by employing these methods. This offers great freedom in beam shaping, and opens up the possibility of developing optical components that can shape arbitrary beam profiles without being restricted by the constraints of the conventional optics.

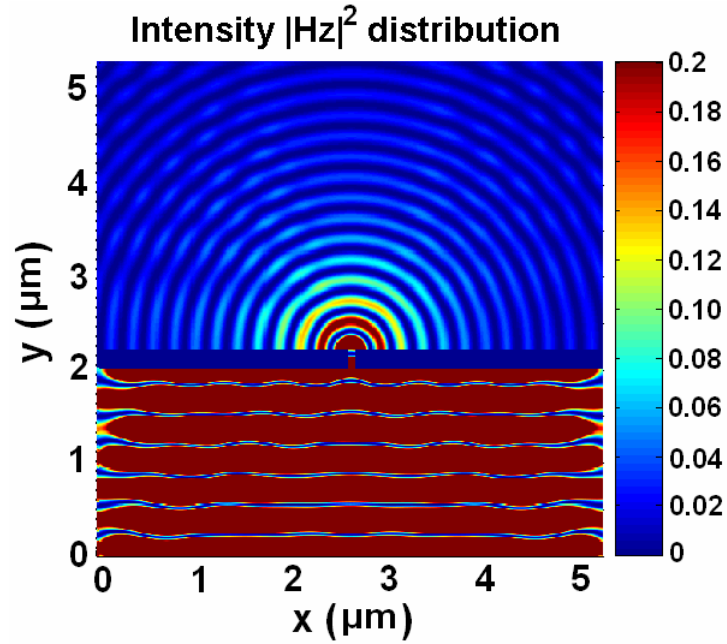


Figure 4.1. (Color) FDTD simulated optical transmission through a single nanoaperture formed on a metal layer. A TM-polarized plane wave (650 nm wavelength) is incident to the slit (80-nm-wide) in a silver slab (200-nm-thick). The wavefronts emanating from the nanoslit are clear concentric circles with a uniform intensity distribution in all directions, indicating a cylindrical wave propagation of radiation.

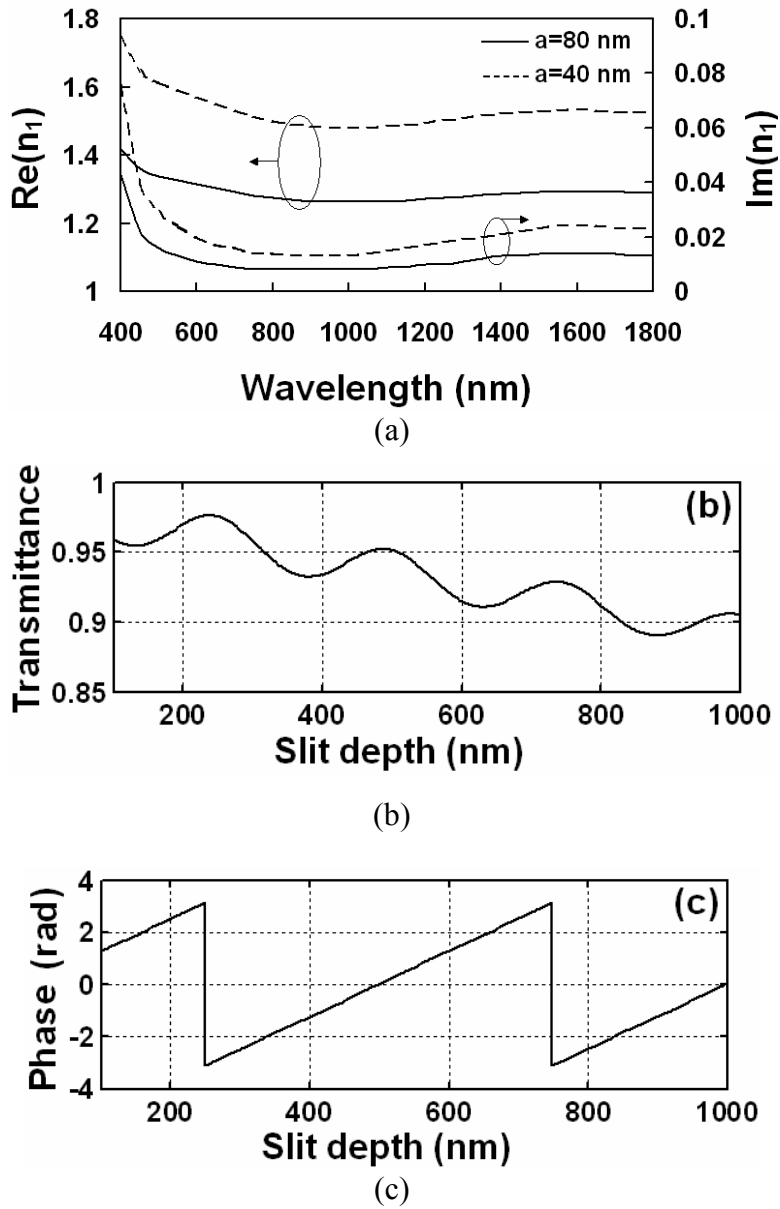


Figure 4.2. Characteristics of a surface plasmon wave through a nanoslit structure formed in metal. (a) Calculated complex effective refractive index (n_1) inside the narrow slit. (b) Transmittance (A_α) and (c) Phase accumulation (ϕ_α) of the optical field.

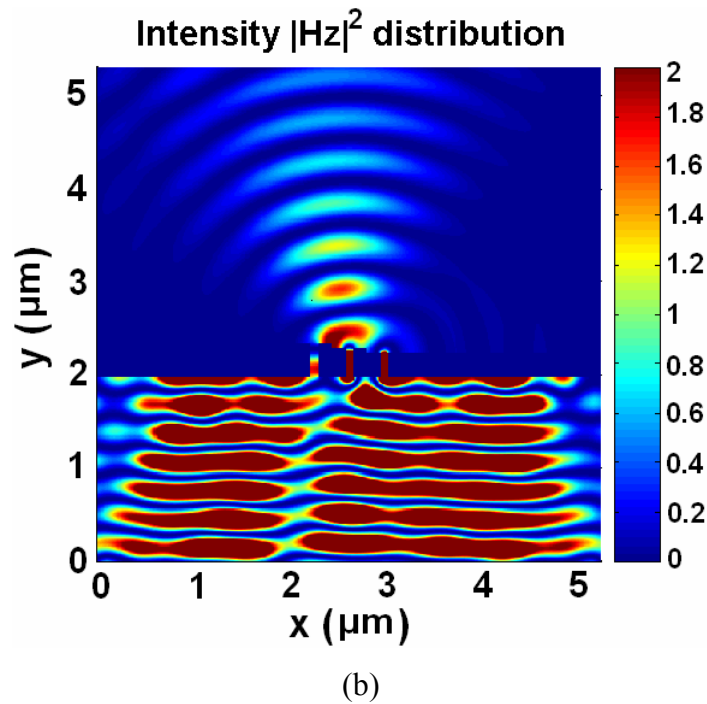
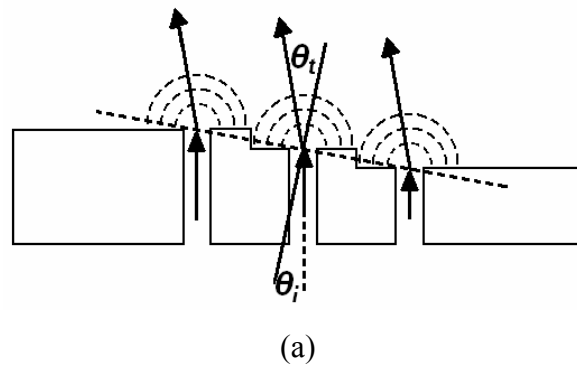
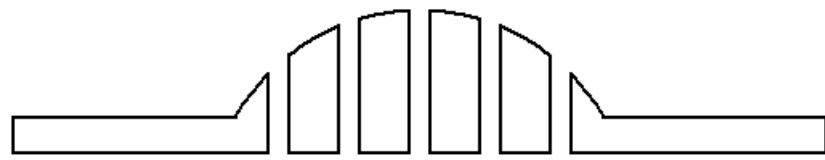
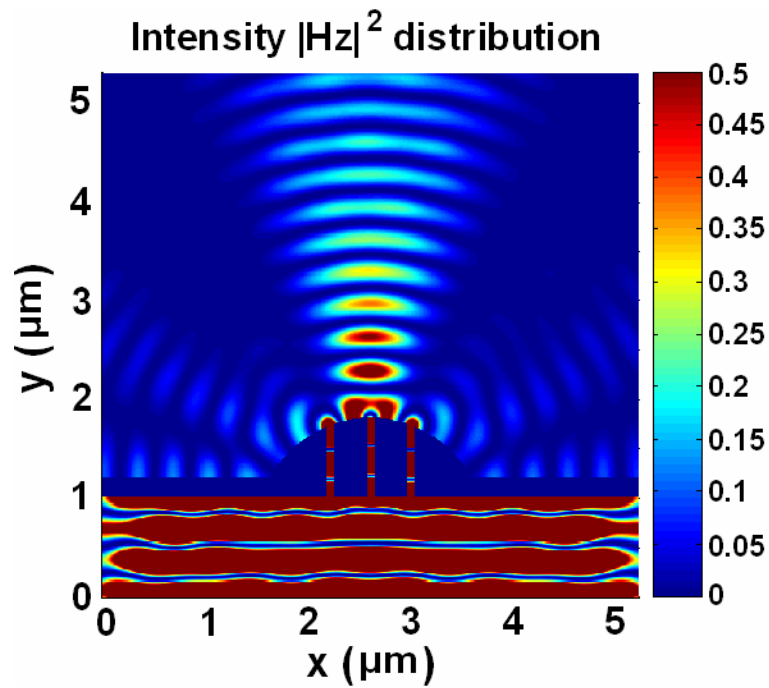


Figure 4.3. Refraction of light at a nano-apertured metal surface. (a) The cross-section of a three-slit structure, in which each slit is designed to have different depth. (b) FDTD simulated optical transmission (TM-polarized and 900 nm wavelength) through the slit array. 80-nm-wide slits are introduced on a Ag layer with a 370-nm spacing (center to center), and the Ag layer thickness is varied with a 50-nm step profile such that the slit depth becomes 250, 300, and 350 nm in sequence.



(a)



(b)

Figure 4.4. FDTD simulated beam shaping with metallic nano-optic lenses. (a) A lens structure that has a convex profile in its metal thickness (aperture depth). Five slits (80 nm slit width) are introduced to a Ag layer with 400-nm spacing (center to center). The metal thickness (slit depth) in the lens region is designed to vary in a partial-elliptical profile: the slit depth in the array is 250, 320, 400, 320, and 250 nm. The diameter of the convex region is 2 μm (The diameter of the aperture array region is 1.7 μm). (b) FDTD simulated optical transmission through a three-slit lens structure at 650 nm wavelength. (To be continued)

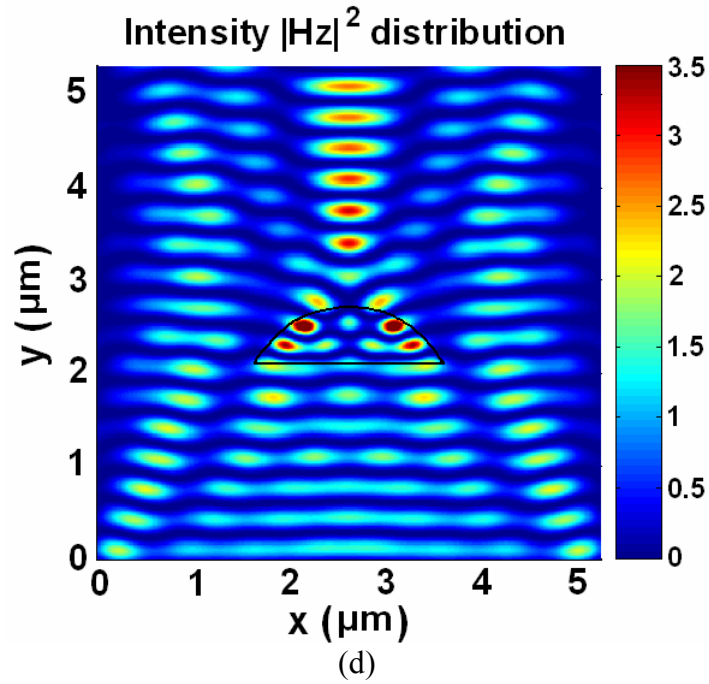
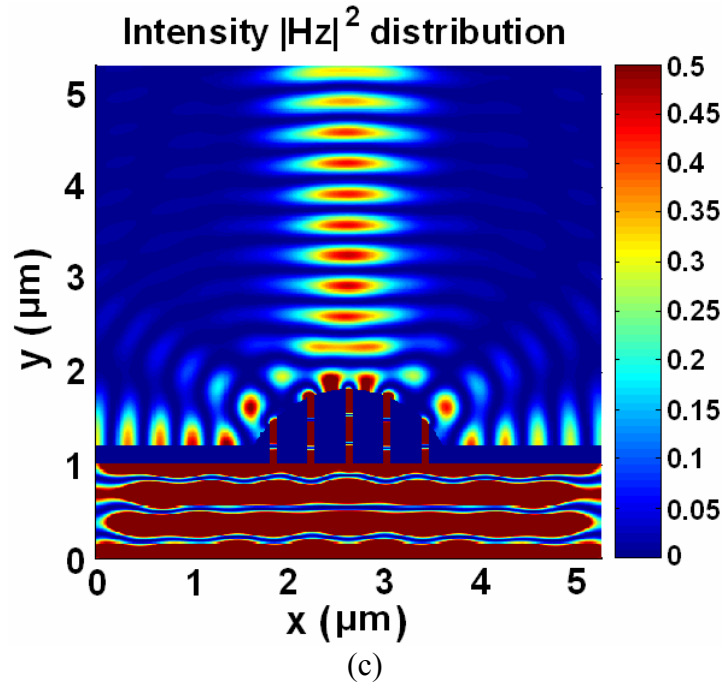


Figure 4.4. Continued (a) – (d). (c) FDTD simulated optical transmission through a five-slit lens structure at 650 nm wavelength. (d) Simulated optical interaction with a micro-scale dielectric lens.

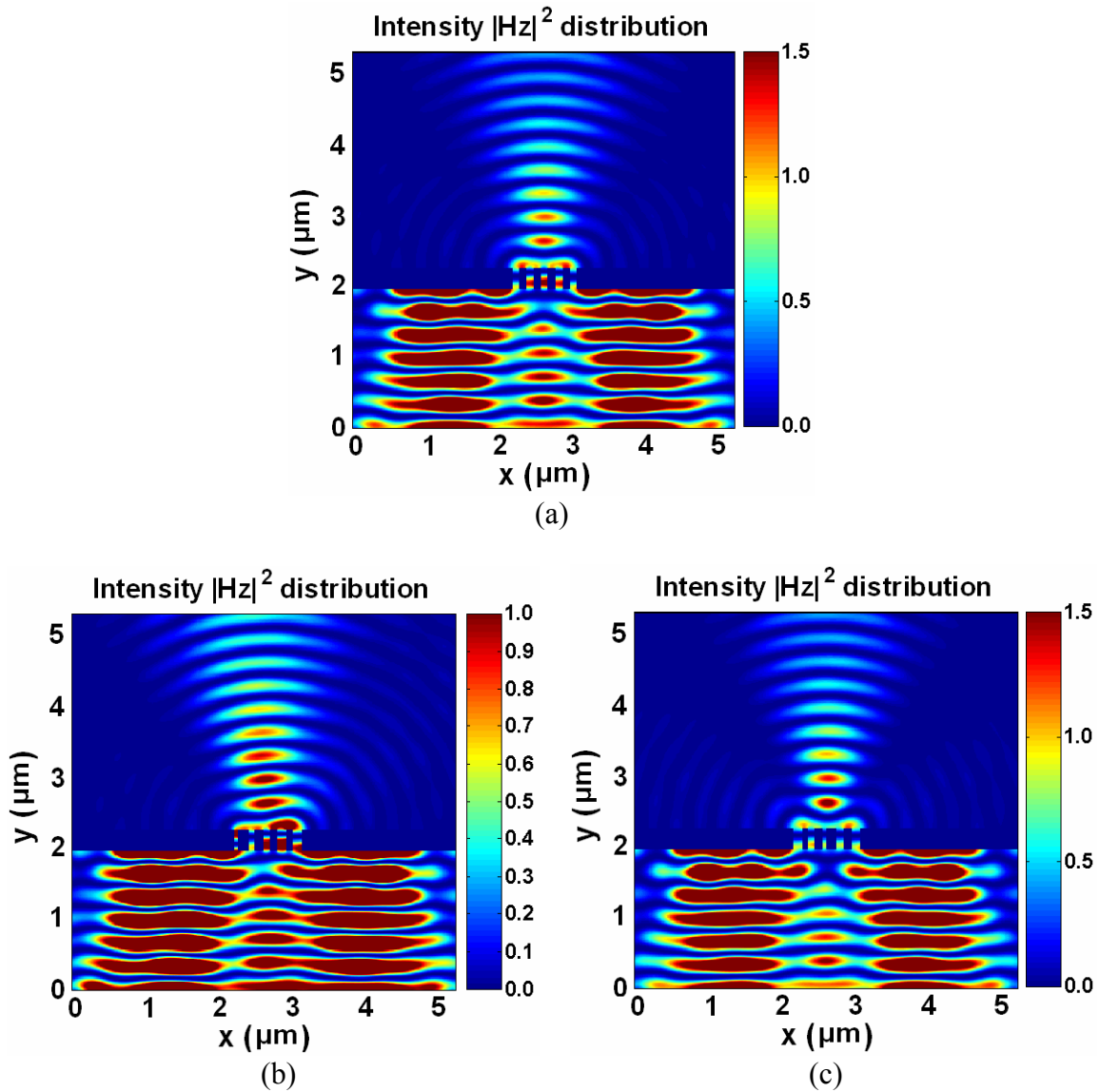


Figure 4.5. FDTD simulated beam steering and focusing with planar metallic nanoslit lenses. (a) Beam transmission through five slits in a planar Ag film of thickness 300 nm, with equal slit width (80 nm) and center-to-center spacing (200 nm). (b) Refractive beam steering. Five nanoslits are introduced in a planar Ag film of thickness 300 nm. Widths of the slits are linearly varied as 40, 60, 80, 100 and 120 nm. The slit spacing is equally 200 nm (center-to-center). (c) Beam focusing. The metal (Ag) film thickness is 300 nm. Widths of the five slits are varied symmetrically as 120, 80, 40, 80, and 120 nm. Here the slit spacing is 200 nm (center-to-center).

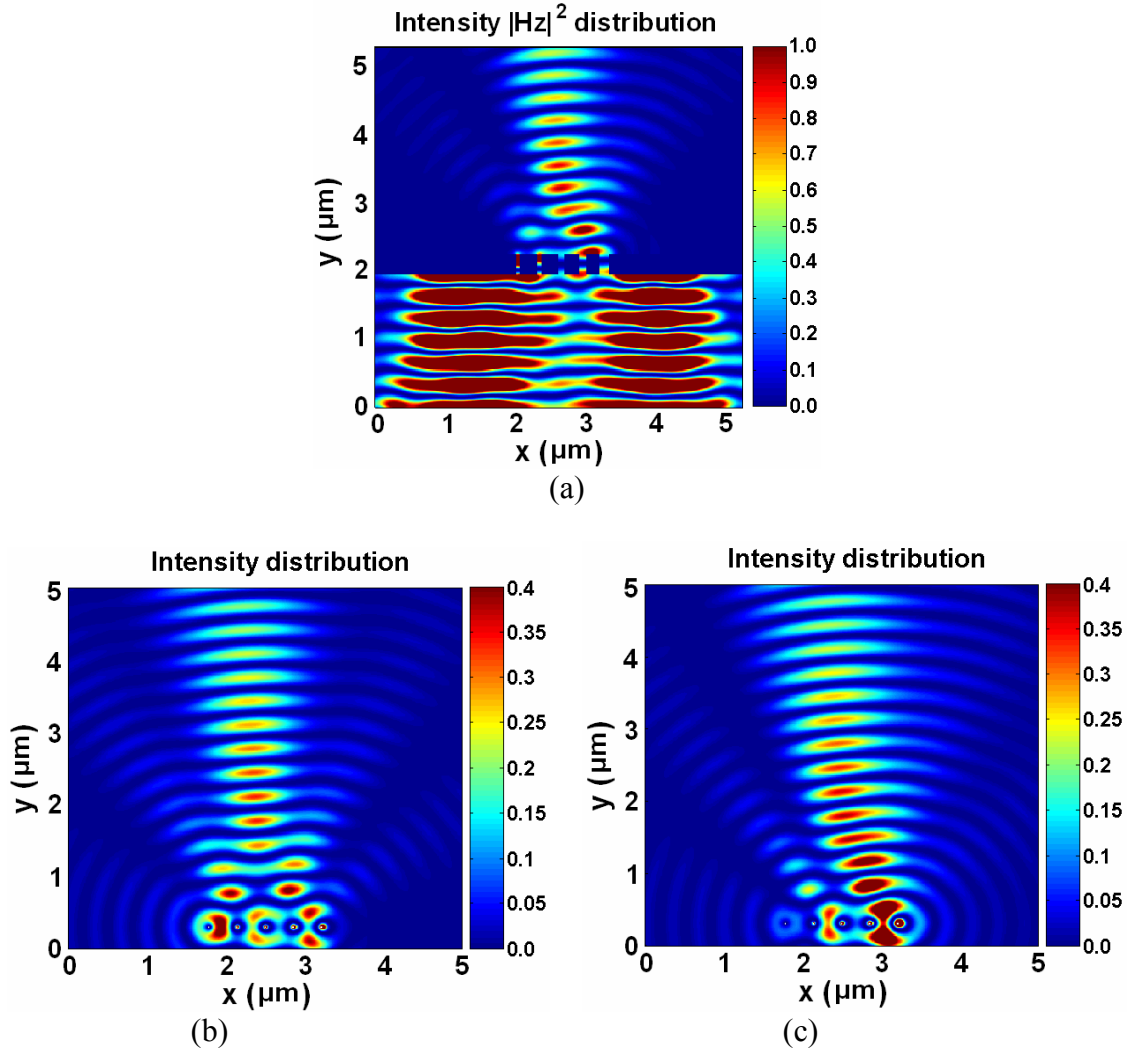


Figure 4.6. Effects of element source intensity on beam steering in near field with metallic slit arrays. (a) FDTD simulated beam steering. The metal (silver) layer thickness is 300 nm, slit spacing is 300 nm and the slit widths are 40, 60, 80, 100, and 120 nm in sequence. A light beam of 650 nm (TM-polarized) is incident onto the slit arrays. (b) Beam steering modeled with element source superposition. The spacing of aligned element sources is 300 nm. The element phases are calculated as the produce of effective index and an equivalent propagation path of 300 nm, which simulates the structure in (a). And the element source intensities are assumed to be the same as 2. (c) Difference from (b) is the element source intensities, [1, 1.5, 2, 2.5, 3], which are assumed to be linearly increasing.

5.0 CONCLUSIONS

In this thesis, we have investigated metallic nanostructures as a medium for photon/plasmon interactions. Surface plasmon (SP) waves excited with an optical beam incident to a metallic structure can propagate and interact with the metal, producing many interesting phenomena that can be observed in the near-field or far-field regime. The scope of this thesis covers both experimental and theoretical aspects. The metallic structures studied include, nanoaperture (slit and hole) arrays, reflective gratings with corrugated surface, and nanoslit array lenses. The spatial extent of SP fields is usually an order of magnitude smaller than the optical fields. Therefore, the structures are designed to span nano to micrometer length scales in order to accommodate wave interactions at different length scales, i.e., the aperture size (slit and hole) in the 10-100 nm range and the size of each metal island on the order of 100 nm or larger.

We have developed novel fabrication processes to form nanoaperture arrays of various geometry. In forming metallic nanoslit arrays, we first fabricate a periodic mesa structure on an optically transparent dielectric substrate using a holographic lithography or electron beam lithography, followed by reactive ion etching of substrate material. With angled deposition of metal, a nanoaperture array is formed on the mesa substrate without involving direct etching of metal. In forming metallic nanohole arrays, we have developed an alternative high-throughput template approach. First, highly-ordered, single-domain ($\sim\text{cm}^2$), alumina nanopore arrays with controlled symmetry are obtained by anodizing prepatterned aluminum films that were deposited on silica substrates. Holographic lithography, in conjunction with a conformal deposition

process, is utilized to form nanoscale corrugations on aluminum film surface prior to anodization. Both the order and symmetry of pore arrays were found to be well controlled and guided by the periodic surface corrugations from the initial stage of pore growth. Metallic nanohole arrays are then formed on these nanopore array substrates by angle deposition of metal.

We have investigated surface plasmon interactions in a metallic nanoslit array structure that shows characteristic transmission spectra with well-defined transmission minima and maxima in the visible-to-infrared range. Peak transmission of ~60 % is observed for TM polarization at a wavelength red-shifted from the point of surface plasmon (SP) resonance at the metal/substrate interface. At the transmission minima, the angular dependence of reflection shows a sharp peak with minimum loss of optical power. Two types of surface plasmon excitation are found responsible for the observed transmission dips: 1) the SP resonance along the planes that comprise either the metal/air or metal/substrate interfaces, and 2) the SP resonance localized along the surface that encloses each metal island separated by slits.

We have analyzed time evolution of surface plasmon resonances in the metallic nanoslit array structure by performing FDTD analysis of the field, energy flow, and polarization charge distributions. Optical interactions with a nanoslit array are found to involve different modes of SP resonances occurring at different sections of metal surfaces. At the shorter wavelength region, the transmission is governed by the SP resonances occurring at the top or bottom side of metal surfaces. At the longer wavelength region, each metal island is found to respond with a dipolar polarization and the overall transmission sensitively depends on slit width. At the intermediate wavelength region, SPs reveal a quadrupolar distribution along the periphery of each metal

island. Overall the optical transmission through a metallic nanoslit array can be understood in terms of the polarizability of the medium (metal islands separated by slits) and the periodic arrangement of nano-slits which serve as energy flow channels with a funneling effect. Designability of a metallic structure's polarizability offers an interesting potential for developing plasmonic nano-optic devices.

In surface corrugated metal films and also metallic nanoslit arrays, the main features of their reflection spectra (angular) are found to be governed by two prime phenomena: SP excitation and Wood's anomaly. The two phenomena are distinguished in terms of the media in which their coupled waves propagate. In terms of phase matching conditions, the two phenomena occur at close proximity. At Wood's anomaly, the incident beam couples into higher-order diffractions and it results in a reduction in specular reflection. Surface plasmon coupling also results in a dip in the reflection spectra. Detailed reflection spectra depend on the surface corrugation profile. At large depth of corrugation, diffusive scattering would be strong and further reduce the reflection.

Focusing or collimating light through a glass lens with curved surfaces is a classical example of beam shaping in conventional refractive optics. Usage of metal in optical beam shaping has been mostly limited to the non-transmissive mode of operation such as reflection or diffraction, mainly due to the non-propagating nature of light in metal. We have performed finite-difference time-domain (FDTD) analysis of optical transmission through a nanoslit array structure formed on a metal layer with tapered film thickness. The analysis result shows refractive transmission of light through the nanoslit array, opening up the possibility of creating

metallic lenses that resemble glass lenses in their shape. Metallic lenses with curved surfaces are designed such that each nanoslit element transmits light with phase retardation controlled by the metal thickness in the aperture region. The FDTD analysis result demonstrates a focusing or collimating function of convex-shaped metal lenses. The phase of each nanoslit element can also be controlled by adjusting other structural and/or material parameters of nanoslits (such as slit width or the dielectric constant in the slit region) besides slit depth. All these features of metal refractive optics are useful for individual and independent control of phase at each slit, and offer great flexibility in designing the nano-optic lenses that can shape arbitrary beam profiles without being restricted by the constraints of conventional optics.

BIBLIOGRAPHY

- [1] M. Ohtsu: *Progress in Nano-Electro-Optics I* ed. by M. Ohtsu (Springer-Verlag Berlin Heidelberg New York 2003), preface.
- [2] M. Born, and E. Wolf: *Principles of Optics* (7th edition, Cambridge University Press, 1999).
- [3] K. Cho, H. Hori, and K. Kitahara: *Nano-Optics* ed. by S. Kawata, M. Ohtsu, M. Irie (Springer-Verlag Berlin Heidelberg New York 2002).
- [4] C. Kittel: *Introduction to Solid State Physics* (6th edition, John Wiley & Sons, 1986).
- [5] C. F. Bohren, and D. R. Huffman: *Absorption and Scattering of Light by Small Particles* (John Wiley & Sons, 1983).
- [6] E. D. Palik: *Handbook of Optical Constants of Solids* (Academic Press, 1998).
- [7] H. Raether: *Surface Plasmons on Smooth and Rough Surfaces and on Gratings* (Springer-Verlag Berlin Heidelberg 1988).
- [8] A. Liebsch: *Electronic Excitations at Metal Surfaces* (Plenum Press, New York and London, 1997).
- [9] U. Kreibig, and M. Vollmer: *Optical Properties of Metal Clusters* (Springer-Verlag Berlin Heidelberg New York, 1995).
- [10] D. M. Sullivan: *Electromagnetic Simulation Using the FDTD Method* (IEEE Press, New York, 2000).
- [11] A. Taflove: *Computational Electrodynamics The Finite-Difference Time-Domain Method* (Artech House, Boston London, 1995).
- [12] T. Ito and K. Sakoda, Phys. Rev. B **64**, 045116 & 045117 (2001).
- [13] H. A. Bethe, Phys. Rev. **66**, 163 (1944).
- [14] T. W. Ebbesen, H. J. Lezec, H. F. Ghaemi, T. Thio, and P. A. Wolff, Nature (London) **391**, 667 (1998).
- [15] H. F. Ghaemi, T. Thio, D. E. Grupp, T. W. Ebbesen, and H. J. Lezec, Phys. Rev. B **58**, 6779 (1998).

- [16] T. J. Kim, T. Thio, T. W. Ebbesen, D. E. Grupp, and H. J. Lezec, *Opt. Lett.* **24**, 256 (1999).
- [17] D. E. Grupp, H. J. Lezec, T. Thio, and T. W. Ebbesen, *Adv. Mater.* **11**, 860 (1999).
- [18] D. E. Grupp, H. J. Lezec, T. W. Ebbesen, k. M. Pellerin, and T. Thio, *Appl. Phys. Lett.* **77**, 1569 (2000).
- [19] A. Krishnan, T. Thio, T. J. Kim, H. J. Lezec, T. W. Ebbesen, P. A. Wolff, J. Pendry, L. Martin-Moreno, and F. J. Garcia-vidal, *optics comm.* **200**, 1 (2001).
- [20] U. Schröter and D. Heitmann, *Phys. Rev. B* **58**, 15419 (1998).
- [21] M. M. J. Treacy, *Phys. Rev. B* **66**, 195105 (2002).
- [22] J. A. Porto, F. J. Garcia-Vidal, and J. B. Pendry, *Phys. Rev. Lett.* **83**, 2845 (1999).
- [23] Y. Takakura, *Phys. Rev. Lett.* **86**, 5601 (2001).
- [24] Q. Cao and P. Lalanne, *Phys. Rev. Lett.* **88**, 057403 (2002).
- [25] F. J. Garcia-Vidal and L. Martin-Moreno, *Phys. Rev. B* **66**, 155412 (2002).
- [26] T. Lopez-Rios, D. Mendoza, F. J. Garcia-Vidal, J. Sanchez-Dehesa, and B. Pannetier, *Phys. Rev. Lett.* **81**, 665 (1998).
- [27] Z. Sun, Y. S. Jung, and H. K. Kim, *Appl. Phys. Lett.* **83**, 3021 (2003).
- [28] Z. Sun, and H. K. Kim, *Appl. Phys. Lett.* **81**, 3458 (2002);
- [29] Z. Sun, PhD preliminary thesis, Optoelectronics Lab, Department of Electrical Engineering, University of Pittsburgh (2002).
- [30] A. Degiron, H. J. Lezec, W. L. Barnes, and T. W. Ebbesen, *Appl. Phys. Lett.* **81**, 4327 (2002).
- [31] L. Martin-Moreno, F. J. Garcia-Vidal, H. J. Lezec, K. M. Pellerin, T. Thio, J. B. Pendry, and T. W. Ebbesen, *Phys. Rev. Lett.* **86**, 1114 (2001).
- [32] P. W. Barber, R. K. Chang, and H. Massoudi, *Phys. Rev. Lett.* **50**, 997 (1983).
- [33] L. Novotny and C. Hafner, *Phys. Rev. E* **50**, 4094 (1994).
- [34] W. L. Barnes, T. W. Preist, S. C. Kitson, and J. R. Sambles, *Phys. Rev. B* **54**, 6227 (1996).
- [35] W. L. Barnes, T. W. Preist, S. C. Kitson, J. R. Sambles, N. P. K. cotter, and D. J. Nash, *Phys. Rev. B* **51**, 11164 (1995-II).
- [36] Y. J. Chen, E. S. Koteles, R. J. Seymour, G. J. Sonek, and J. M. Ballantyne, *Solid State Comm.*, vol. **46**, No. 2, p95-99 (1983).

- [37] H. Lochbihler, Phys. Rev. B **50**, 4795 (1994-I).
- [38] M. G. Salt, W. C. Tan, and W. L. Barnes, App. Phys. Lett. **77**, 193 (2000).
- [39] A. A. Maradudin, R. F. Wallis, and G. I. Stegeman, Solid State Comm., vol. **46**, No. 6, p481-485 (1983).
- [40] K. Busch, C. T. Chan, and C. M. Soukoulis: *Photonic Band Gap Materials* ed. by C. M. Soukoulis, (Kluwer Academic Publishers, Dordrecht/Boston/London, 1996).
- [41] P. W. Barber, R. K. Chang, and H. Massoudi, Phys. Rev. Lett. **50**, 997 (1983).
- [42] M. Meier and A. Wokaun, Opt. Lett. **8**, 581 (1983).
- [43] O. J. F. Martin: *Optical Nanotechnologies* ed. by J. Tominaga and D. P. Tsai, Topics Appl. Phys. **88**, 183-210 (Springer-Verlag Berlin Heidelberg 2003).
- [44] E. Moreno, D. Erni, and C. Hafner, Phys. Rev. B, **65**, 155120 (2002).
- [45] J. P. Kottmann, and Olivier J. F. Martin, Opt. Exp., **8**, 655 (2001).
- [46] M. Quinten, A. Leitner, J. R. Krenn, and F. R. Aussenegg, Opt. Lett. **23**, 1331 (1998).
- [47] S. A. Maier, M. L. Brongersma, P. G. Kik, and H. A. Atwater, Phys. Rev. B **65**, 193408 (2002).
- [48] H. Masuda and K. Fukuda, Science **268**, 1466 (1995).
- [49] J. P. O'Sullivan and G. C. Wood, Proc. R. Soc. London, Ser. A **317**, 511 (1970).
- [50] D. Routkevitch, A. A. Tager, J. Haruyama, D. Almawlawi, M. Moskovits, and J. M. Su, IEEE Trans. Electron Devices **43**, 1646 (1996).
- [51] A. P. Li, F. Müller, A. Birner, K. Nielsch, and U. Gösele, J. Appl. Phys. **84**, 6023 (1998).
- [52] F. Li, L. Zhang, and R. M. Metzger, Chem. Mater. **10**, 2470 (1998).
- [53] H. Masuda, H. Yamada, M. Satoh, H. Asoh, M. Nakao, and T. Tamamura, Appl. Phys. Lett. **71**, 2770 (1997).
- [54] H. Masuda, H. Asoh, M. Watanabe, K. Nishio, M. Nakao, and T. Tamamura, Adv. Mater. **13**, 189 (2001).
- [55] C. Y. Liu, A. Datta, and Y. L. Wang, Appl. Phys. Lett. **78**, 120 (2001).
- [56] N. W. Liu, A. Datta, C. Y. Liu, and Y. L. Wang, Appl. Phys. Lett. **82**, 1281 (2003).
- [57] D. Crouse, Y-H. Lo, A. E. Miller, and M. Crouse, Appl. Phys. Lett. **76**, 49 (2000).

- [58] W. Hu, D. Gong, Z. Chen, L. Yuan, K. Saito, C. A. Grimes, and P. Kichambare, *Appl. Phys. Lett.* **79**, 3083 (2001).
- [59] S. R. J. Brueck, V. Diadiuk, T. Jones, and W. Lenth, *Appl. Phys. Lett.* **46**, 915 (1985).
- [60] S. Collin, F. Pardo, and J. L. Pelouard, *Appl. Phys. Lett.* **83**, 1521 (2003).
- [61] N. E. Hecker and R. A. Höpfel, *Appl. Phys. Lett.* **75**, 1577 (1999).
- [62] S. Martellucci and A. N. Chester ed., *Diffraction Optics and Optical Microsystems* (Plenum Press, New York, 1997).
- [63] A. Degiron, H. J. Lezec, W. L. Barnes, and T. W. Ebbesen, *Appl. Phys. Lett.* **81**, 4327 (2002).
- [64] E. Altewischer, M. P. van Exter, and J. P. Woerdman, *Nature* **418**, 304 (2002).
- [65] H. J. Lezec, et al., *Science* **107**, 1895 (2002).
- [66] L. Martín-Moreno, F. J. Garcia-Vidal, H. J. Lezec, A. Degiron, and T. W. Ebbesen, *Phys. Rev. Lett.* **90**, 167401 (2003).
- [67] W. L. Barnes, A. Dereux and T. W. Ebbesen, *Nature* **424**, 824 (2003).
- [68] Z. Sun, and H. K. Kim, *Appl. Phys. Lett.* **85**, 642 (2004).
- [69] S. Astilean, P. Lalanne, and M. Palamaru, *Optics Comm.* **175**, 265 (2000).
- [70] F. J. García-Vidal, H. J. Lezec, T. W. Ebbesen, and L. Martín-Moreno, *Phys. Rev. Lett.* **90**, 213901 (2003).
- [71] F. J. Garcia-Vidal, L. Martin-Moreno, H. J. Lezec and T. W. Ebbesen, *Appl. Phys. Lett.* **83**, 4500 (2003).